Electronic Supplementary Information (ESI)

Dynamics and control of active sites in hierarchically nanostructured cobalt phosphide/chalcogenide-based electrocatalysts for water splitting

Yonggui Zhao, Nanchen Dongfang, Carlos A. Triana, Chong Huang, Rolf Erni, Wenchao Wan, Jingguo Li, Dragos Stoian, Long Pan, Ping Zhang, Jinggang Lan, Marcella Iannuzzi, and Greta R. Patzke*

Y. G. Zhao, N. Dongfang, Dr. C. A. Triana, C. Huang, W. C. Wan, J. G. Li, Dr. J. G. Lan, PD Dr. M. Iannuzzi, and Prof. G. R. Patzke
Department of Chemistry, University of Zurich, Winterthurerstrasse 190, CH-8057 Zurich, Switzerland
E-mail: greta.patzke@chem.uzh.ch

Dr. R. Erni
Electron Microscopy Center, Empa, Swiss Federal Laboratories for Materials Science and Technology, Überlandstrasse 129, CH-8600 Dübendorf, Switzerland

Dr. D. Stoian
Swiss-Norwegian Beamlines at the European Synchrotron Radiation Facility, 38000 Grenoble, France.

Prof. L. Pan
Key Laboratory of Advanced Metallic Materials of Jiangsu Province, School of Materials Science and Engineering, Southeast University, Nanjing 211189, China

Prof. P. Zhang
School of Electrical and Information Engineering and Key Laboratory of Advanced Ceramics and Machining Technology of Ministry of Education, Tianjin University, Tianjin 300072, China

Table of Contents

1. Experimental Details and Methods

Chemicals. Cobalt(II) nitrate hexahydrate (≥ 98 %), cobalt(II) acetate tetrahydrate (≥ 98 %), cetrimonium bromide (≥99 %), 2-methylimidazole (≥99 %), iron(III) nitrate nonahydrate (≥98 %), polyvinylpyrrolidone (PVP, MW~10000), potassium hexacyanoferrate(III) (≥ 99 %), potassium hexacyanoferrate(II) trihydrate (≥99 %), potassium hexacyanocobaltate(III) (≥99 %), potassium hydroxide (≥99.97 %), potassium thiocyanate (≥99 %), sodium citrate dihydrate (≥99 %), sodium hypophosphite (98-101 %), selenium (≥99.5 %), tellurium (≥99.8 %), thioacetamide (≥99 %), urea (≥99 %), IrO_2 (99.9 %), RuO_2 (99.9 %), and 20 wt.% Pt/C were purchased from Sigma-Aldrich. All chemicals were used as received without any further purification.

Synthesis of ZIF-67. ZIF-67 was prepared at room temperature based on a previously reported method with slight modifications.[1-2] In a typical synthetic procedure, 580 mg of cobalt(II) nitrate hexahydrate and 10 mg cetrimonium bromide were dissolved into 20 mL of deionized (DI) water to form a clear transparent pink solution A. At the same time, a total of 9.08 g of 2-methylimidazole was dissolved into 140 mL of DI water to form a clear transparent solution B. Solution A was rapidly poured into solution B. After stirring at room temperature for 30 min, the purple precipitate was centrifuged and washed with ethanol at least three times. Finally, the products were transferred into a drying oven and dried at 70 ℃ overnight.

Synthesis of yolk-shell ZIF-67@CoFe-based Prussian blue (ZIF-67@CoFe-PB). The synthesis of ZIF-67@CoFe-PB was performed as follows. A total of 50 mg of ZIF-67 precursors were dispersed in 30 mL of ethanol by sonication for 15 min. Meanwhile, a total of 100 mg of potassium hexacyanoferrate(III) was dissolved in 10 mL of DI water and stirred for 15 min. Then, the potassium hexacyanoferrate(III) solution was rapidly poured into the ZIF-67 dispersion and stirred for another 2.5 h. The brick-red precipitations were centrifuged and washed with DI water and ethanol at least three times. Finally, the obtained ZIF-67@CoFe-PB products were transferred into a drying oven and dried at 70 ℃ overnight. The formation of yolk-shell ZIF-67@CoFe-PB cubic nanostructures is proposed as follows:

$$Co(C_4H_5N_2)_x \ \text{(ZIF-67)} \longrightarrow Co^{2+} + xC_4H_5N_2^- \quad \text{(aqueous conditions, eq. S1)}$$

$$3Co^{2+} + 2K_3Fe(CN)_6 \longrightarrow Co_3[Fe(CN)_6]_2 + 6K^+ \quad \text{(aqueous conditions, eq. S2)}$$

Synthesis of Co-based Prussian blue (Co-PB). First, 1.2 mmol of cobalt(II) acetate tetrahydrate and 1.6 mmol of sodium citrate dihydrate were dissolved into 40 mL of DI water to obtain a clear transparent pink solution A. Second, 0.8 mmol of potassium hexacyanocobaltate(III) was added into 40 mL of DI

water to form a transparent solution B. Solution B was rapidly poured into solution A and stirred for 3 min. The solution mixture was aged at room temperature for 18 h. Finally, the obtained pink precipitate was centrifuged, washed with DI water, and dried at 70 °C overnight.

Synthesis of Fe-based Prussian blue (Fe-PB). Fe-PB was synthesized based on a previously reported method with slight modifications.[3] 3.8 g of PVP and 0.11 g of potassium hexacyanoferrate(II) trihydrate were dissolved into 50 mL of 0. 1 M HCl under magnetic stirring for 30 min. The as-prepared transparent solution was then transferred into a Teflon-lined stainless steel autoclave (90 mL) and kept at 80 °C for 24 h. The resulting products were centrifuged and washed several times with DI water and ethanol. Finally, the obtained blue precipitation was dried at 70 °C overnight for further use.

Synthesis of CoFe-based Prussian blue (CoFe-PB). 1.2 mmol of cobalt(II) acetate tetrahydrate and 1.6 mmol of sodium citrate dihydrate were dissolved into 40 mL of DI water to obtain a clear transparent pink solution A. A total of 0.8 mmol of potassium hexacyanoferrate(III) was added into 40 mL of DI water to form a transparent solution B. Solution B was rapidly poured into solution A and stirred for 2 min. The solution mixture was aged at room temperature for 24 h. Finally, the obtained purple precipitate was centrifuged, washed with DI water, and dried at 70 °C overnight.

Synthesis of cobalt sulfide with hollow structure (Co-S). 20 mg of ZIF-67 was dispersed in 6 mL of ethanol by sonication for 15 min. At the same time, a total of 50 mg of thioacetamide was dissolved into 6 mL of ethanol to obtain a transparent solution. The as-prepared thioacetamide solution was rapidly injected into 6 ml of ZIF-67 suspension and stirred for another 15 min. The mixed suspension was then transferred into a Teflon-lined stainless steel autoclave (20 mL) and kept at 120 °C for 4 h. The obtained black precipitate was collected by centrifugation, washed three times with DI water and ethanol, and dried at 70 °C overnight. To improve the crystallinity, the products were annealed at 300 °C under Ar atmosphere for 2 h. The formation of hollow structured Co-S was proposed as follows:[4-6]

$$CH_3CSNH_2 + 2C_2H_5OH \longrightarrow CH_3(NH_2)C(OC_2H_5)_2 + H_2S \quad \text{(eq. S3)}$$

$$Co(C_4H_5N_2)_2 + xH_2S \longrightarrow CoS_x + 2CH_4H_6N_2 + (2x\text{-}2)H^+ \quad \text{(eq. S4)}$$

Synthesis of hybrid cobalt sulfide and CoFe-based Prussian blue (Co-S@CoFe-PB). The preparation of Co-S@CoFe-PB was similar to that of Co-S. 20 mg of ZIF-67@CoFe-PB was dispersed into 6 mL of ethanol by sonication for 15 min. At the same time, a total of 50 mg of thioacetamide was dissolved into 6 mL of ethanol to obtain a transparent solution. Then, 6 mL of thioacetamide solution was injected into 6 ml of ZIF-67@CoFe-PB suspension and stirred for another 15 min. The mixed suspension was then transferred into a Teflon-lined stainless steel autoclave (20 mL) and kept at 120 °C for 4 h. The obtained black precipitate was collected by centrifugation, washed three times with DI water and ethanol, and dried at 70 °C overnight.

Synthesis of Co-phosphides, Fe-phosphides, and CoFe-phosphides (Co-P, Fe-P, and CoFe-P). A total of 20 mg of ZIF-67/Co-PB/Fe-PB/CoFe-PB precursors and 400 mg of sodium hypophosphite powders were placed at two separate positions in a porcelain boat with sodium hypophosphite at the upstream side of the tube furnace. Then, the samples were annealed at 350 ℃ under Ar atmosphere for 2 h with a ramping rate of 2 °C min^{-1}.

Synthesis of Co@CoFe-phosphides (Co@CoFe-P). To prepare Co@CoFe-P, a total of 20 mg of ZIF-67@CoFe-PB precursors and 400 mg of sodium hypophosphite powders with a mass ratio of 1/20 were placed at two separate positions in a porcelain boat with sodium hypophosphite at the upstream side of the tube furnace. Then, the samples were annealed at 250 ℃, 350 ℃, and 450 ℃ in Ar atmosphere for 2 h with a ramping rate of 2 °C min^{-1}. The samples annealed with different amounts of sodium hypophosphite (100 mg, 200 mg, 300 mg, 400 mg, and 500 mg) were denoted as Co@CoFe-P-1-5, Co@CoFe-P-1-10, Co@CoFe-P-1-15, Co@CoFe-P-1-20, and Co@CoFe-P-1-25.

Synthesis of Co@CoFe-oxides (Co@CoCoFe-O). To prepare Co@CoCoFe-O, 100 mg of ZIF-67@CoFe-PB precursors were placed into a muffle furnace and calcined at 350 ℃ in air for 2 h with a ramping rate of 2 °C min^{-1}.

Synthesis of Co@CoFe-selenides and Co@CoFe-tellurides (Co@CoFe-Se and Co@CoFe-Te). The preparation of Co@CoFe-Se and Co@CoFe-Te was similar to the synthetic strategy of Co@CoFe-P, except for replacing sodium hypophosphite powders with selenium and tellurium powders, respectively. For the synthesis of Co@CoFe-Se, 20 mg of ZIF-67@CoFe-PB precursors and 100 mg of Se were annealed at 350 ℃ in Ar atmosphere for 2 h with a ramping rate of 2 °C min^{-1}. To prepare Co@CoFe-Te, 20 mg of ZIF-67@CoFe-PB precursors and 100 mg of Te were annealed at 600 ℃ in Ar atmosphere for 2 h with a ramping rate of 2 °C min^{-1}.

Synthesis of Co-FeOOH. 0.3 mmol of cobalt(II) nitrate hexahydrate, 0.1 of mmol iron(III) nitrate nonahydrate, and 1 of mmol urea were dissolved into 14 mL DI water to obtain a clear transparent solution. The solution was then transferred into a Teflon-lined stainless steel autoclave (20 mL) and kept at 120 °C for 15 h. The obtained precipitate was collected by centrifugation, washed three times with DI water and ethanol, and dried at 70 °C overnight.

Materials characterization. Powder X-ray diffraction (PXRD) patterns were recorded on a STOE STADI P diffractometer (transmission mode, Ge monochromator) with Mo K_α (λ = 0.7093 Å) radiation operated at a voltage of 50 kV and a current of 40 mA. The morphologies of as-prepared samples were characterized using field-emission scanning electron microscopy (FESEM-Zeiss Supra 50 VP), and transmission electron microscopy (TEM-FEI Tecnai G2 Spirit). Energy-dispersive X-ray spectroscopy (EDX) attached to the FESEM instrument was used for analyzing the composition of the samples. High-resolution TEM (HRTEM), high angle annular dark field-scanning transmission electron microscopy

(HAADF-STEM), and scanning transmission electron microscopy-energy dispersive X-ray spectroscopy (STEM-EDX) element mappings were acquired on a FEI Titan Themis equipped with a hexapole-type aberration corrector for scanning transmission electron microscopy (CEOS DCOR) and a Super EDX system. Fourier-transform infrared (FTIR) spectra were recorded on a Bruker Vertex 70 spectrometer equipped with a Platinum ATR accessory containing a diamond crystal. X-ray photoelectron spectroscopy (XPS) spectra were recorded on a PerkinElmer PHI 1600 ESCA system with an excitation radiation source of Mg K_α 1253.6 eV. The binding energy was calibrated based on the standard C 1s peak of graphite at 284.6 eV. Inductively coupled plasma mass spectrometry (ICP-MS) was performed on an Agilent 8800 ICP-MS.

Preparation of working electrodes. 5.0 mg of catalysts were dispersed in 1 mL of ethanol and 50 μL of 5 wt% Nafion solution after sonication for 30 min to form a homogeneous ink. 4 μL of the catalyst ink was loaded onto a glassy carbon rotating disk electrode (GC-RDE) or screen-printed carbon electrode (SPCE) with a diameter of 3 mm (loading amounts of 0.3 mg/cm^2). The electrode was dried at room temperature overnight before use.

***Operando* and *ex situ* Raman spectroscopy measurements.** The *operando* and *ex situ* Raman spectra were recorded on a Renishaw Raman scope or InVia Qontor (Ar^+ laser, 532 nm). For the *ex situ* test, the pristine powder samples were pressed on quartz glass slides with a flat surface. The *operando* measurements were performed in an in-house designed electrochemical cell equipped with a SPCE (Dropsens, DRP-110). Chronoamperometry tests were performed by a stepwise increase of the anodic potential in the ranges of 0.8 to 1.55 V vs. RHE for OER in 1.0 M KOH or decrease the cathodic potential in the ranges of 0.05 V to -0.15 V vs. RHE for HER in 1.0 M KOH.

***Operando* and *ex situ* X-ray absorption spectroscopy (XAS).** X-ray absorption near-edge structure (XANES) and extended X-ray absorption fine structure (EXAFS) experiments at the Co and Fe *K*-edges were performed at the European Synchrotron Radiation Facility (ESRF), Swiss-Norwegian Beamline BM31, Grenoble, France. The XANES and EXAFS data were recorded in both transmission (TR) and fluorescence (FL) modes using liquid nitrogen (LN2) cooled Si(111) double crystal monochromator (DCM) (*if not otherwise mentioned, the XAS data shown in the main text were recorded in transmission mode*). TR tests were performed using ion chambers (I.C.) detectors for which the filling has been optimized at 20% absorption in I_0 (before the sample) and 80% absorption for $I_{1,2}$ (after the sample and reference foil), respectively. A Vortex® one-element silicon drift detector (SDD) with XIA-Mercury digital electronics was used in FL tests. *Ex situ* tests were performed by dispersion of solid powder samples in cellulose to optimize absorption length and reach an absorption step of ca. 1. Energy calibration was performed using the corresponding reference metal foils. For the *operando* measurements, the catalysts inks were drop-dried on carbon paper with a loading mass of 2.0~3.0 mg/cm^2. All XAS tests were conducted in synchrotron mode with low intensity to prevent beam damage.

Electrochemical measurements were carried out in an in-house developed electrochemical cell (as shown in **Figure S78**) at room temperature in 1.0 M KOH. A standard three-electrode system (Dropsens, DRP-110) using a Hg/HgO electrode (1.0 M KOH) as the reference electrode, graphite rod as the counter electrode, and the catalysts loaded in carbon paper as the working electrode, respectively, was used. Chronoamperometry test was performed by a stepwise increase of the anodic potential in the ranges of 0.8 to 1.55 V vs. RHE for OER or by a stepwise decrease of the cathodic potential in the ranges of 0.05 to -0.15 V vs. RHE for HER. In order to reduce the influence of noise and to improve the quality of the collected XAS signals, all *operando* XAS signals recorded at the constant potential were repeated 8~10 times (~3 mins per time) for the Co *K*-edge and 3 times (~15 mins per time) for the Fe *K*-edge. The recorded XAS signals were merged into a total XAS signal and used for EXAFS fitting. XANES and EXAFS spectra were processed using the ATHENA software. The k^3-weighted Fourier transform (FT) for all the EXAFS data was conducted into the k-range of 0 to 14 $Å^{-1}$. S_0^2 was obtained based on the fitting of the corresponding reference sample and fixed as a constant value for the other samples. For the fitting of the investigated Co *K*-edge EXAFS data, the k-ranges were limited from 3 to 11 $Å^{-1}$ for both HER and OER, and R-ranges were limited to 1.0 to 3.0 Å for OER and 1.0 to 2.3 Å for HER, respectively. Due to the low amounts of Fe ions in the Co@CoFe-P NBs, it was extremely challenging to acquire a similar quality of EXAFS data on the Fe *K*-edge as we recorded on the Co *K*-edge. Therefore, the investigations of Fe *K*-edge EXAFS data were limited to the k-range from 3 to 9 $Å^{-1}$, and the fitting was not conducted. All the EXAFS spectra are presented without phase correction.

XANES simulations

To validate the atomic coordination of the photoabsorbing Co cations by O and P atoms, the Co *K*-edge XANES spectra of Co-P and Co-P_{air} were calculated self-consistently by the *ab initio* Finite Difference Method (FDM), as implemented into the FDMNES Code.[6] The final excited state was approximated by relaxed configurations with a core hole at the [1*s*] level and an additional electron at the [4*p*] level. The spectra were calculated on a grid of 8 Å centered at the photoabsorbing Co site using the real energy-dependent exchange Hedin-Lundqvist potential.

Electrocatalytic performance tests. Electrochemical measurements were carried out at room temperature in 1.0 M KOH (pH 13.8), 1.0 M PBS (pH 7.0) and 0.5 M H_2SO_4 (pH 0.3). A standard three-electrode system (Metrohm Autolab PGSTAT302N potentiostat) equipped with a Ag/AgCl electrode (3.0 M KCl) for the test in 0.5 M H_2SO_4 and 1.0 M PBS and a Hg/HgO electrode (1.0 M KOH) for the test in 1.0 M KOH as reference electrodes, graphite rod as the counter electrode, and GC-RDE as the working electrode, respectively, were used. Prior to tests, the working electrode was running for 10

scans of cyclic voltammetry (CV) at 50 mV/s to reach a stable state. The linear sweep voltammetry (LSV) curves were collected at 5 mV/s with a rotation speed of 1600 rpm. Electrochemical impedance spectroscopy (EIS) measurements were conducted in the range of 100 m Hz to 10 k Hz with a 5 mV amplitude. Durability tests were conducted through CV cycling (200, 500, and 1000 cycles) and chronopotentiometric methods (10 and 20 mA/cm^2). The electrochemical double-layer capacitance (C_{dl}) was measured between 1.21 and 1.31 V vs. RHE by increasing the scan rates from 10 mV/s to 100 mV/s without any Faradaic processes involved. All measured potentials were converted to RHE using the following equation: E(RHE)=E+E(reference electrode)+0.059×pH. All polarization curves were corrected with 90 % iR-compensation, where R is the uncompensated ohmic contact resistance measured by electrochemical impedance spectroscopy at the open-circuit voltage. For the overall water splitting test, the catalyst inks were drop-dried on carbon paper (1×1 cm^2) with a loading mass of 0.3 and 1.0 mg/cm^2, respectively, both as cathodic and anodic electrodes. Poisoning tests were performed in 1.0 M KOH electrolyte with 0.1 M KSCN.

Sodium battery performance measurements. The sodium battery performance of as-prepared Co-S@CoFe-PB was tested in a LANHE CT2001A instrument. The as-prepared sample, carbon black, and CMC (binder) were mixed in DI water with a mass ratio of 70:20:10. The mixture was then stirred overnight to obtain a homogeneous slurry. The slurry was loaded on titanium holders and dried under vacuum conditions. Sodium foil and glass fiber membrane were employed as the counter electrode and separator, respectively. The test was conducted in 1.0 M $NaClO_4$ electrolyte, which was dissolved with propylene carbonate/fluoroethylene carbonate with a ratio of 95:5 vol.%.

Faradaic efficiency was calculated from the following equation:[5,7]

$$\text{Faradaic efficiency} = i_{ring} / (i_{disk} \times N) \quad \text{(eq. S5)}$$

where i_{disk} and i_{ring} are the disk and ring currents, respectively. N is the current collection efficiency of the rotating ring-disk electrode (RRDE) and is 0.2 in this study. The galvanostatic method was performed with a ratio speed of 1600 rpm during the measurements.

Density function theory (DFT) calculations.

All DFT simulations were performed using the CP2K package with Grimme D3 corrected Perdew-Burke-Ernzerhof (PBE).[8-10] The plane-wave cut-off energy of 500 Ry was set up for all simulations. The investigation of the local molecular environment was carried out by Goedecker-Teter-Hutter (GTH) pseudopotential and DZVP-MOLOPT-GTH basis. The investigated models have been optimized by the Broyden-Fletcher-Goldfarb-Shanno algorithm, and a 10^{-4} bohr/hartree was set up for the convergence criterion of the forces. The computed model was built by the CoP (111)-terminated surface, which was determined from HR-TEM measurements. Fe and O atoms were inserted afterward by partial

substitution of Co and P atoms, respectively. A 3×3×3 supercell with a total of 288 atoms based on CoP was used for all simulations. The atomic positions were fully relaxed until a maximum energy difference, and the residual force and energy convergence was 0.05 eV/Å and 1×10^{-4} eV, respectively. A vacuum layer of at least 15 Å thickness was added into the built supercell to avoid the interaction between top and bottom surfaces. Based on the computational hydrogen electrode models,[11-12] the free energy of OH^- was described as $G(OH^-) = G(H_2O) - G(H^*)$ assuming the equilibrium process $H^* + OH^- \rightarrow H_2O$, where the G(H*) was equal of the free energy of ½ H_2. When the pH was different from 0, the additional entropy G(pH) was added to the proton energy, i.e., $G(pH) = -kT \ln10 \times pH$. The thermodynamic free energy of all states was calculated as $G = E+E_{ZPE}-TS$, where E is ground state energy, E_{ZPE} is the zero-point energy, and S is the entropy.

2. Schematic diagram of the synthetic process

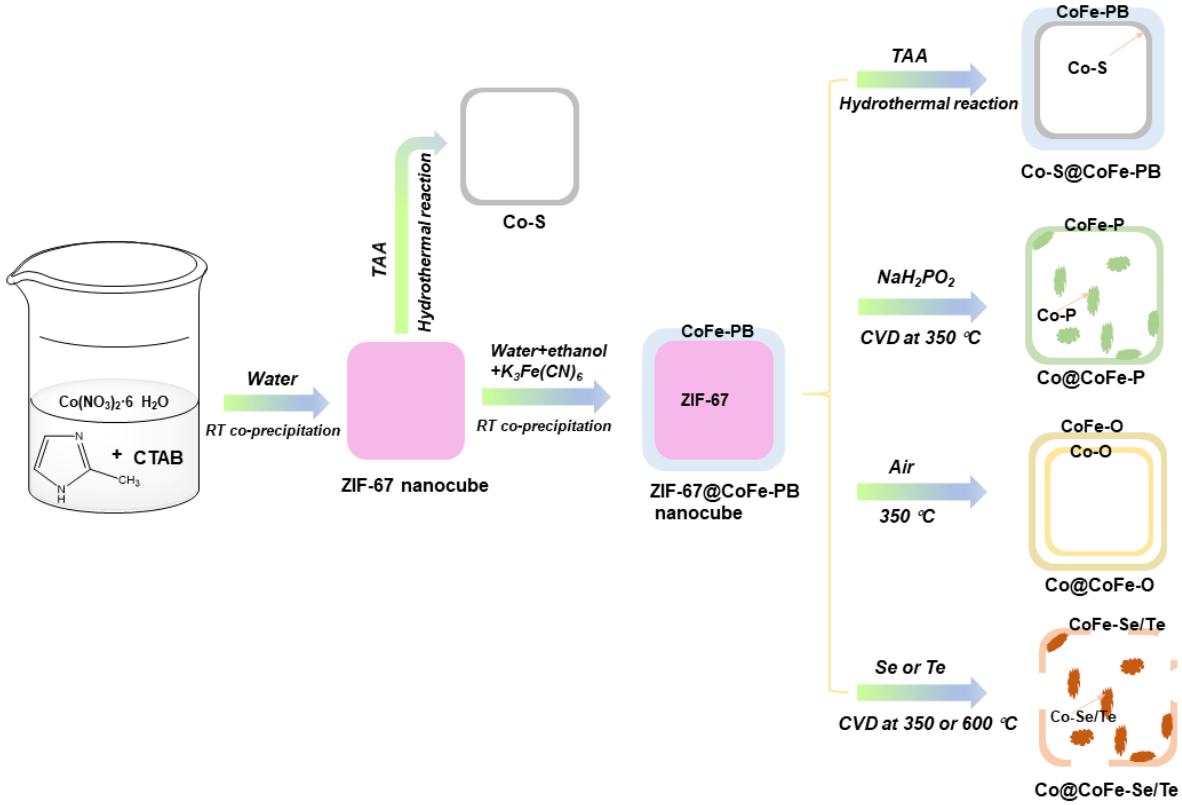

Figure S1. Schematic diagram of the synthetic process.

3. Basic characterization of as-prepared products

3.1 Characterization of as-prepared ZIF-67

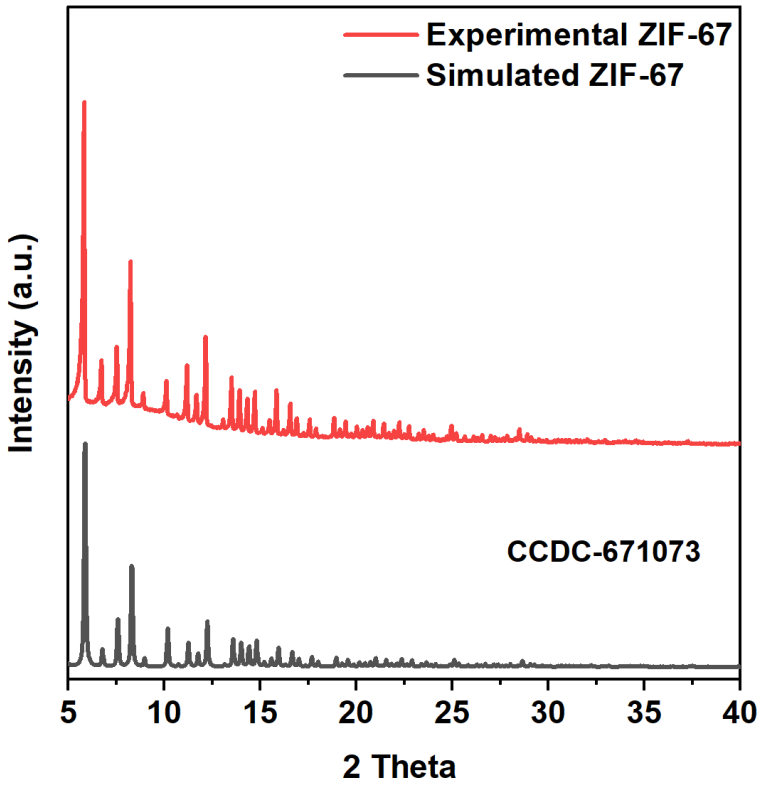

Figure S2. Calculated and experimental PXRD patterns of ZIF-67.

The experimental PXRD pattern of ZIF-67 matches perfectly with the simulated pattern (CCDC-671073), which demonstrates the successful synthesis of phase pure ZIF-67. FESEM (field-emission scanning electron microscopy) and TEM images demonstrate that the as-prepared ZIF-67 precursors possess a well-defined cubic nanostructure with an average particle size between 300~400 nm (**Figure 1a,e** and **Figures S3-S4**).

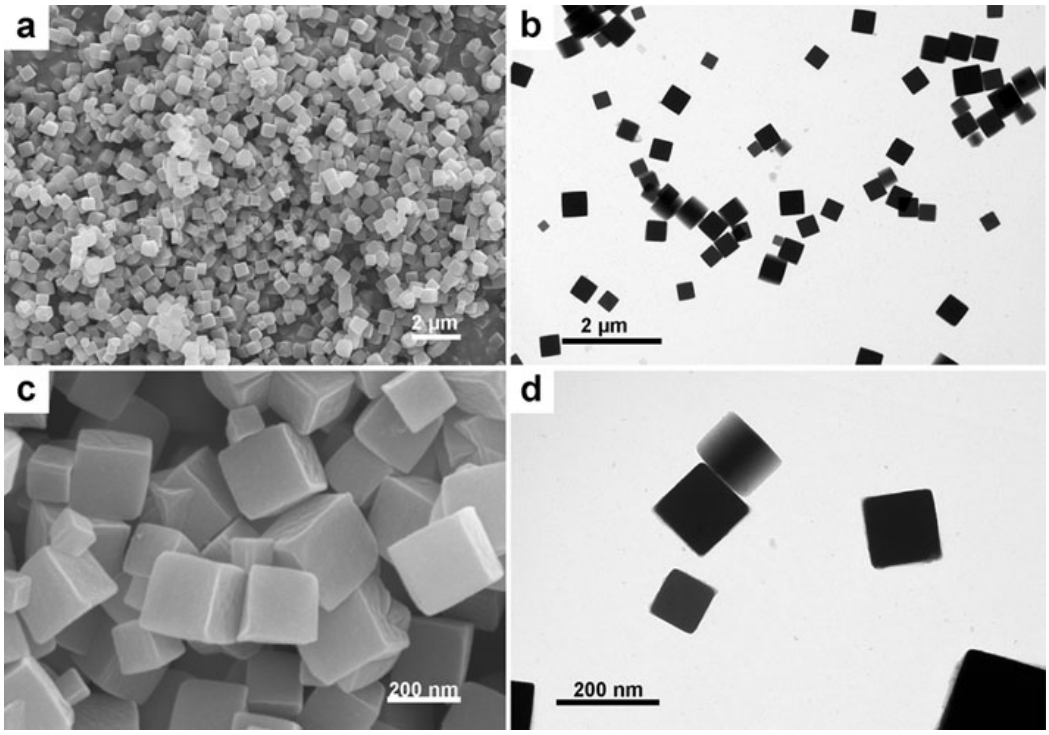

Figure S3. FESEM (a, c) and TEM (b, d) images of as-prepared ZIF-67.

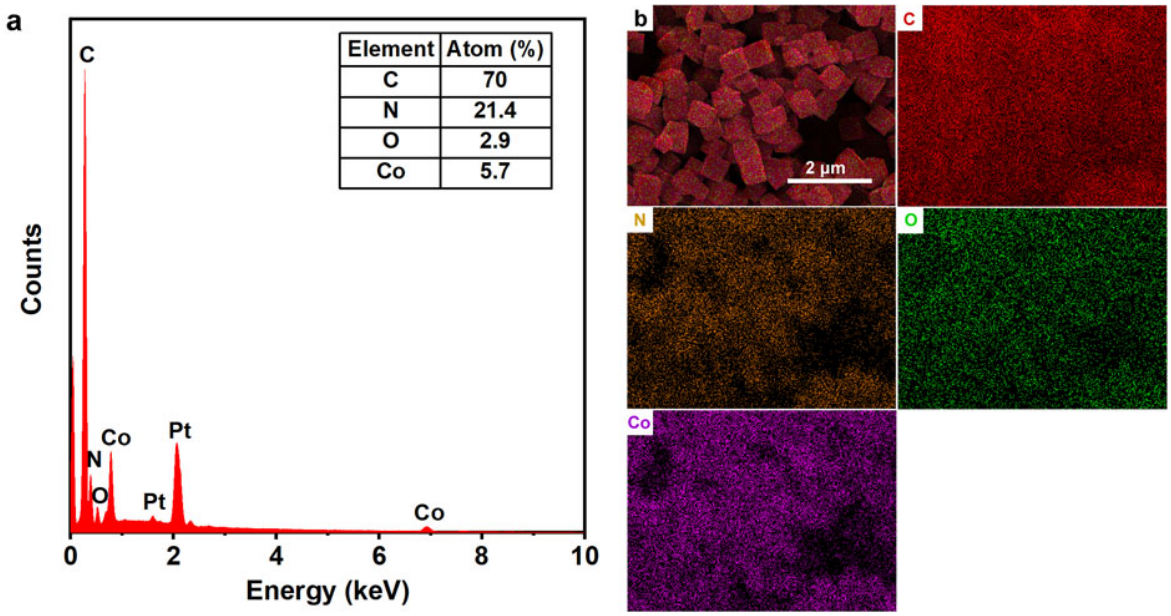

Figure S4. FESEM-EDX spectrum (a) and element mappings (b) of as-prepared ZIF-67.

3.2 Characterization of as-prepared ZIF-67@CoFe-PB

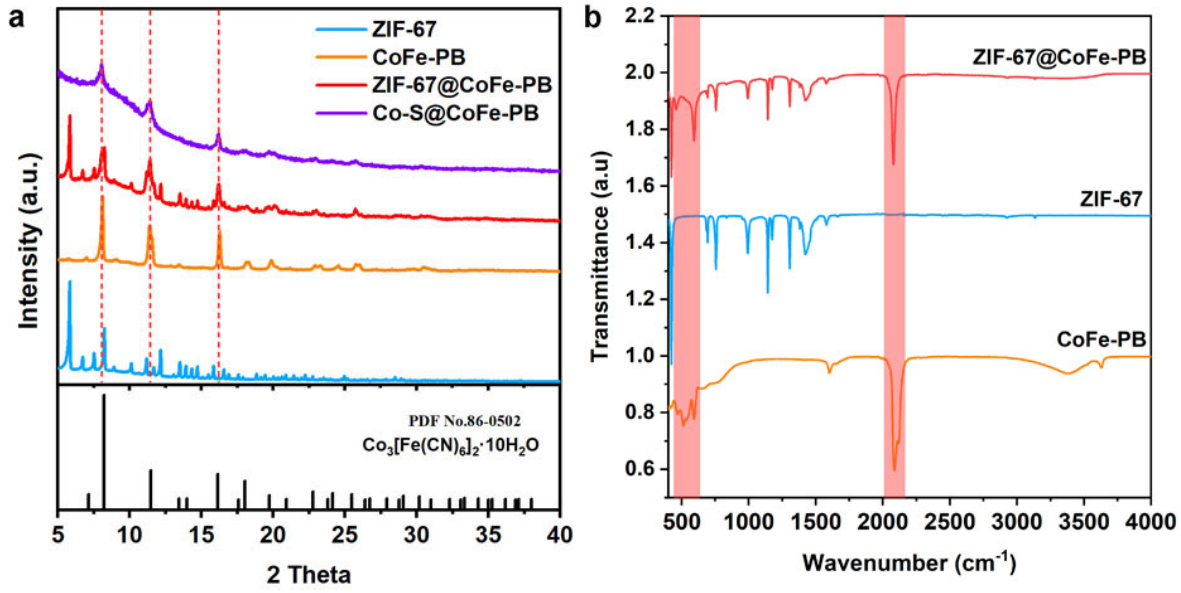

Figure S5. PXRD patterns (a) and FTIR spectra (b) of as-prepared ZIF-67, CoFe-PB, ZIF-67@CoFe-PB, and Co-S@CoFe-PB.

The PXRD pattern and FT-IR spectrum of as-prepared CoFe-PB agree with our previous study on CoFe-PB.[5] All the diffraction peaks of as-prepared CoFe-PB correspond to the standard cubic structure $Co_3[Fe(CN)_6]_2 \cdot 10H_2O$ (PDF No. 86-0501) (**Figure S5a**). The FT-IR spectrum (**Figure S5b**) of as-prepared CoFe-PB exhibits two pronounced peaks at 2117 and 2087 cm^{-1}, which are ascribed to the CN stretching modes in the Co-NC-Fe moieties. The peaks in the range of 400 to 750 cm^{-1} are assigned to M-C/N (M=Co, Fe) bonds. The as-prepared ZIF-67 does not show any FT-IR active peaks in the mentioned ranges. As shown in **Figure S5a**, the as-prepared ZIF-67@CoFe-PB presents the mixed PXRD signals from ZIF-67 and CoFe-PB (**Figure S5a**). FT-IR spectra (**Figure S5b**) indicate the successful formation of hybrid ZIF-67@CoFe-PB. After the ZIF-67@CoFe-PB precursor was reacted with TAA at 120 °C for 4 h, the PXRD pattern of Co-S@CoFe-PB only shows three main diffractions peaks appearing at $2\theta \approx 7.51°$, 11.18°, and 16.15°, corresponding to the (200), (220), and (400) planes of CoFe-PB, respectively. No diffraction peaks corresponding to ZIF-67 were present in the pattern of Co-S@CoFe-PB (**Figure S5a**). Moreover, the FT-IR spectrum of Co-S@CoFe-PB (**Figure S5b**) retained most peaks from CoFe-PB. In contrast, all the FT-IR peaks of ZIF-67 were absent for Co-S@CoFe-PB. Based on our previous study,[5] the anion exchange reaction between S^{2-} and CN^- is quite demanding and incomplete at lower hydrothermal reaction temperatures within a short reaction time. Therefore, we proposed that the dominant anion exchange reaction in the current study is arising between S^{2-} from TAA and $C_4H_5N_2^-$ from ZIF-67, resulting in the formation of CoS_x species after the hydrothermal reaction. The absence of diffraction peaks of CoS_x in the PXRD pattern (**Figure S5a**) is mainly due to its amorphous features. FESEM and TEM images indicate a cubic core-shell morphology of ZIF-67@CoFe-PB (**Figure S6**). The SAED pattern and HR-TEM images (**Figure S6**) were further recorded to analyze the phases of the as-prepared ZIF-67@CoFe-PB precursors. As seen from SAED patterns (**Figure S7b**),

the as-synthesized ZIF-67@CoFe-PB nanocubes exhibit three distinct diffraction rings, arising from the main crystal planes of (200), (220), and (400) of CoFe-PB, respectively. The HR-TEM images recorded on the different positions further display two clear lattice spacings of 5.2 Å and 3.6 Å, assigned to the (200) and (220) planes of CoFe-PB, respectively. Moreover, the STEM-EDX and FESEM-EDX element mappings (**Figures S8-S9**) reveal the homogenous distribution of C, O, and Co over both the core and the shell of the cube, while Fe and N are mainly dispersed in the shell, indicating the successful formation of core-shell ZIF-67@CoFe-PB nanocubes.

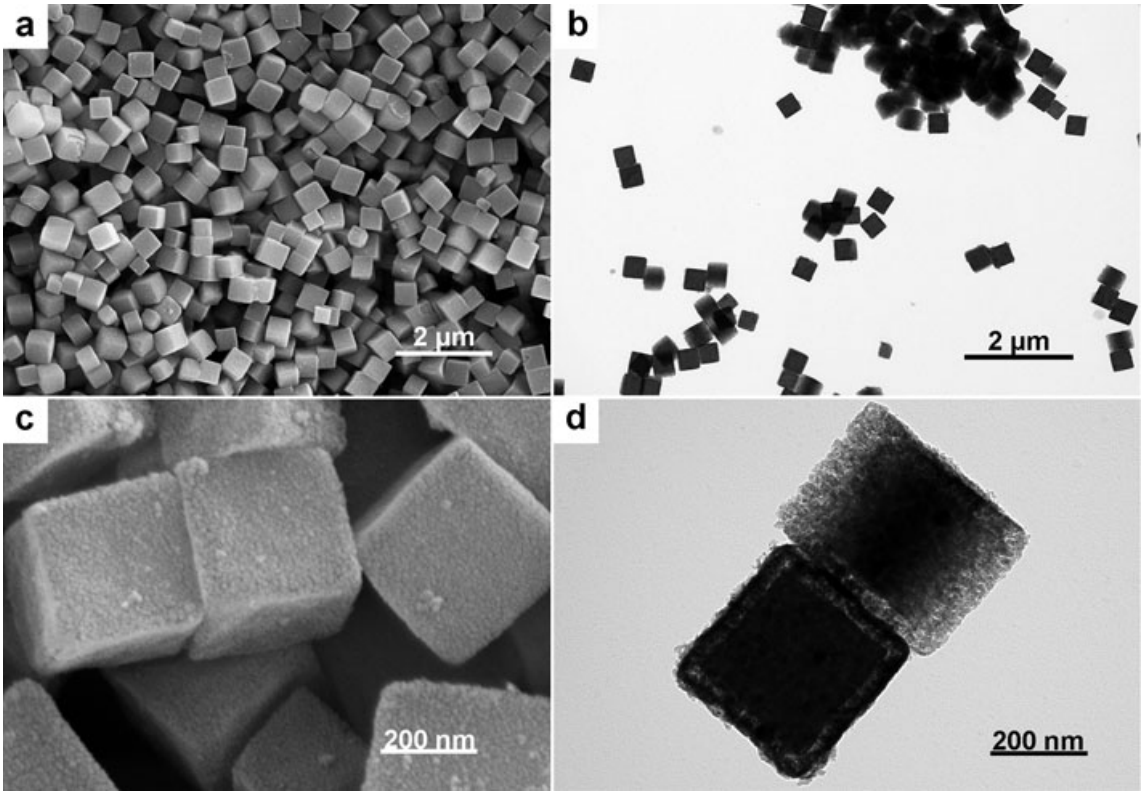

Figure S6. FESEM (a, c) and TEM (b, d) images of as-prepared ZIF-67@CoFe-PB.

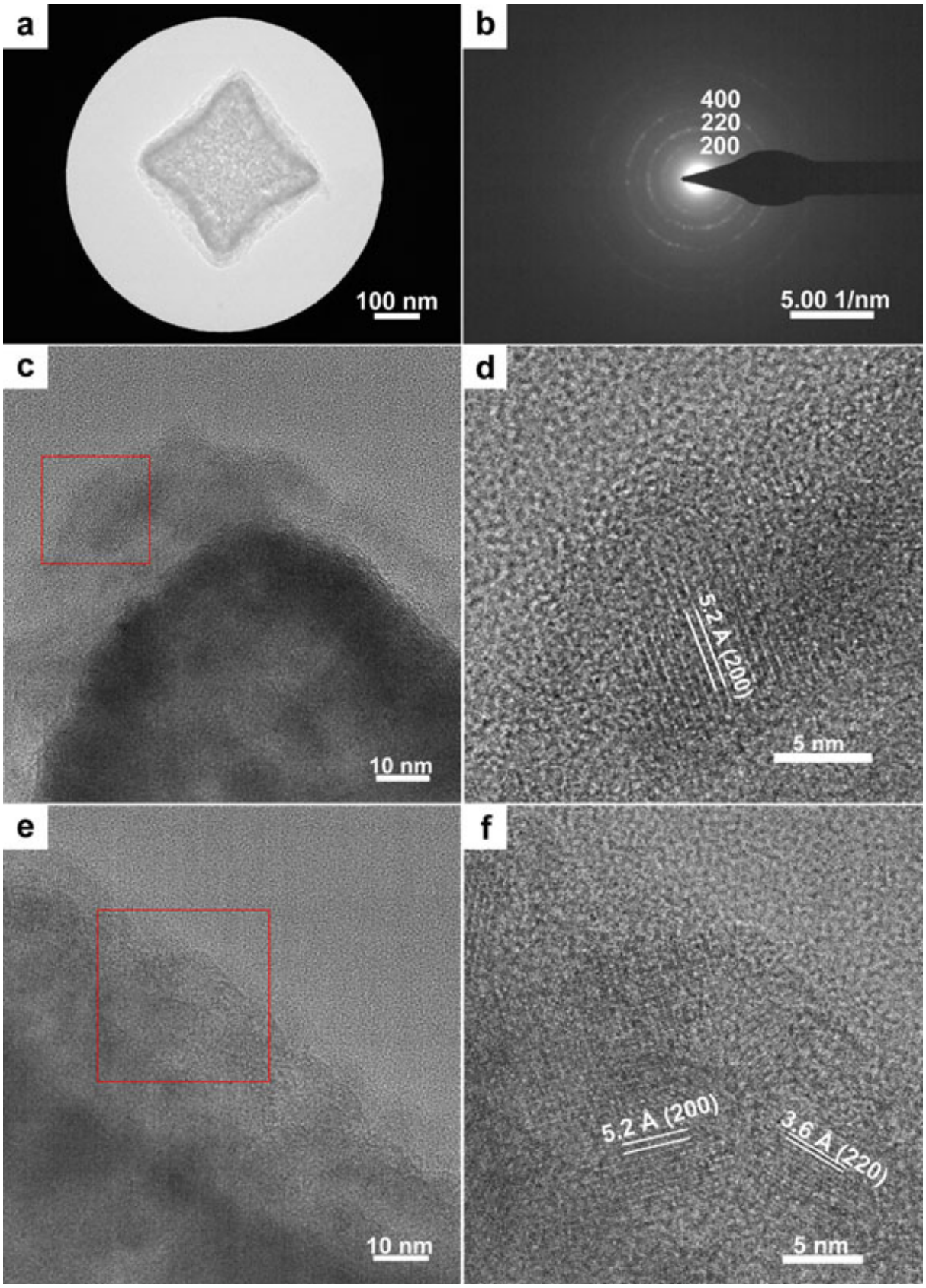

Figure S7. HR-TEM characterization of ZIF-67@CoFe-PB. (a, b) TEM image and corresponding SAED image. (c) HR-TEM image. (d) Zoom into the selected red area (**Figure S7c**). (e) HR-TEM image. (f) Zoom into the selected red area (**Figure S7e**).

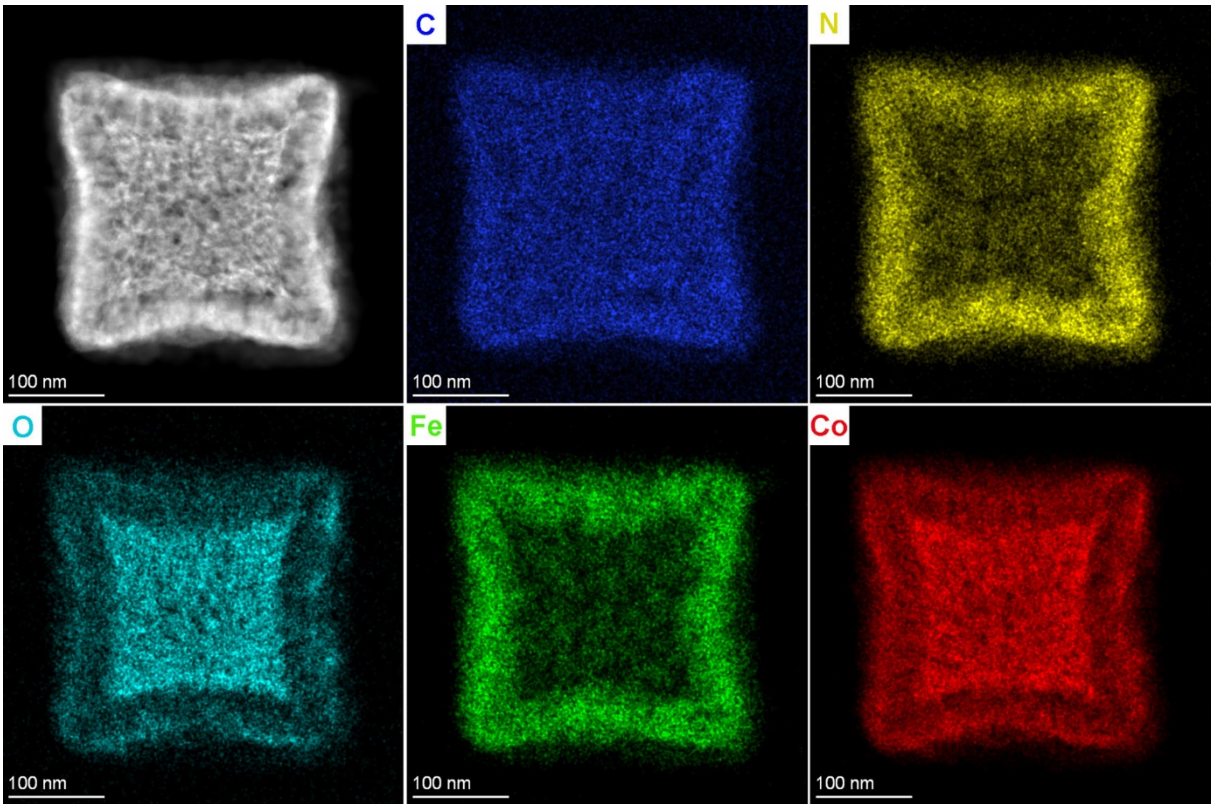

Figure S8. HAADF-STEM image and STEM-EDX element mappings of ZIF-67@CoFe-PB.

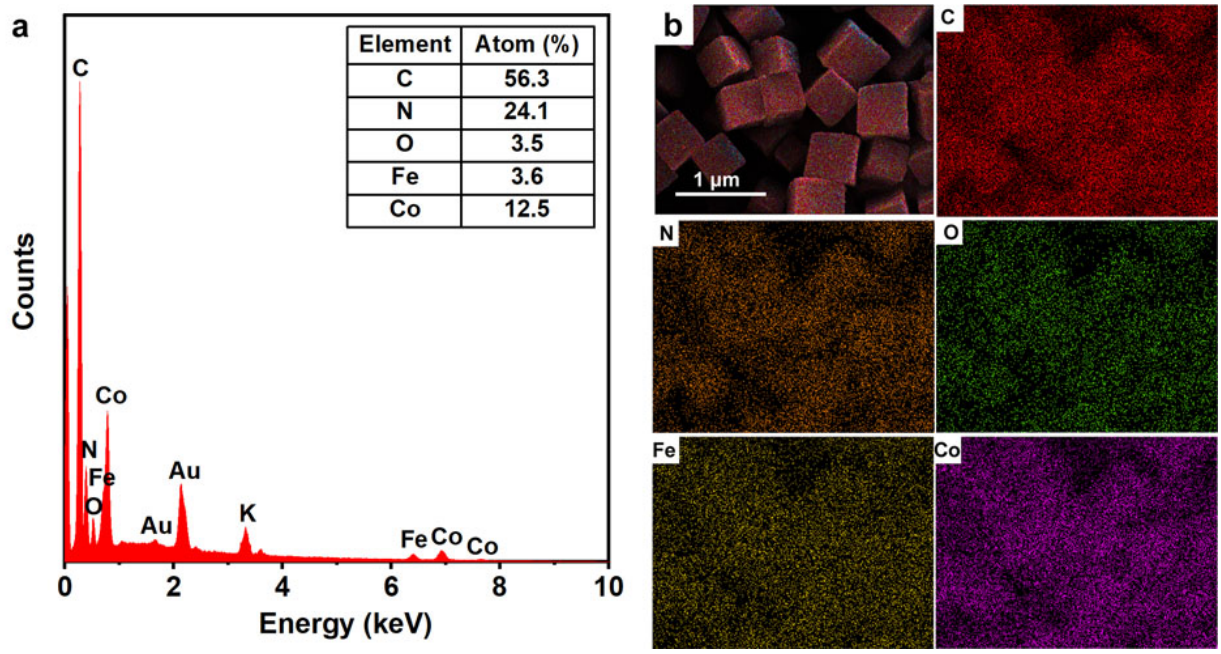

Figure S9. FESEM-EDX spectrum (a) and element mappings (b) of as-prepared ZIF-67@CoFe-PB.

3.3 Characterization of as-prepared Co-S@CoFe-PB

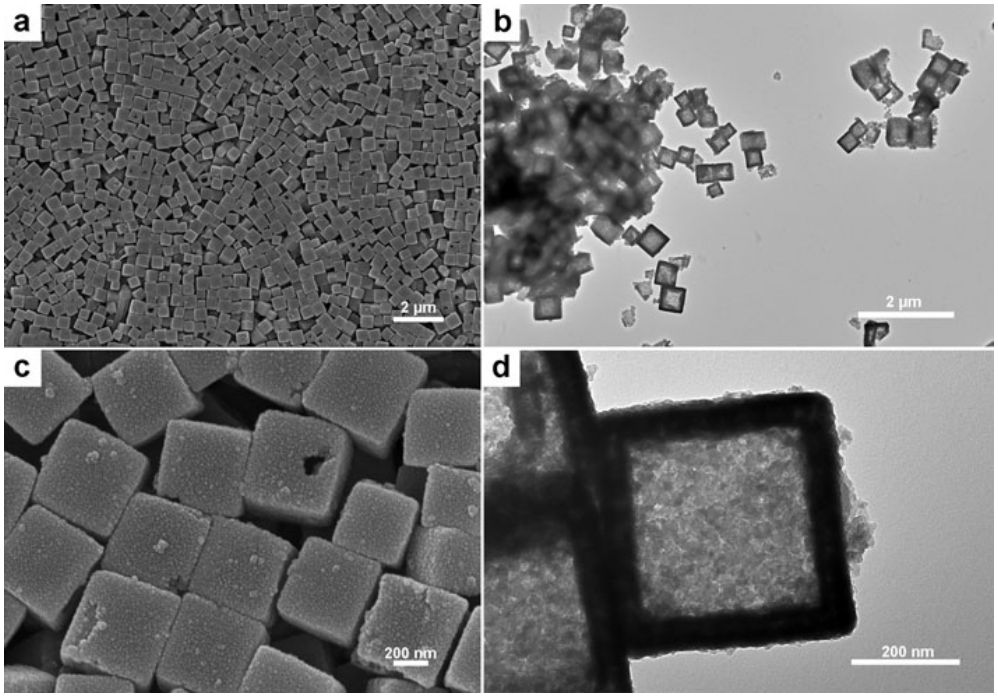

Figure S10. FESEM (a, c) and TEM (b, d) images of as-prepared Co-S@CoFe-PB.

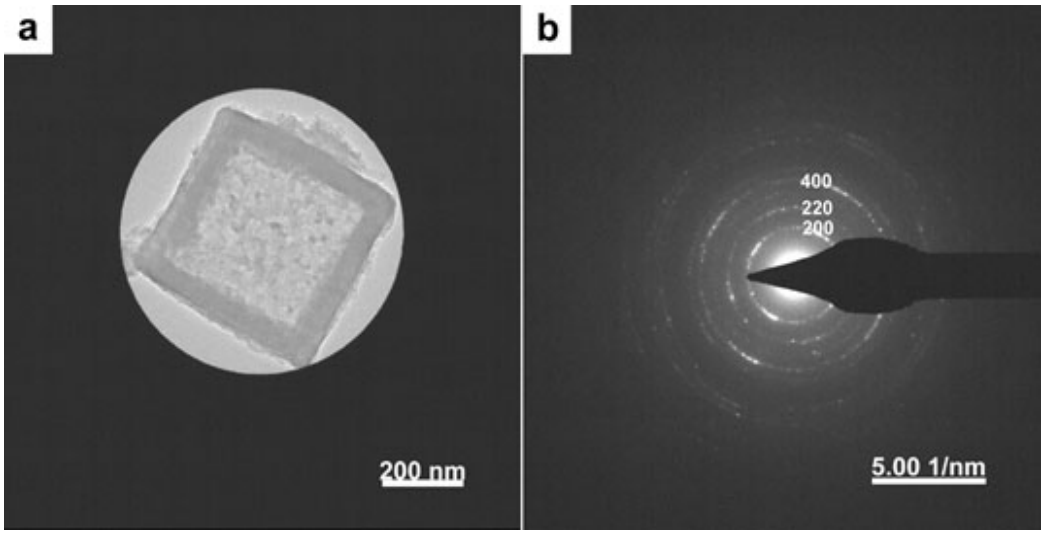

Figure S11. (a, b) TEM image and corresponding SAED image of Co-S@CoFe-PB.

The SAED pattern (**Figure S11b**) of Co-S@CoFe-PB shows three main diffraction rings, which are corresponding to the (200), (220), and (400) crystal planes of CoFe-PB, respectively. This indicates that CoFe-PB can retain its pristine crystal structure after the hydrothermal sulfidation reaction. Acquisition of HR-TEM images for Co-S@CoFe-PB NCs is challenging because some amorphous species are generally present on the outer layer of the cubes after the hydrothermal reaction.[5] The STEM-EDX and FESEM-EDX element mappings (**Figures S12-S13**) reveal the homogenous elemental distribution of C, N, O, and Co over the shell of the box, while S is mainly dispersed in the inner layer of the shell, suggesting that the major chemical exchange occurred between ZIF-67 and S^{2-}.

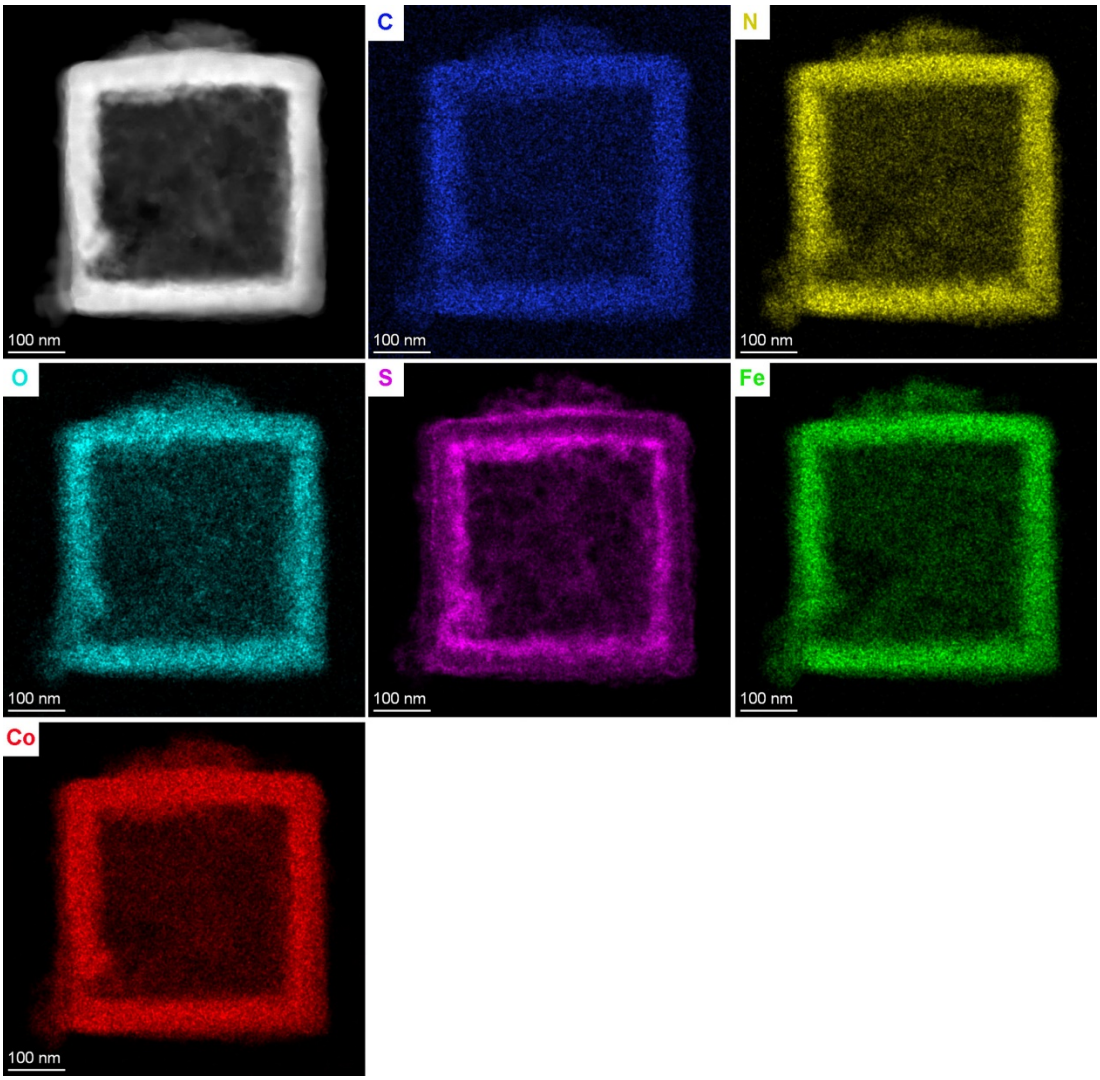

Figure S12. HAADF-STEM image and STEM-EDX element mappings of Co-S@CoFe-PB.

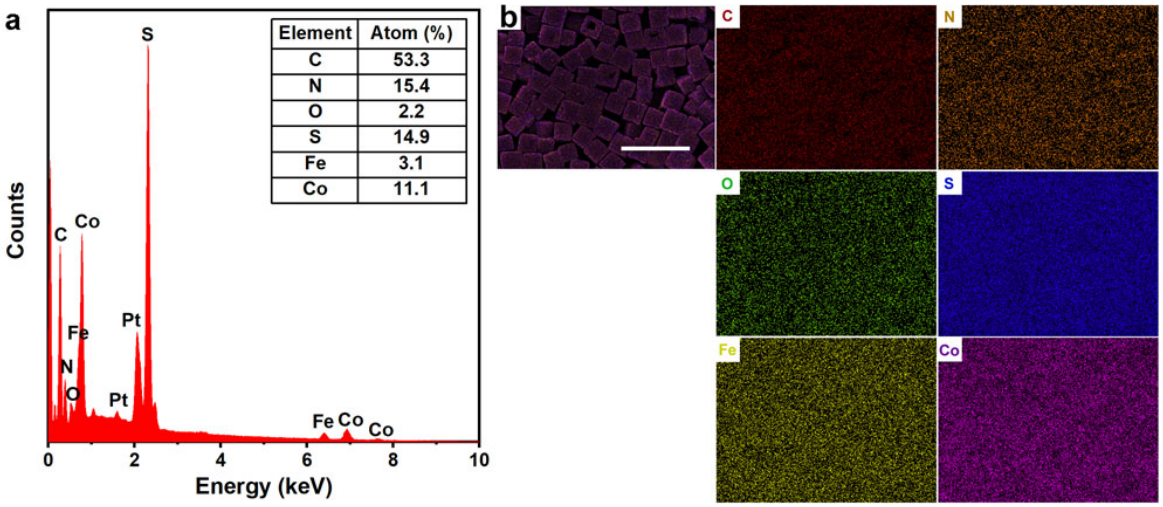

Figure S13. FESEM-EDX spectrum (a) and element mappings (b) of as-prepared Co-S@CoFe-PB.

3.4 Characterization of as-prepared Co-S

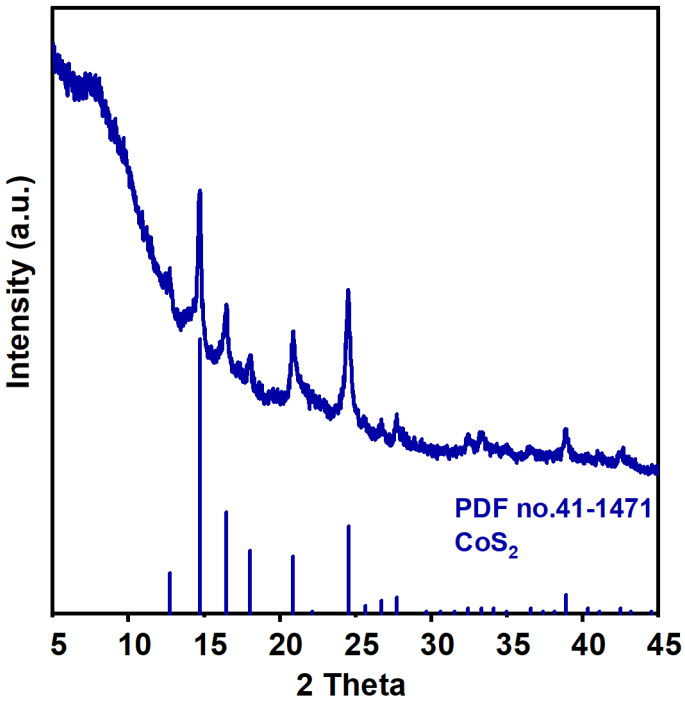

Figure S14. PXRD pattern of as-prepared Co-S.

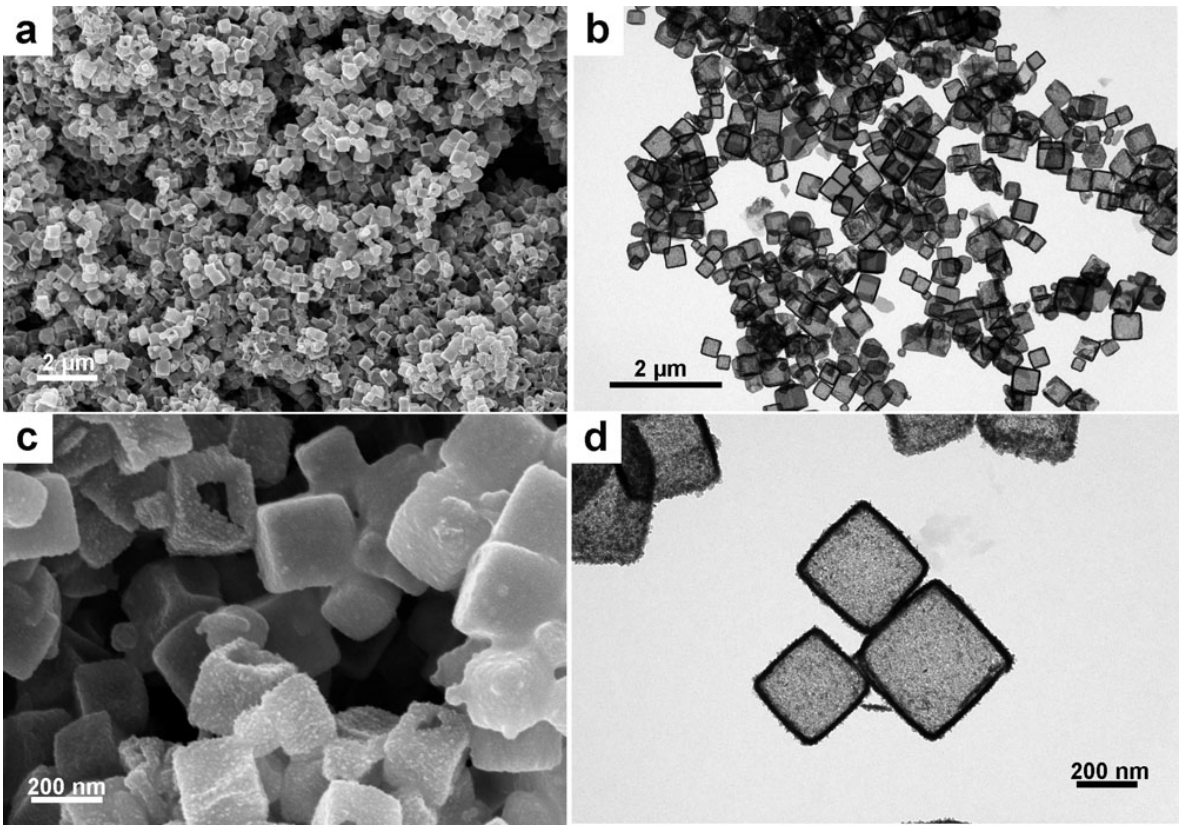

Figure S15. FESEM (a, c) and TEM (b, d) images of as-prepared Co-S.

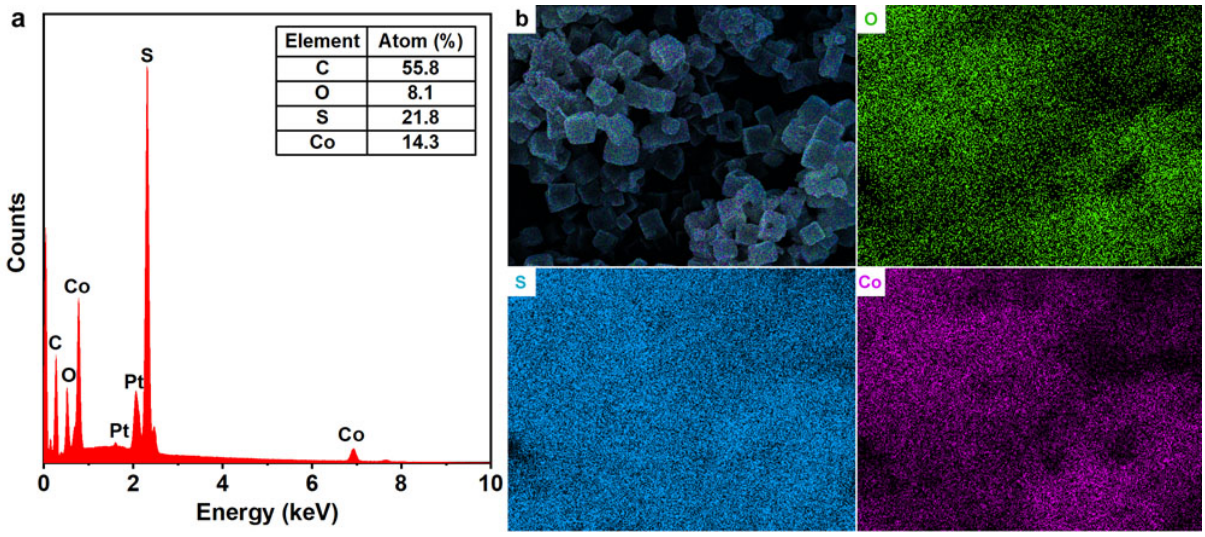

Figure S16. FESEM-EDX spectrum (a) and element mappings (b) of as-prepared Co-S.

3.5 Characterization of as-prepared Co@CoFe-P

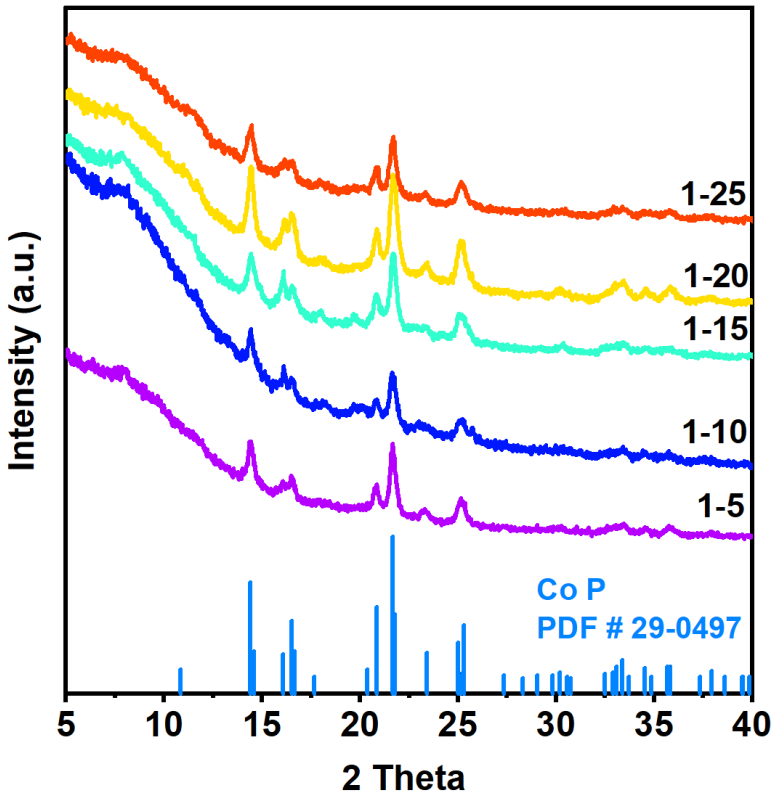

Figure S17. PXRD patterns of as-prepared Co@CoFe-P obtained with different mass ratios between the as-prepared precursors and NaH_2PO_2.

As shown in **Figure S17**, the PXRD patterns of Co@CoFe-P prepared with the different amounts of NaH_2PO_2 match well with reference CoP (PDF No. 29-0497, S.G. *Pnma*), indicating that partial Fe substitution in CoP does not influence its pristine crystal structure. Some peaks with lower intensities were also observed at 2 theta≈7.5°, indicating the presence of C after the reaction.[20,76,77]

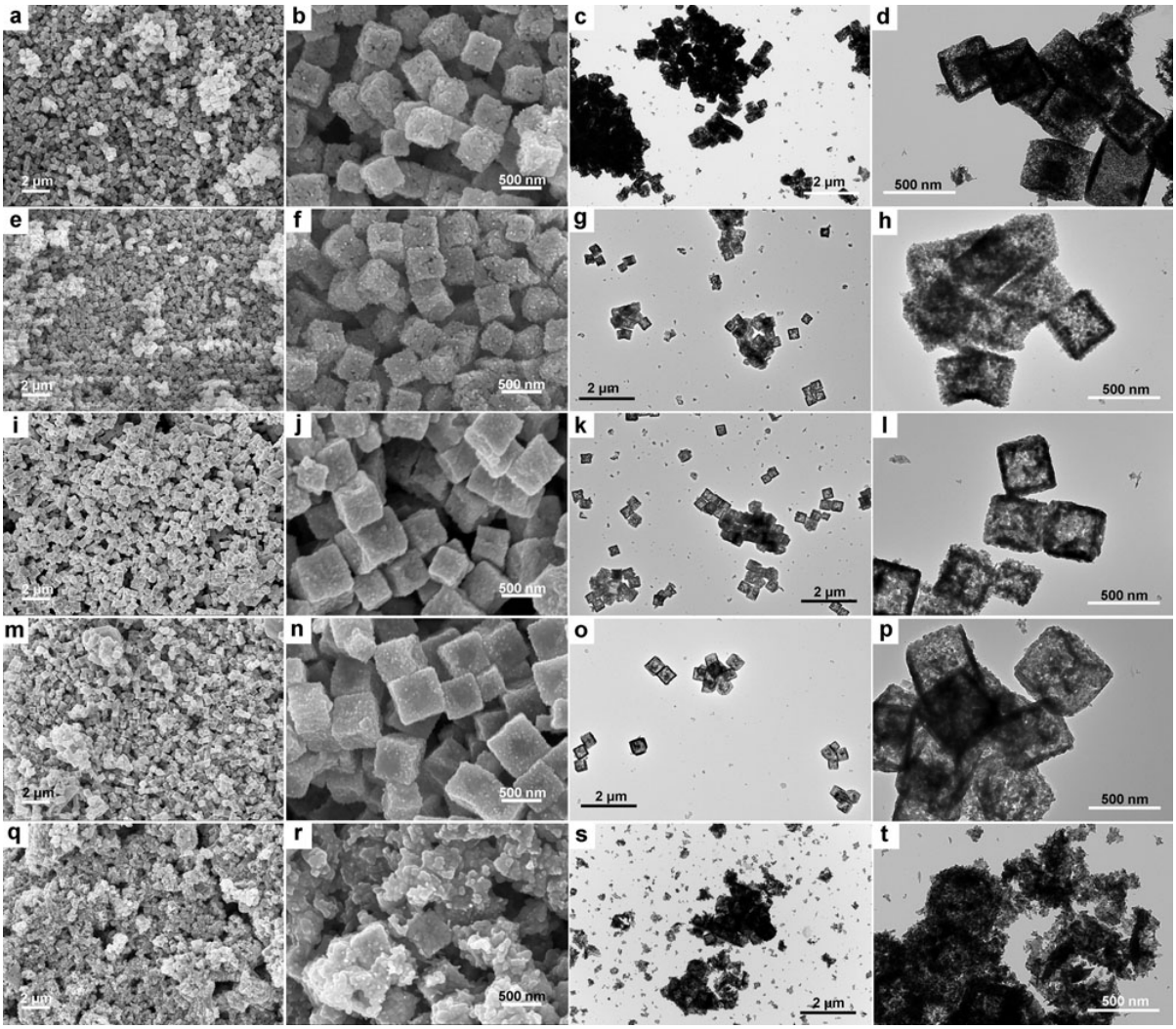

Figure S18. FESEM and TEM images of as-prepared Co@CoFe-P obtained with different mass ratios between the as-prepared precursors and NaH_2PO_2: (a-d) 1-5; (e-h) 1-10; (i-l) 1-15; (m-p) 1-20; (q-t) 1-25.

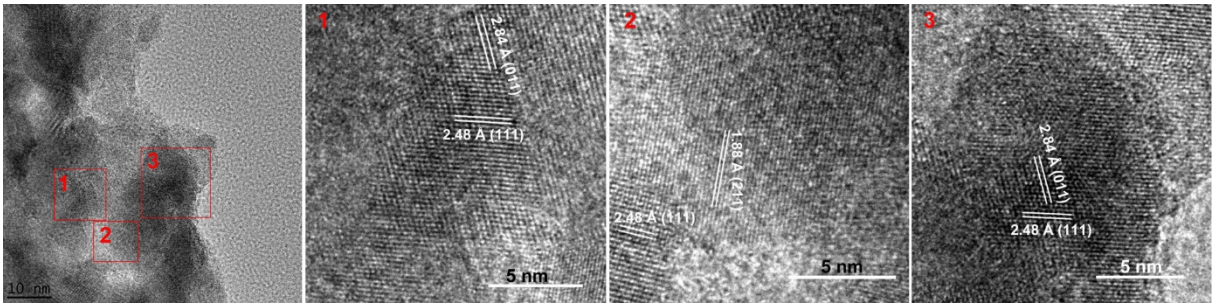

Figure S19. HR-TEM images of as-prepared Co@CoFe-P obtained with 400 mg of NaH_2PO_2 (1-20).

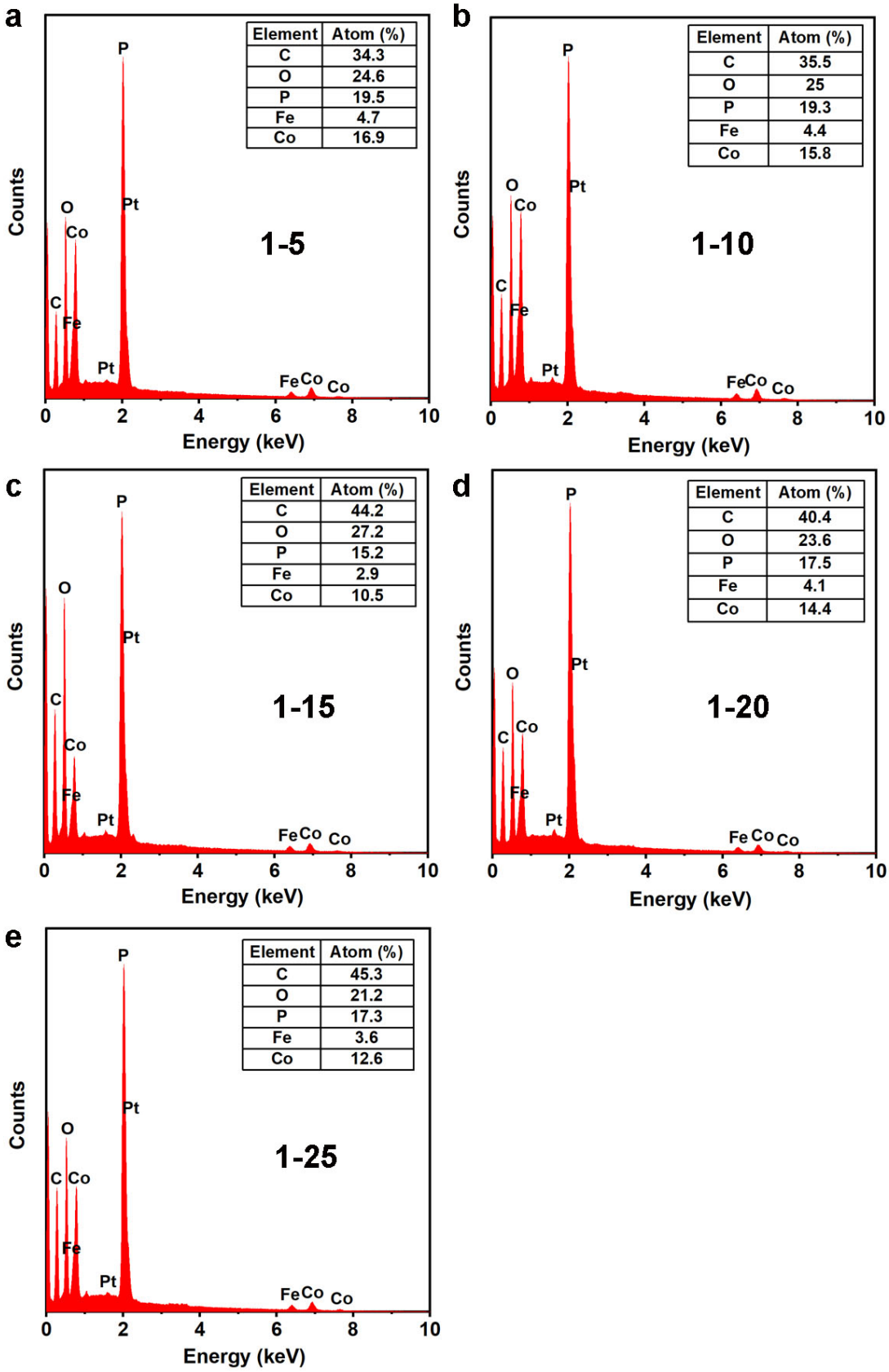

Figure S20. FESEM-EDX spectra of as-prepared Co@CoFe-P with different mass ratios between the as-prepared precursors and NaH_2PO_2: (a) 1-5; (b) 1-10; (c) 1-15; (d) 1-20; (e) 1-25.

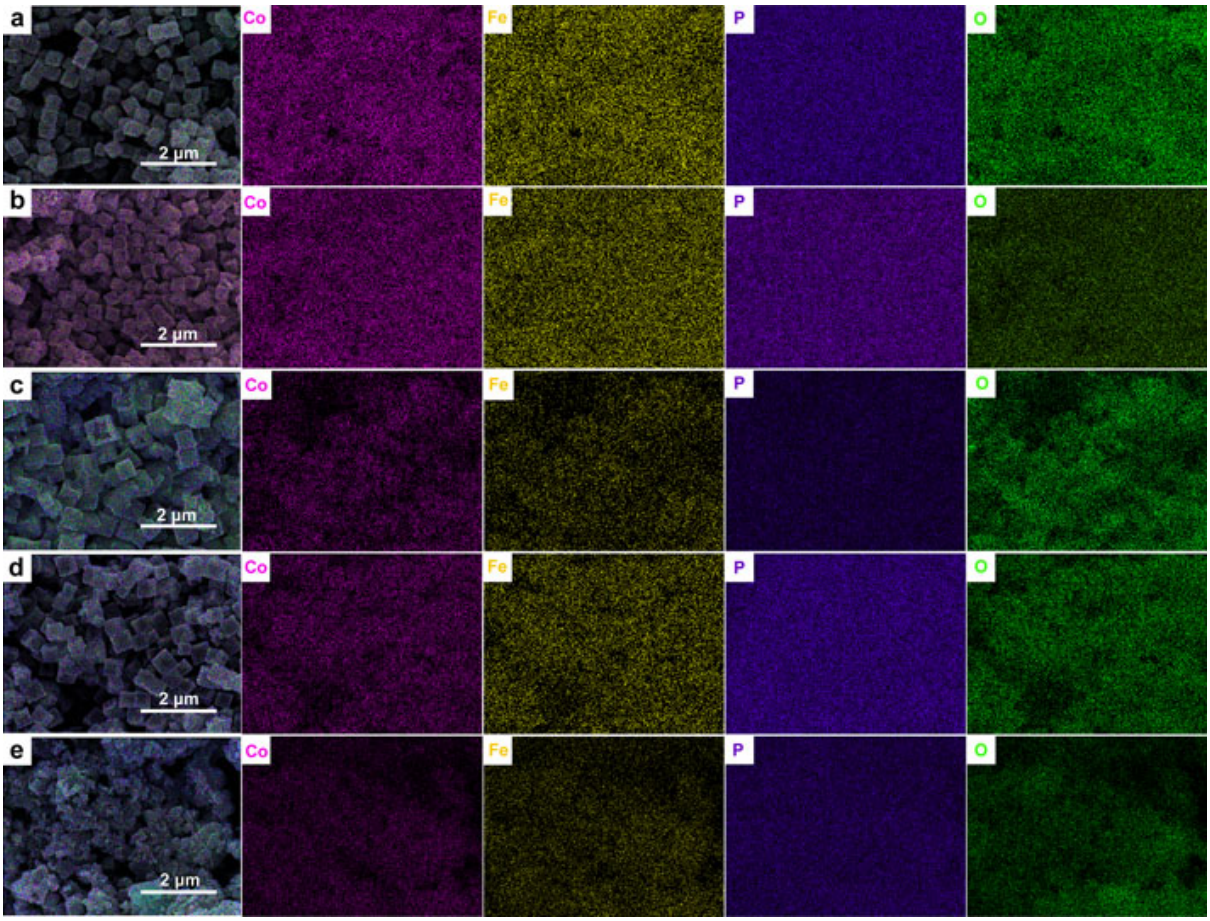

Figure S21. FESEM-EDX element mappings of as-prepared Co@CoFe-P different mass ratios between the as-prepared precursors and NaH_2PO_2: (a) 1-5; (b) 1-10; (c) 1-15; (d) 1-20; (e) 1-25.

FESEM and TEM images (**Figure S18**) reveal a morphological evolution with the adjustment of NaH_2PO_2 amounts. A low amount of NaH_2PO_2 slowed down the phosphorization process and the final products maintained their pristine cubic morphology, but with a thick shell and fewer cavities inside (**Figure S18a-S18d**). On the contrary, the reaction rate was enhanced when a higher amount of NaH_2PO_2 was present. Thereby, the final products still exhibit the cubic morphologies but with reduced thickness of shells and more cavities (**Figure S18e-S18p**). It is also significant to keep in mind that applying an excess reagent resource (20 mg of precursor with 500 mg of NaH_2PO_2) can destroy the initial morphological integrity and lead to a collapsed architecture in the end (**Figure S18q-S18t**). Besides, an analogous morphological evolution is also observed in the samples reacted from 250 to 450 °C compared with that arising from different NaH_2PO_2 amounts (**Figures S24-S27**).

Supplementary Discussion I: Investigation of the nucleation and growth processes

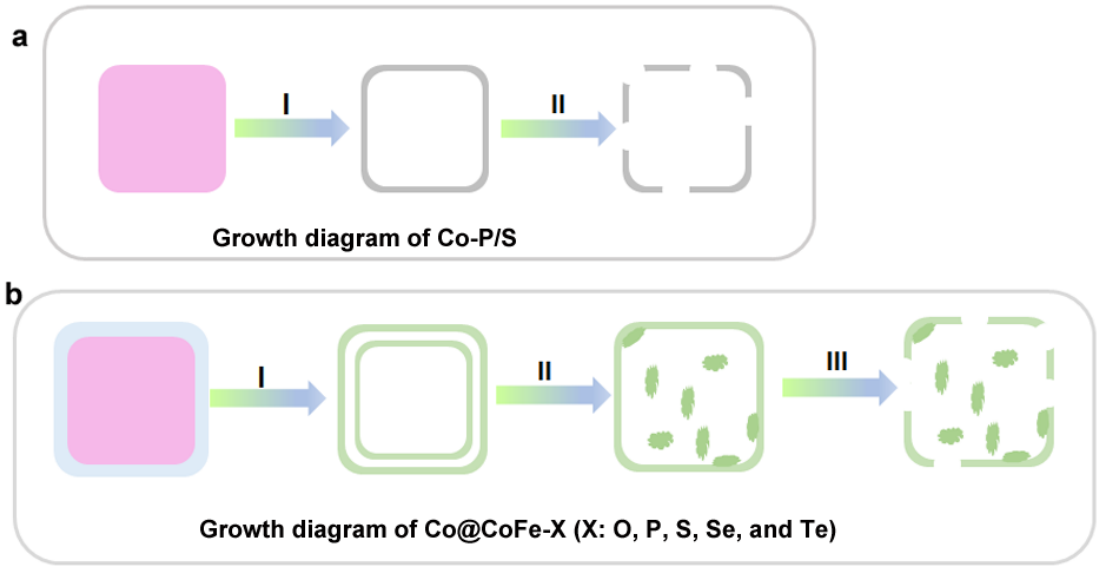

Figure S22. Schematic diagrams of the nucleation and growth processes.

ZIF-67@CoFe-PB NBs were prepared via a one-step co-precipitation method with as-prepared ZIF-67 as self-template. As described in the experimental procedure, ZIF-67 can slowly decompose into Co^{2+} and $C_4H_5N_2^-$ in mixed water and ethanol solvents.[1,4,17] Moreover, those ions arising from decomposition are mainly adsorbed on the surface of the ZIF-67 cubes. After adding $K_3Fe(CN)_6$ into the ZIF-67 dispersion, the $Fe(CN)_6^{3-}$ group can nucleate with Co^{2+} ions to form $Co_3[Fe(CN)_6]_2$ (CoFe-PB), due to strong interactions between Co^{2+} and $Fe(CN)_6^{3-}$.[5] Moreover, the formed CoFe-PB layer can prevent further decomposition of ZIF-67. As a result, the as-obtained products of ZIF-67@CoFe-PB show core-shell architectures (**Figure S6**).

The formation of Co-P/S and Co@CoFe-X (X:O, P, S, Se, and Te) NBs are both based on the Kirkendall effect.[5] Taking Co-P/S NBs as an example (**Figure S22a**), at an initial stage, the Co-P/S layer is formed on the surface of ZIF-67, due to the anion exchange between S/P and $C_4H_5N_2^-$. The newly formed Co-P/S layer can hinder the inward diffusion of S/P. As a consequence, the outward diffusion of $C_4H_5N_2^-$ from the core is becoming dominant, leading to the formation of a hollow box. However, with further prolonged reaction processes, the extra S/P can delete the obtained box architecture due to the surface tensions and mechanical properties. Therefore, the final products obtained from a long reaction time or a high amount of S/P cannot preserve the box architecture and exhibit random nanoparticle morphology (**Figure S23**).

The growth of Co@CoFe-X proceeds similar to Co-P/S. According to the results of Co-S@CoFe-P NBs (**discussion details in Figure S5 and Figures S10-S13**), we can conclude that the $C_4H_5N_2^-$ groups are more active than CN^- groups in the anion exchange reaction. This indicates that an inner box can be formed first at an early stage for the growth of Co@CoFe-X, as demonstrated in **Figures S10 and S21**. With a higher amount of X, the outer layer of CoFe-PB is converted into CoFe-X. However, the inner box collapsed due to the surface tension and mechanical properties. With further increasing amounts of X, the constructed outer boxes can also be destroyed, leading to broken boxes (**Figure S21q-t**).

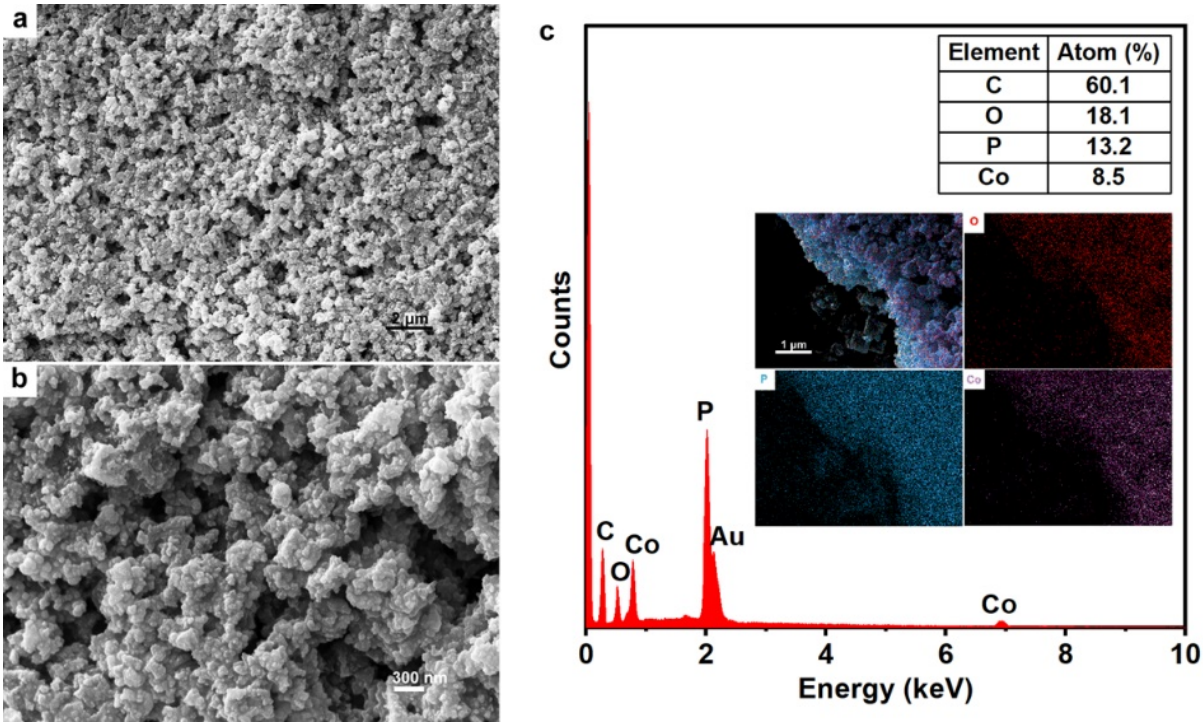

Figure S23. (a, b) FESEM images of Co-P prepared with ZIF-67 as a precursor. (c) FESEM-EDX spectrum and element mappings of Co-P prepared with ZIF-67 as a precursor.

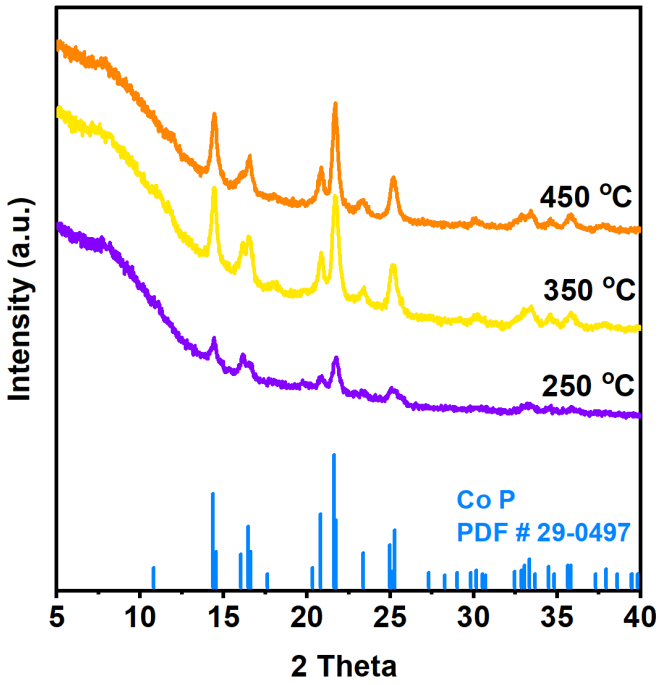

Figure S24. PXRD patterns of as-prepared Co@CoFe-P (1-20) at different reaction temperatures.

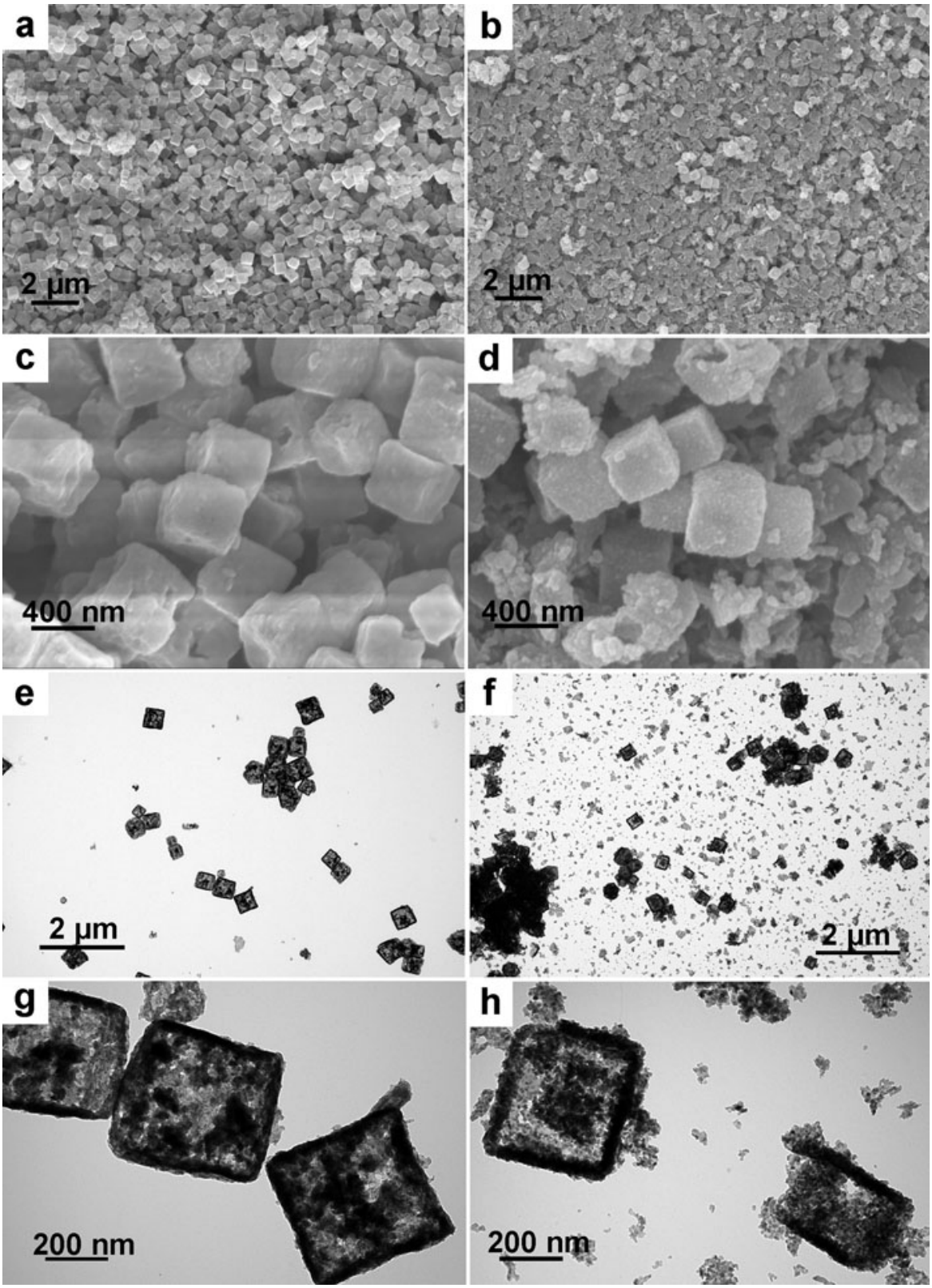

Figure S25. FESEM and TEM images of as-prepared Co@CoFe-P (1-20) at different reaction temperatures: (a, c, e, g) 250 °C; (b, d, f, h) 450 °C.

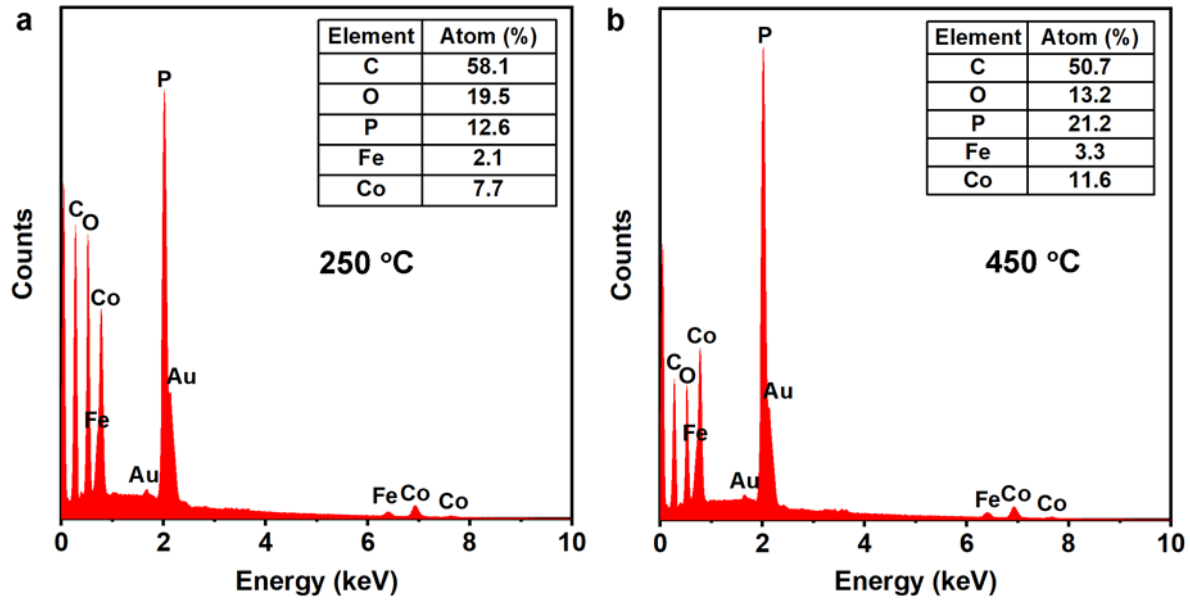

Figure S26. FESEM-EDX spectra of as-prepared Co@CoFe-P (1-20) at different reaction temperatures: (a) 250 °C; (b) 450 °C.

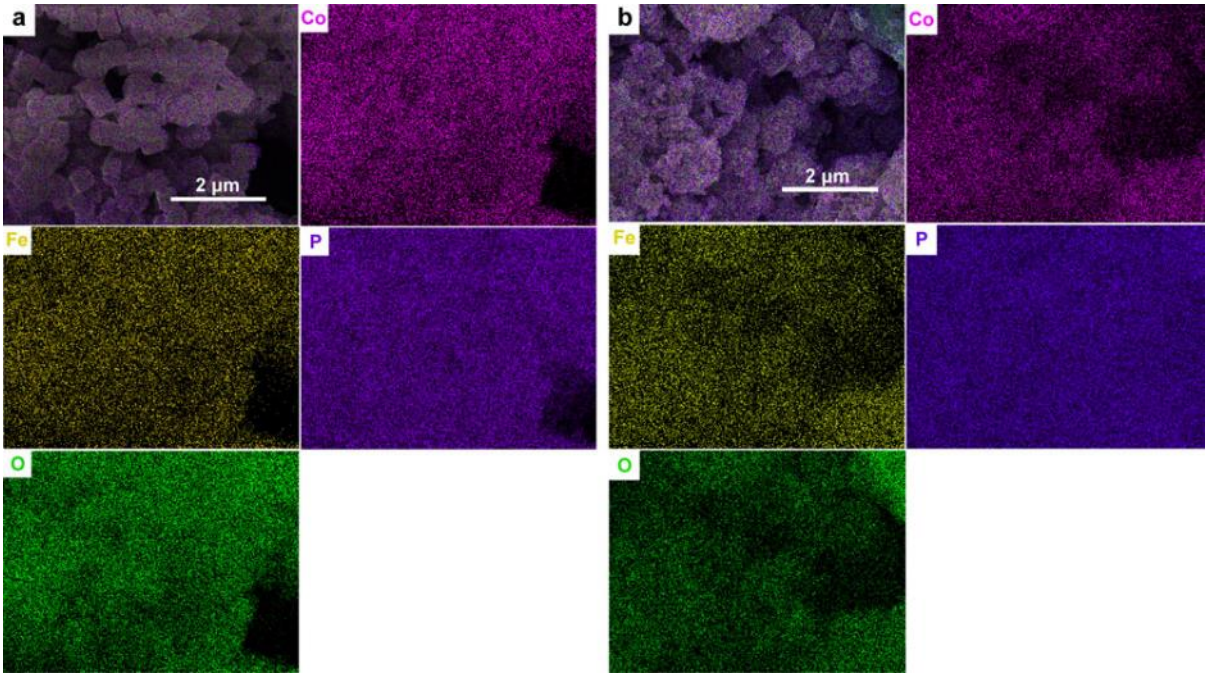

Figure S27. FESEM-EDX element mappings of as-prepared Co@CoFe-P (1-20) at different reaction temperatures: (a) 250 °C; (b) 450 °C.

3.6 Characterization of as-prepared Co-PB and Co-P

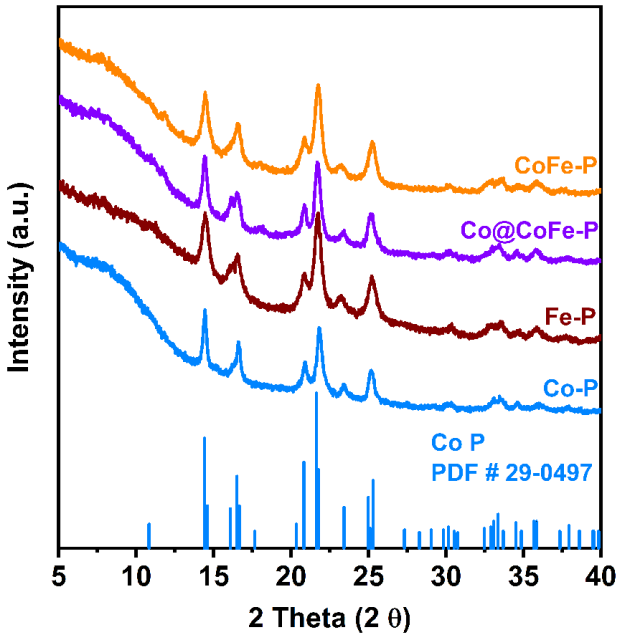

Figure S28. PXRD patterns of as-prepared Co-P, Fe-P, CoFe-P, and Co@CoFe-P (1-20).

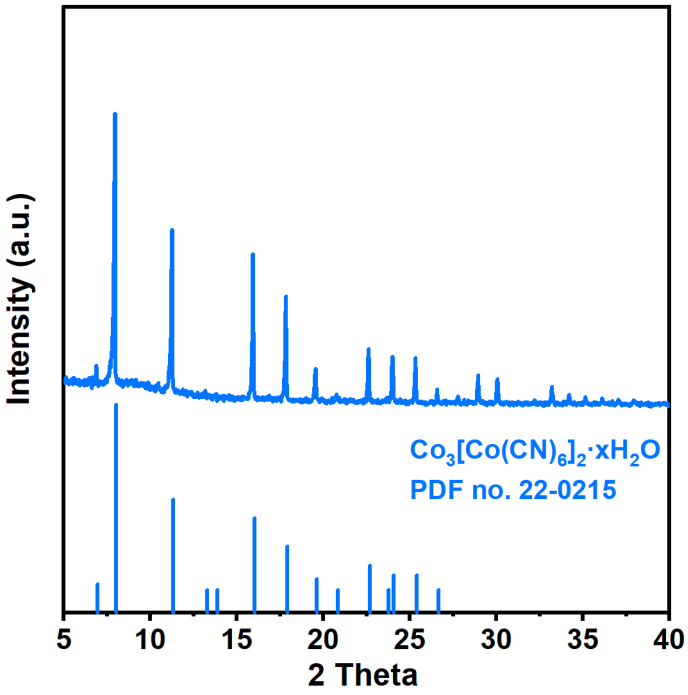

Figure S29. PXRD pattern of as-prepared Co-PB vs. theoretical pattern calculated from reference data.

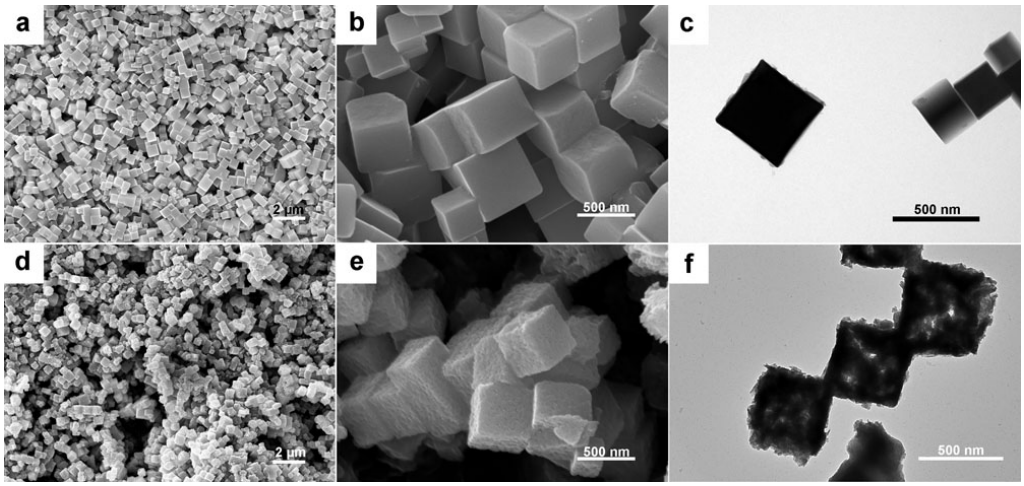

Figure S30. FESEM and TEM images of as-prepared Co-PB (a-c) and Co-P (d-f).

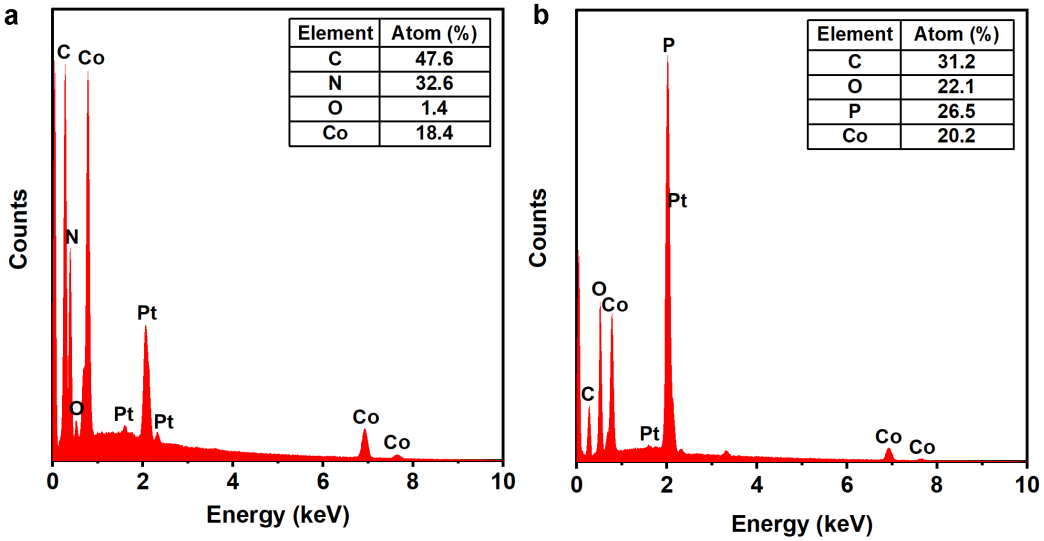

Figure S31. FESEM-EDX spectra of as-prepared Co-PB (a) and Co-P (b).

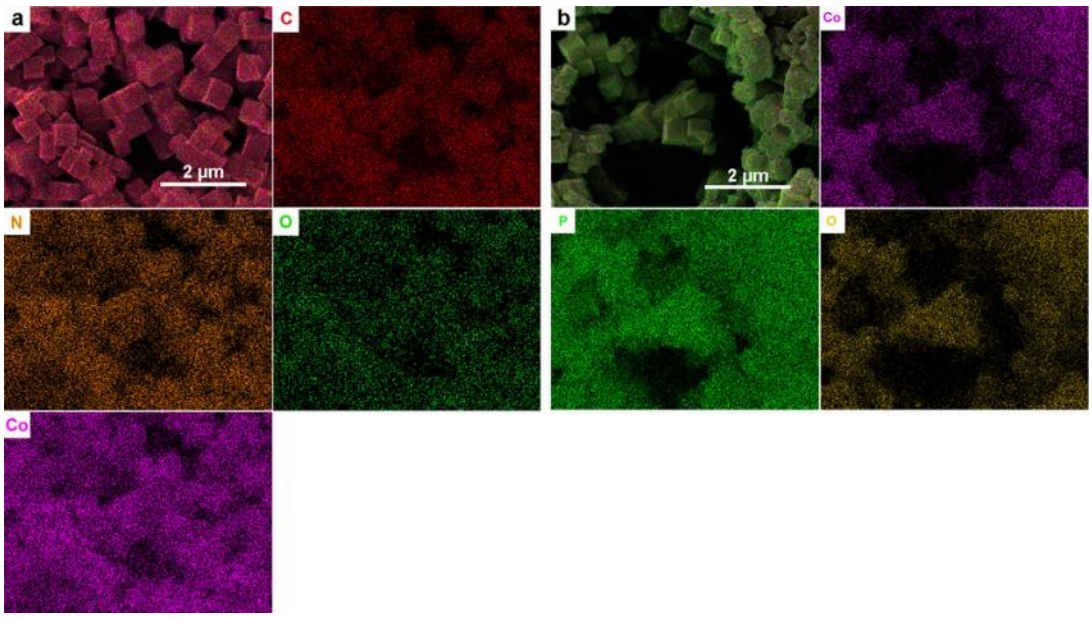

Figure S32. FESEM-EDX element mappings of as-prepared Co-PB (a) and Co-P (b).

3.7 Characterization of as-prepared Fe-PB and Fe-P

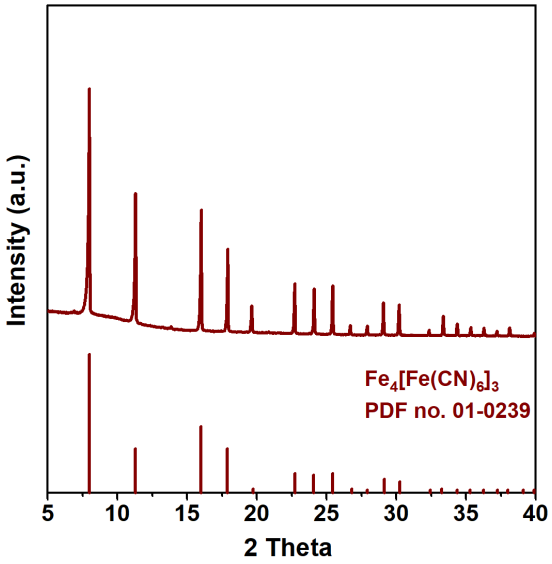

Figure S33. PXRD pattern of as-prepared Fe-PB vs. theoretical pattern calculated from database references.

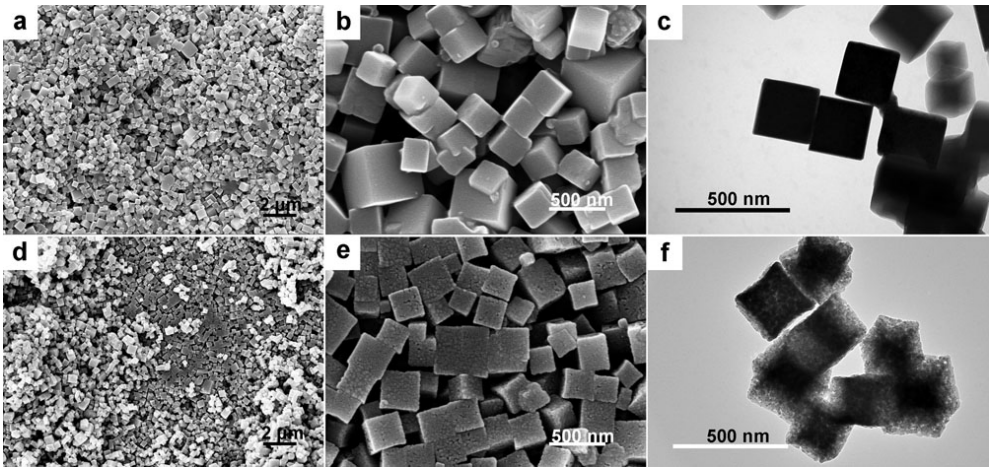

Figure S34. FESEM and TEM images of as-prepared Fe-PB (a-c) and Fe-P (d-f).

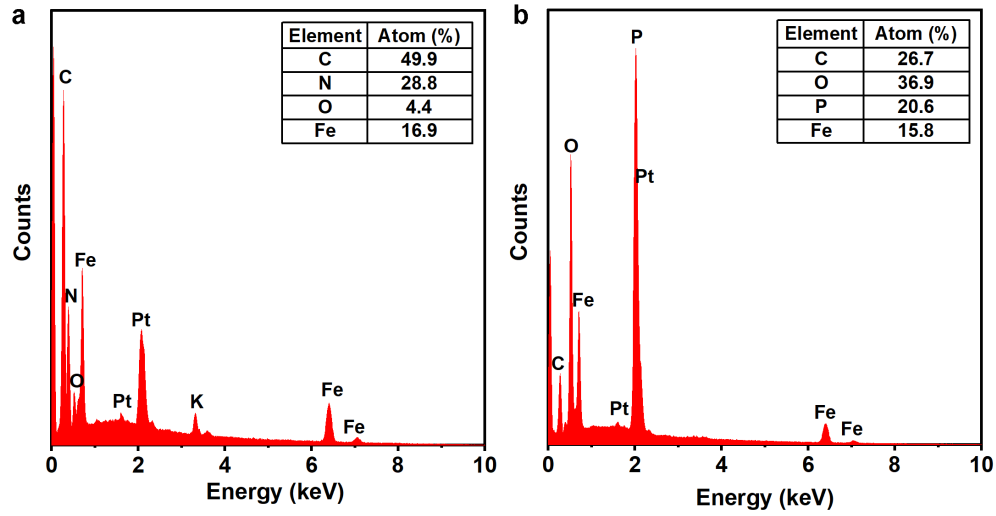

Figure S35. FESEM-EDX spectra of as-prepared Fe-PB (a) and Fe-P (b).

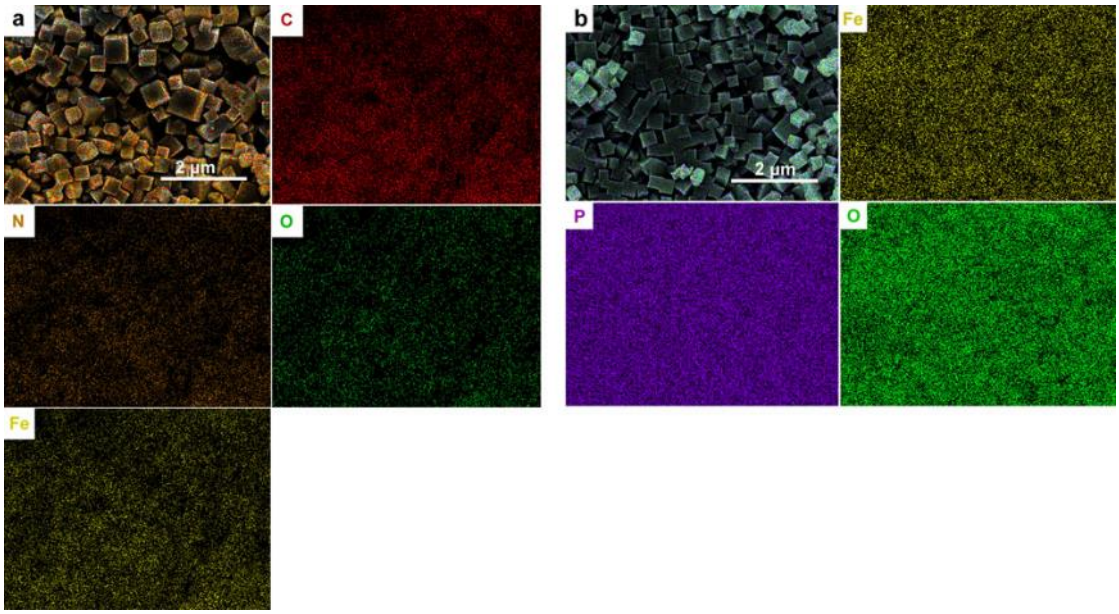

Figure S36. FESEM-EDX element mappings of as-prepared Fe-PB (a) and Fe-P (b).

3.8 Characterization of as-prepared CoFe-PB and CoFe-P

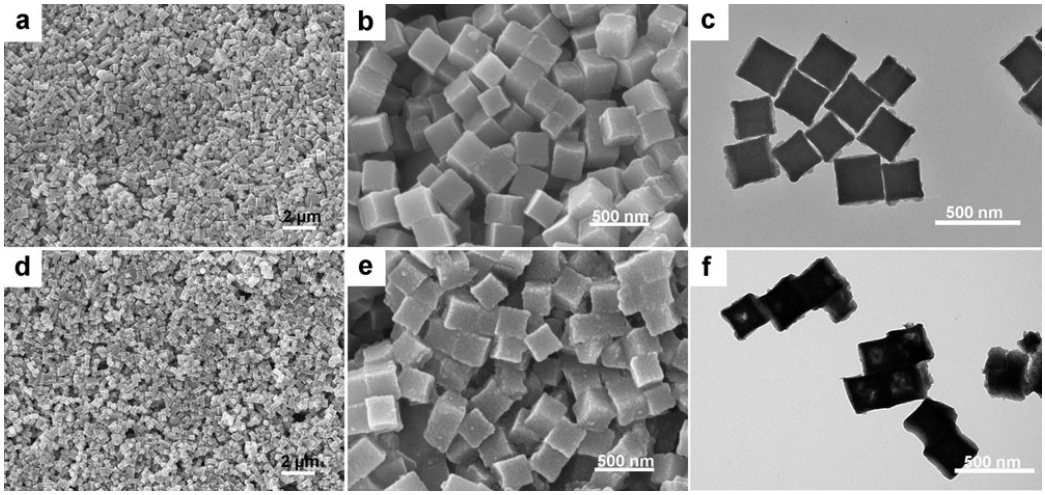

Figure S37. FESEM and TEM images of as-prepared CoFe-PB (a-c) and CoFe-P (d-f).

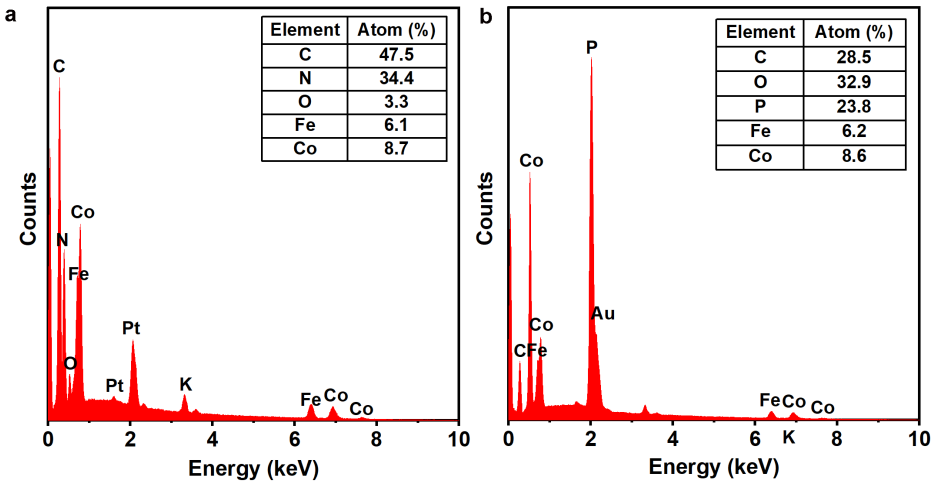

Figure S38. FESEM-EDX spectra of as-prepared CoFe-PB (a) and CoFe-P (b).

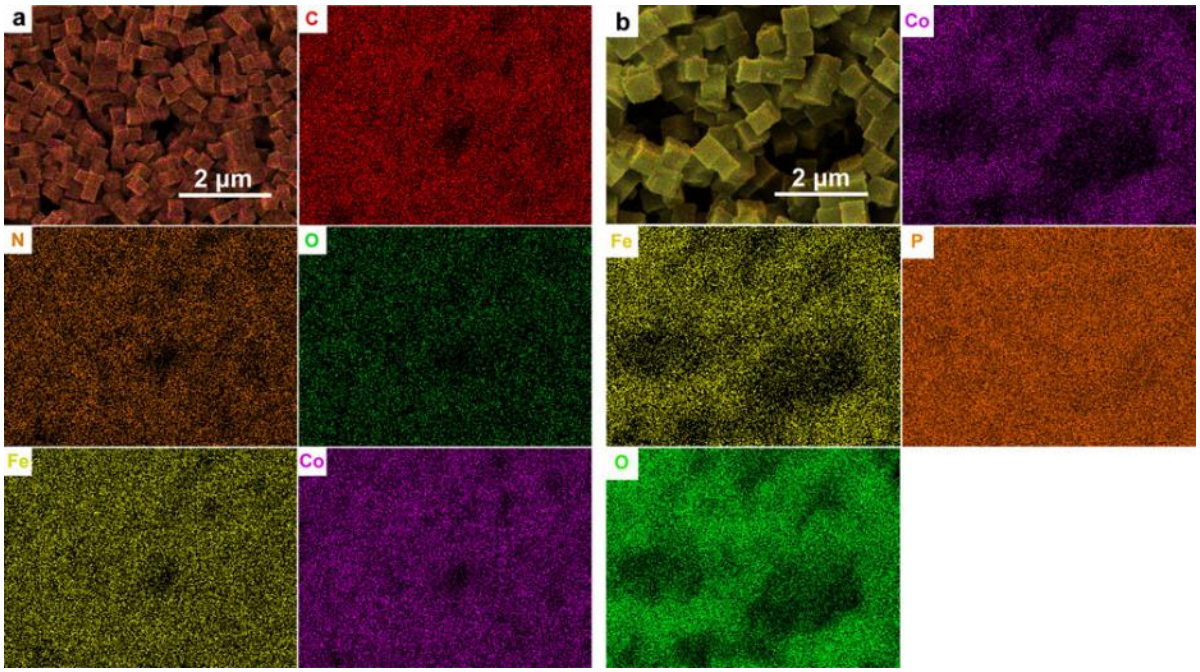

Figure S39. FESEM-EDX element mappings of as-prepared CoFe-PB (a) and CoFe-P (b).

3.9 Characterization of as-prepared Co@CoFe-O

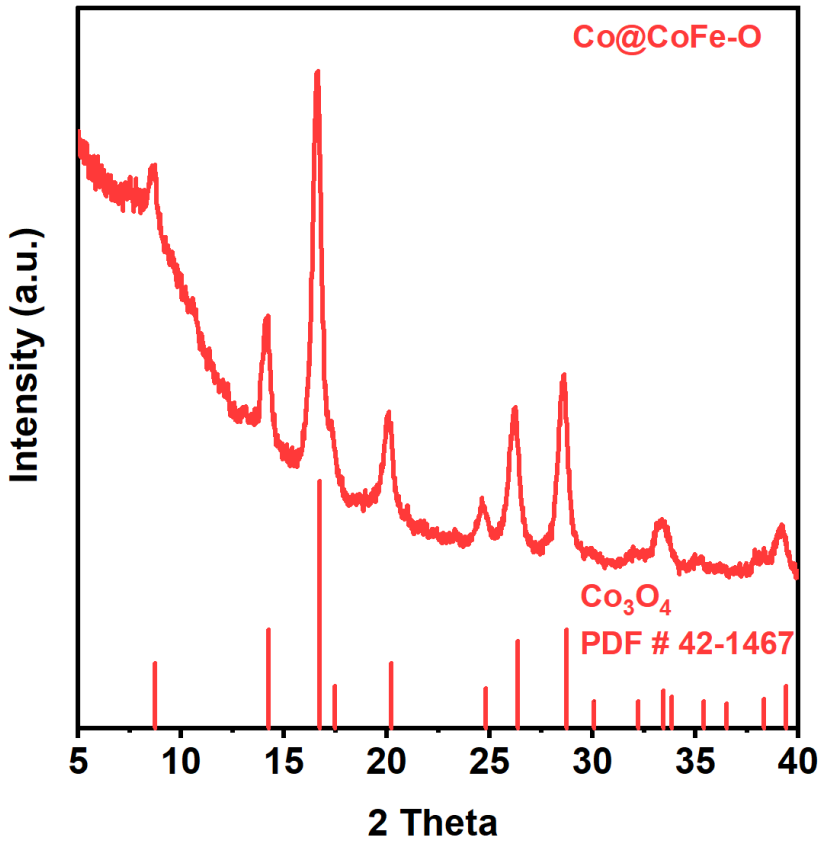

Figure S40. PXRD pattern of as-prepared Co@CoFe-O vs. theoretical pattern calculated from database reference.

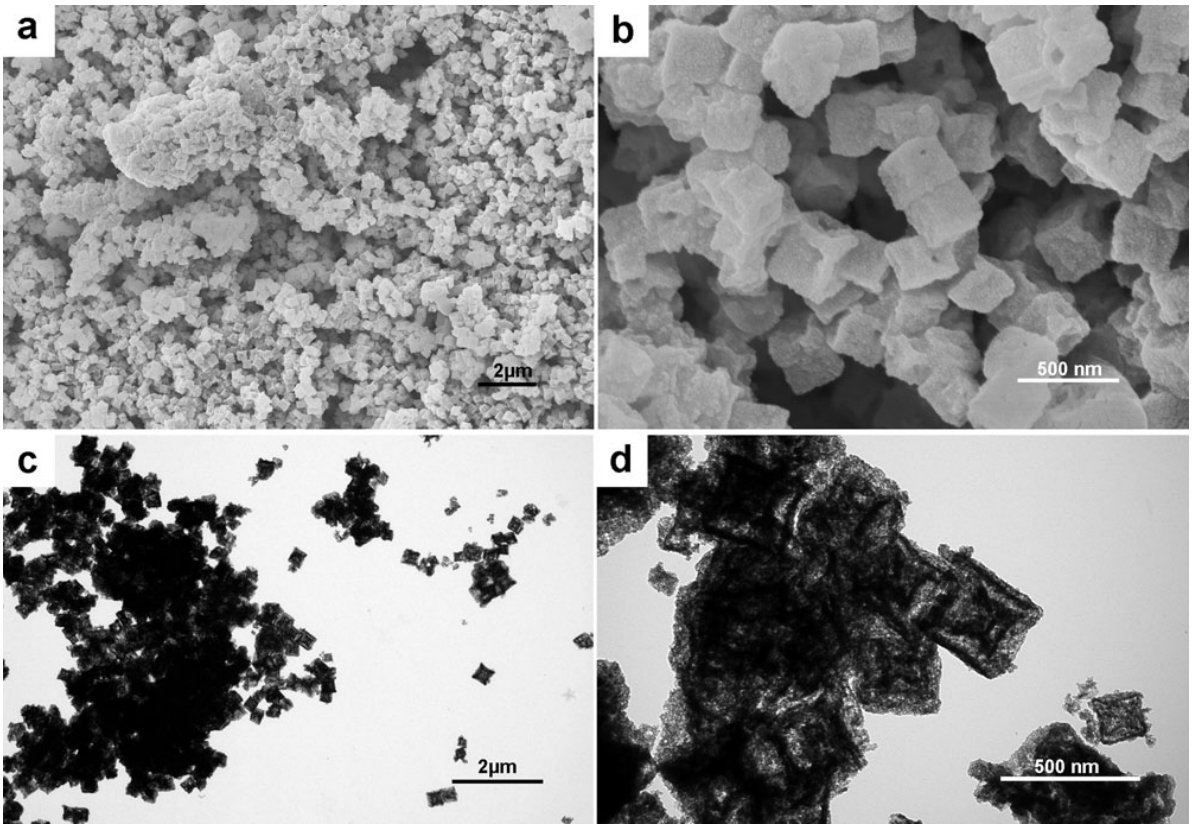

Figure S41. FESEM (a, b) and TEM (c, d) images of as-prepared Co@CoFe-O.

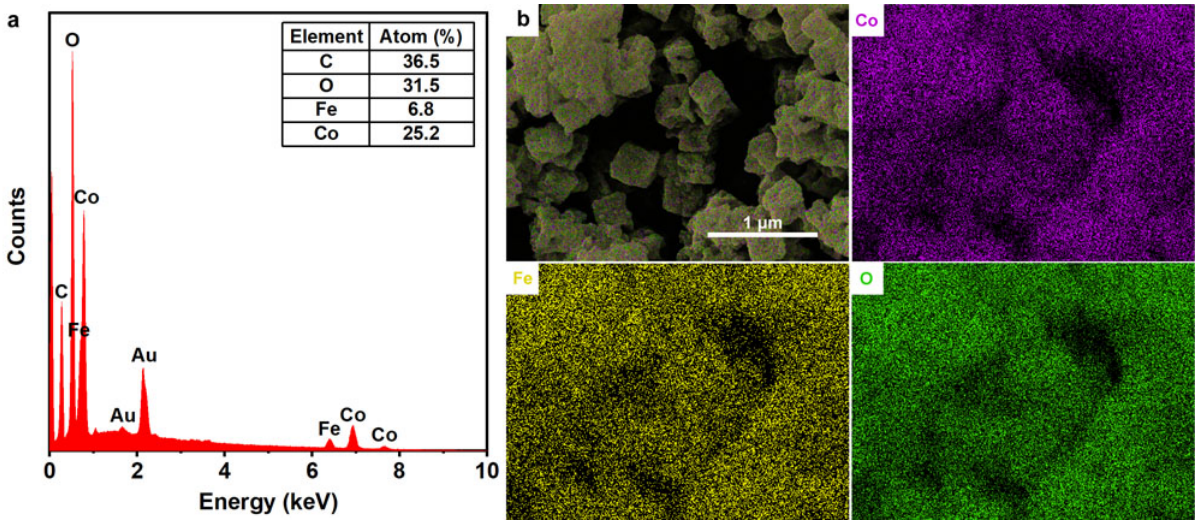

Figure S42. FESEM-EDX spectrum and element mappings of as-prepared Co@CoFe-O.

3.10 Characterization of as-prepared Co@CoFe-Se and Co@CoFe-Te

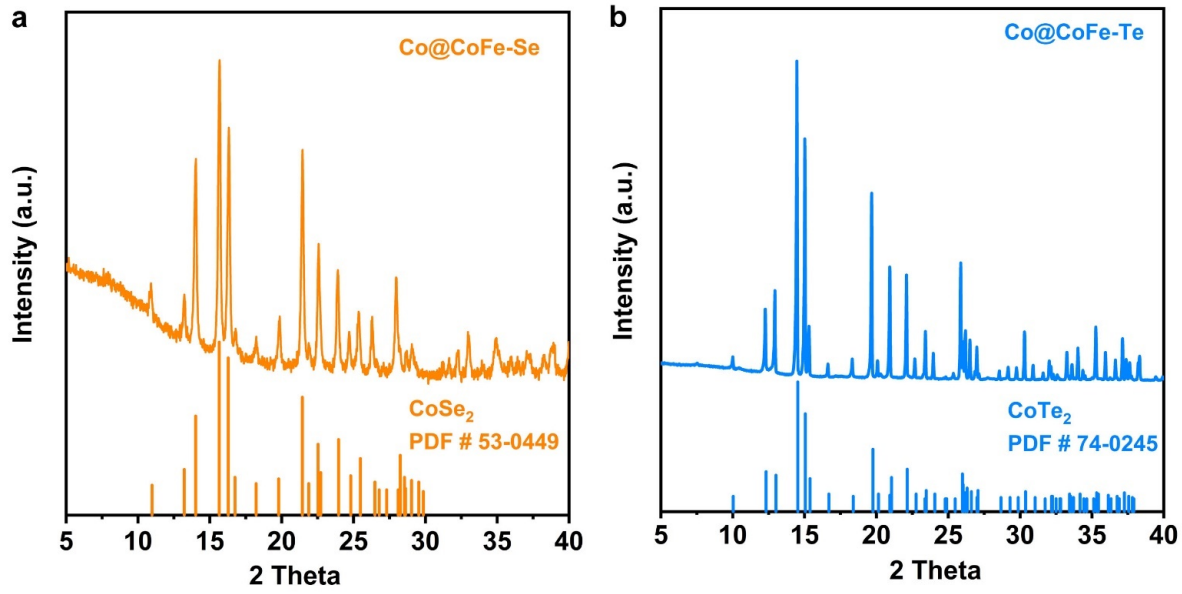

Figure S43. PXRD patterns of as-prepared Co@CoFe-Se (a) and Co@CoFe-Te (b) vs. calculated patterns.

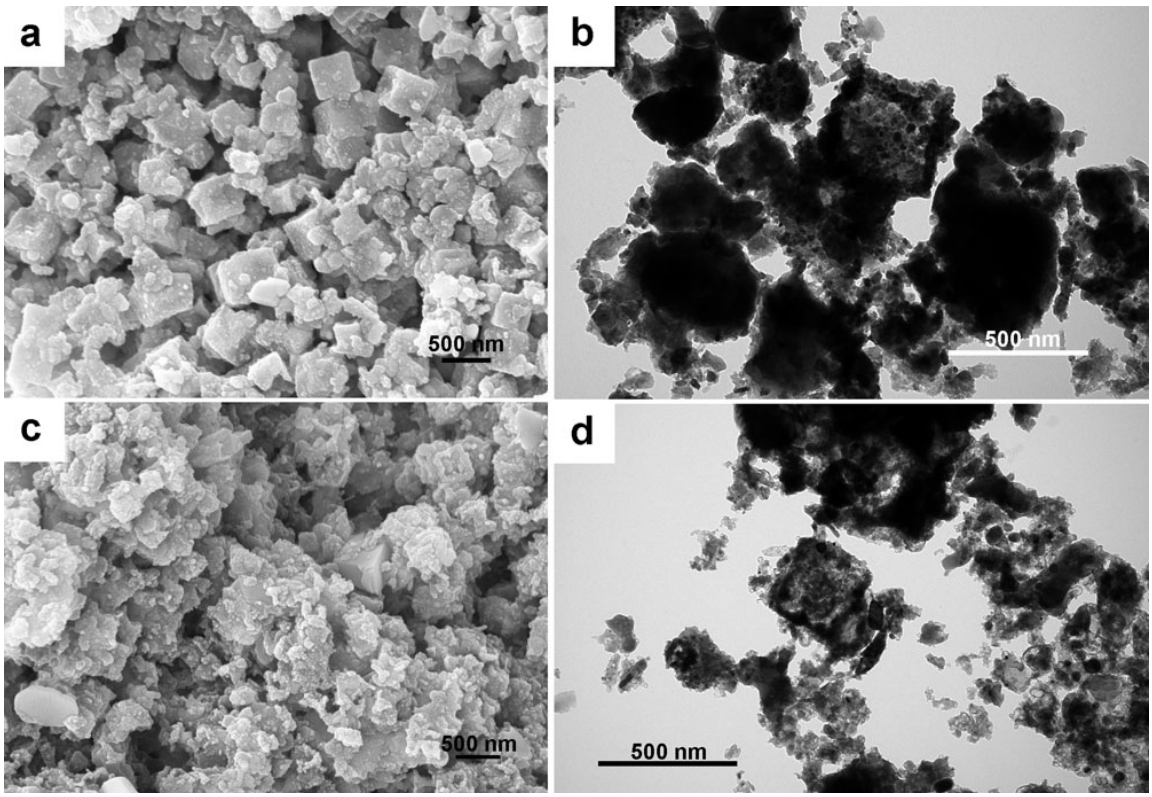

Figure S44. FESEM and TEM images of as-prepared Co@CoFe-Se (a, b) and Co@CoFe-Te (c, d).

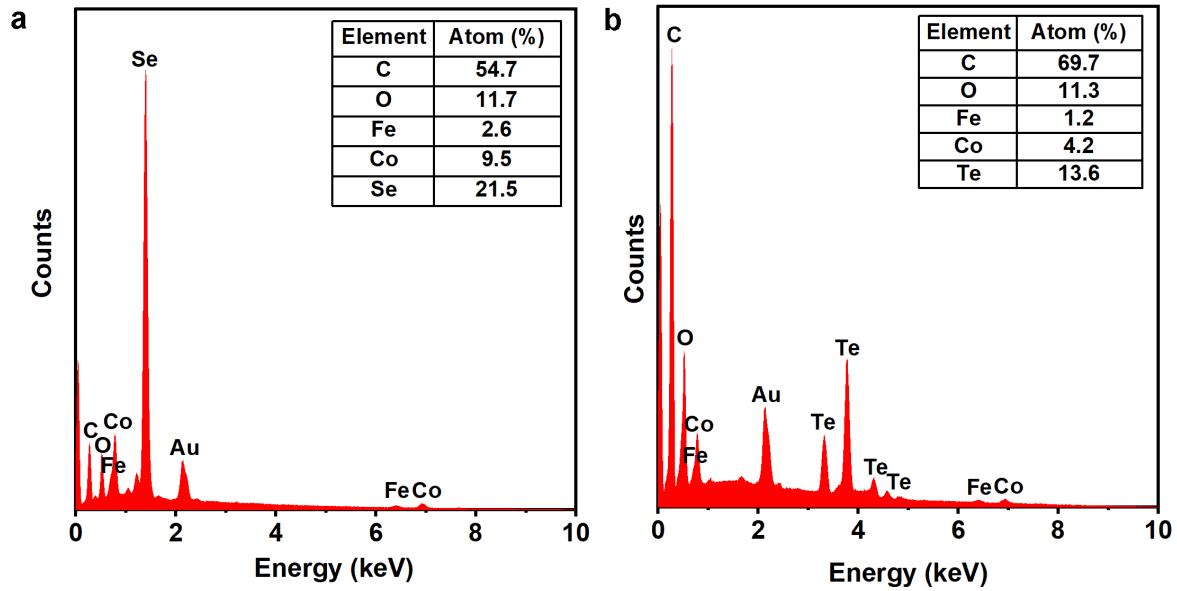

Figure S45. FESEM-EDX spectra of as-prepared Co@CoFe-Se (a) and Co@CoFe-Te (b).

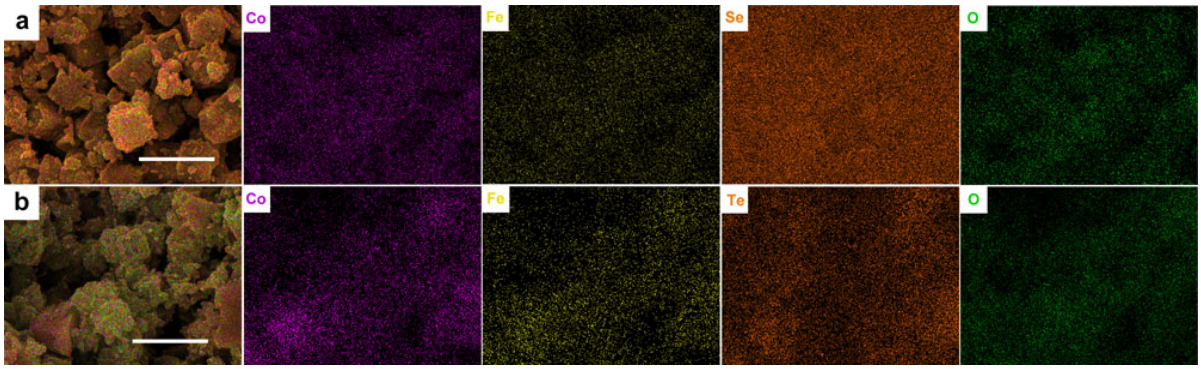

Figure S46. FESEM-EDX element mappings of as-prepared Co@CoFe-Se (a) and Co@CoFe-Te (b).

4. *Ex situ* XAS and XPS characterization of as-prepared products

4.1 XAS characterization and XANES simulations of as-prepared products

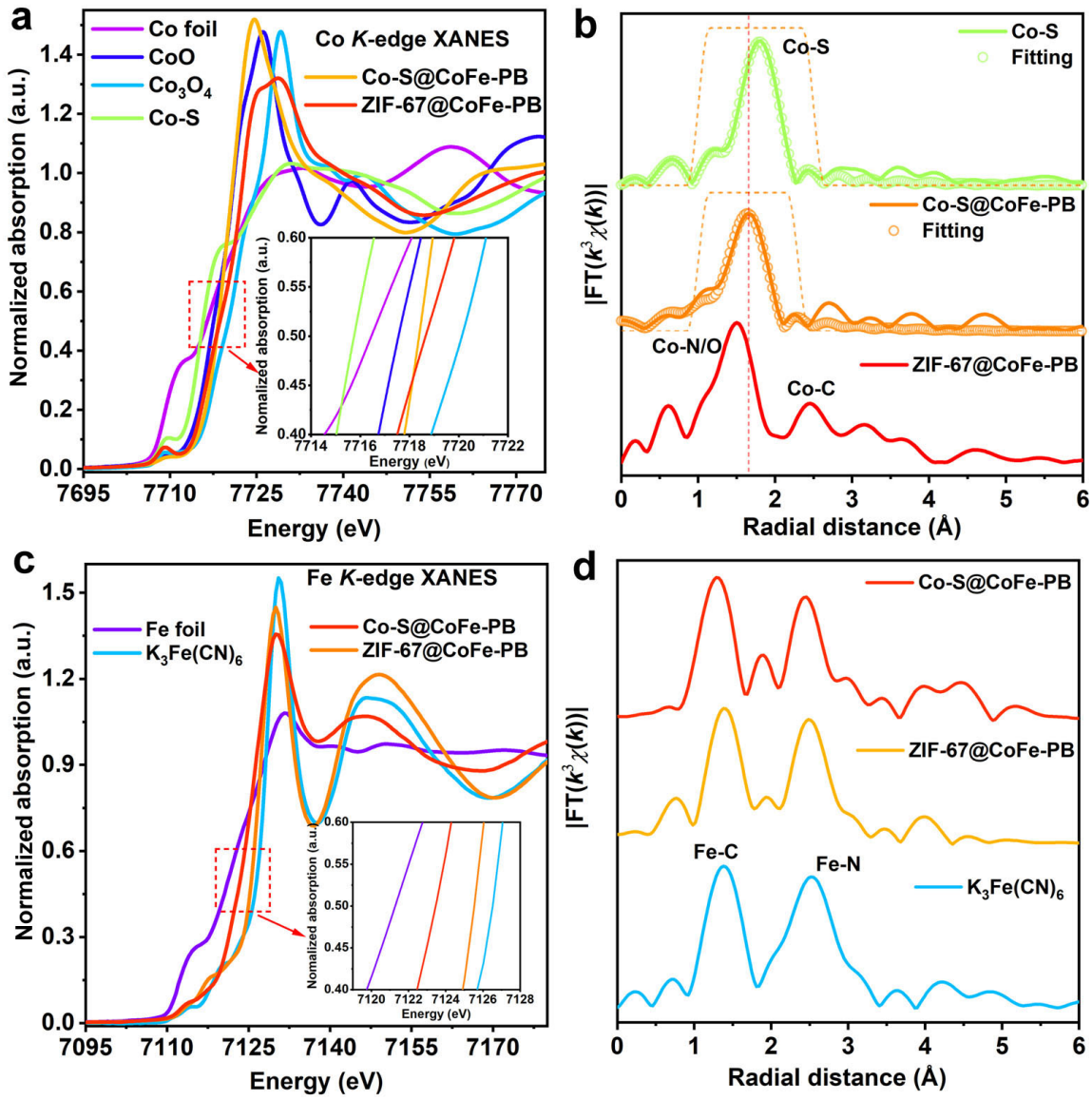

Figure S47. (a, b) Co *K*-edge XANES and FT-EXAFS spectra of Co-S, Co-S@CoFe-PB, and ZIF-67@CoFe-PB vs. references. (c, d) Fe *K*-edge XANES and FT-EXAFS spectra of Co-S@CoFe-PB and ZIF-67@CoFe-PB vs. references.

To study the impact of sulfidation on the local electronic structure of as-prepared ZIF-67@CoFe-PB NCs, Co and Fe *K*-edge XAS data were recorded for Co-S NBs, ZIF@CoFe-PB NCs, and Co-S@CoFe-PB NBs, along with the reference samples. A close inspection of the rising edge energy position in Co *K*-edge XANES spectra (**Figure S47a**) reveals that the valence states of cobalt ions follow the order Co-S<Co-S@CoFe-PB<ZIF-67@CoFe-PB. The Co *K*-edge FT-EXAFS spectrum of Co-S NBs only shows one prominent peak at 1.81 Å (**Figure S47b**), corresponding to the backscattering of the first Co-S coordination shell, in line with previous studies on cobalt sulfides.[84-86] Other than for Co-S NBs, the Co *K*-edge FT-EXAFS spectrum of ZIF-67@CoFe-PB NCs exhibits two main peaks in the range of 1-3 Å. The first peak located at 1.50 Å is associated with the backscattering of Co-N/O pairs. It should

be mentioned that the scattering difference between the first coordination shells of Co-N and Co-O cannot be distinguished here due to their similar scattering features.[33,87] The second peak at 2.45 Å is mainly ascribed to the second Co-C shell.[33,88]

For the as-prepared Co-S@CoFe-PB, only one dominant peak is observed at 1.66 Å, which is different from the Co-S shell in Co-S NBs or the Co-N/O shell in ZIF-67@CoFe-PB NCs. This suggests that the local coordination environment of Co centers in ZIF-67@CoFe-PB NCs changed after sulfidation. Moreover, the fitting of the FT-EXAFS spectrum of Co-S@CoFe-PB (**Table S5**) suggests the presence of Co-S bonds and Co-N/O bonds in the first coordination shell. Fe *K*-edge XANES spectra of ZIF-67@CoFe-PB NCs and Co-S@CoFe-PB NBs verify that the local electronic structure of Fe ions remains more or less unchanged after sulfidation. Compared with ZIF-67@CoFe-PB NCs, the rising absorption edge of Co-S@CoFe-PB NCs (**Figure S47c**) exhibits a negative energy shift, probably caused by the electronic interaction between inner shells of Co-S and outer shells of CoFe-PB.[5,89] Moreover, the FT-EXAFS spectra (**Figure S47d**) of both ZIF-67@CoFe-PB and Co-S@CoFe-PB present two similar scattering peaks, one at 1.38 Å and the other one at 2.45 Å, which correspond to the Fe-C and Fe-N bonds, respectively, as confirmed by the reference $K_3Fe(CN)_6$. All these results corroborate that only Co coordination environments were changed and that the pristine local electronic structures of Fe ions in ZIF-67@CoFe-PB were retained after sulfidation, further supporting the successful preparation of double-layered Co-S@CoFe-PB NBs.

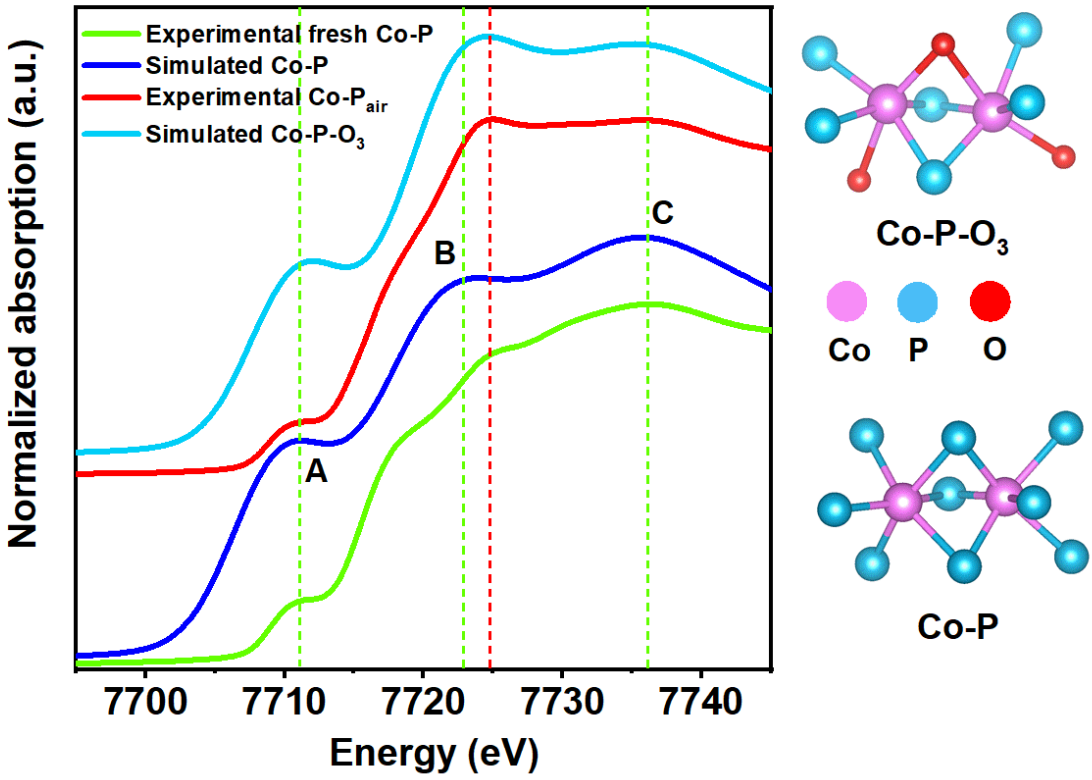

Figure S48. Co *K*-edge XANES spectra of simulated Co-P and Co-P-O_3 model structures vs. experimental XANES spectra. (Co-P_{air} refers to freshly prepared Co-P samples exposed to air for one week)

The simulated XANES spectrum of Co-P shows three main peak features at A~7711 eV, B~7723 eV, and C~7736 eV. Peak A arises from quadrupolar transitions from Co 1s to Co 3d orbitals and reflects the intrinsic metallic properties of Co-P.[90-92] Peak B is attributed to the

dipolar transitions from Co 1s to P 3p orbitals. The dipolar transitions from Co 1s to Co 4p orbitals contribute to peak C. The experimental spectrum of Co-P reproduces the simulated one well, except for the slight shift to positive energy observed at B~7725 eV (simulated B~7723 eV). Results in **Figure 1p and Figure S20** indicate that P anions can be easily oxidized to PO_x moieties,[32,46,76,93] resulting in the formation of new metal-oxygen bonds, which might influence the absorption features of peak B. To study this structural variation, we recorded the XANES spectra for Co-P NBs samples that were exposed to air for 1 week, denoted as Co-P_{air} (**Figure S48**). Results show an increase in the intensity and energy position of the peak B~7725 eV in Co-P_{air} compared with that of the simulated XANES spectrum of Co-P. Based on our above discussions, these may arise from the interaction between Co-O and Co-P bonds in Co-P NBs. To corroborate this hypothesis, the XANES spectrum of a Co-P sample with partial O substitution (denoted as Co-P-O_3) was further calculated (**Figure S48)**. The simulated XANES spectrum of Co-P-O_3 reproduces the experimental spectrum of Co-P_{air} well, which shows a similar energy position of peaks A to C and intensity ratio between the peaks B and C. Further evidence is that partial incorporation of oxygen into the Co-P lattice influences the dipolar transitions from Co 1s to P 3p and affects the absorption features of peak B. Moreover, the existence of metal-oxygen bonds in Co-P NBs only influences the coordination environments of Co centers, but it does not affect its pristine crystal structure (**see discussion of Figure S49**).

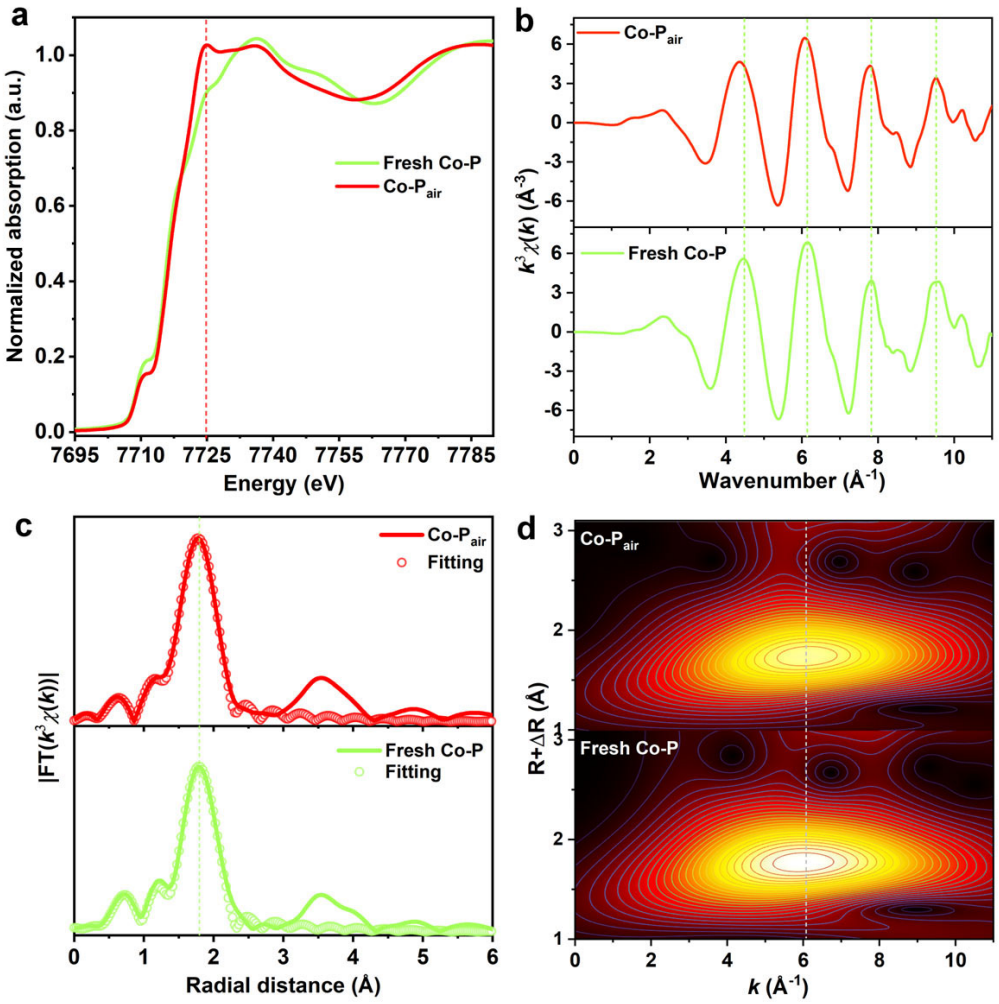

Figure S49. (a) Co *K*-edge XANES spectra of fresh Co-P and Co-P_{air}. (b, c) Co *K*-edge EXAFS and FT-EXAFS spectra of two samples. (d) WT contour profiles of fresh samples and of a sample exposed to air.

Figure S49a displays the Co *K*-edge XANES spectra of freshly prepared Co-P and of Co-P_{air}. The XANES spectrum of Co-P_{air} shows a similar line shape compared with that of fresh Co-P in the rising absorption range, except for a much higher peak intensity appearing at around 7725 eV in Co-$P_{air.}$ Based on the XANES spectra simulations in **Figure S48**, the appearance of the prominent peak feature at around 7725 eV is mainly attributed to the increasing number of Co-O bonds in Co-P_{air} compared with that of fresh Co-P. This is confirmed by the slightly positive energy shift in the rising absorption edge (**Figure S49a**), indicating an increase of the oxidation state of Co ions in Co-P_{air}. EXAFS and FT-EXAFS spectra were further acquired to investigate the local coordination environments of Co centers in the investigated samples. As depicted in **Figure S49b**, the EXAFS oscillations of fresh Co-P and Co-P_{air} are quite similar in the investigated k ranges of 0 to 11 $Å^{-1}$, revealing a very closely related local coordination environment of Co centers in the investigated samples. As anticipated, the FT-EXAFS spectrum (**Figure S49c**) of Co-P_{fresh} exhibits only one dominant peak at 1.78 Å, which agrees with that of fresh Co-P. Furthermore, the wavelet-transform (WT) contour plots (**Figure S49d**) of two samples were investigated. The relative magnitude of the most intense maximum, ascribed to the first Co-P shell, decreases from Co-P to Co-P_{air}, indicating weaker scattering contributions from first Co-P shells in Co-P_{air} samples compared with those of fresh Co-P. The fitting of FT-EXAFS spectra (**Table S5**) demonstrates that the coordination number of the first Co-P shell (CN_{Co-P}) decreases from 5.79 in fresh Co-P to 5.15 in Co-P_{air}. In comparison, the CN_{Co-O} shows an increasing trend from 0.30 in fresh Co-P to 0.82 in Co-P_{air}. Due to the slightly higher atomic weight of P than O, the backscattering from the first Co-O shells was suppressed by the first Co-P shells in the FT-EXAFS spectra.[94] This explains why the Co-P_{air} sample shows similar EXAFS and FT-EXAFS spectra but with a weakened intensity maximum in the WT contour plot compared with that of fresh Co-P.

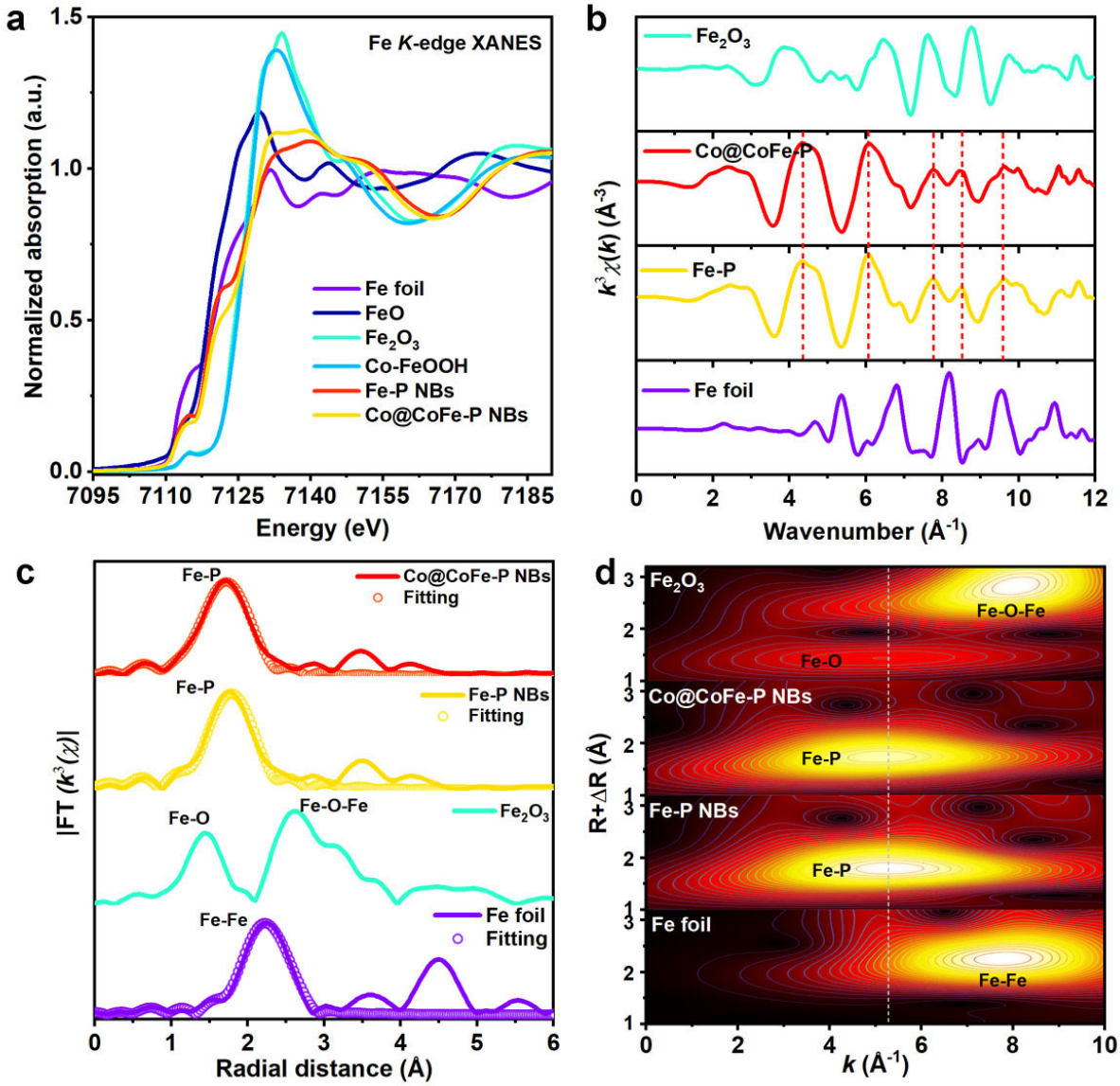

Figure S50. (a) Fe *K*-edge XANES spectra of as-synthesized samples versus references. (b) Fe *K*-edge EXAFS spectra of as-synthesized samples vs. references. (c) Fitting of the Fe *K*-edge FT-EXAFS spectra of as-synthesized samples vs. references. (d) Fe *K*-edge WT contour profiles of as-synthesized samples vs. references.

Ex situ Fe *K*-edge XAS data further corroborate the presence of similar coordination environments of Fe centers in as-prepared Fe-P NBs and Co@CoFe-P NBs (**Figure S50**). As shown in **Figure S50a**, the energy positions of rising absorption edges of Fe-P NBs and Co@CoFe-P NBs are close to that of FeO, suggesting that the average valence states of Fe in both samples are nearly +2. However, we observe that the rising absorption edge of as-prepared Co@CoFe-P NBs is slightly shifted to higher energy. Moreover, the peak intensity at ~7134 eV increases slightly compared with that of Fe-P NBs, indicating that the average valence state of Fe in Co@CoFe-P NBs is slightly higher than that of Fe-P NBs. From the fitting of FT-EXAFS spectra and the WT contour plots (**Figure S50c,d and Table S5**), the as-synthesized Co@CoFe-P NBs show an expected higher CN_{Fe-O} of 1.34 compared with that of Fe-P NBs (0.75). All of the above XAS results (**Figure 2 and Figure S50**) point to the presence of unsymmetrical Co/Fe-$P_{6-x}O_x$ moieties in the as-prepared Co@CoFe-P NBs.

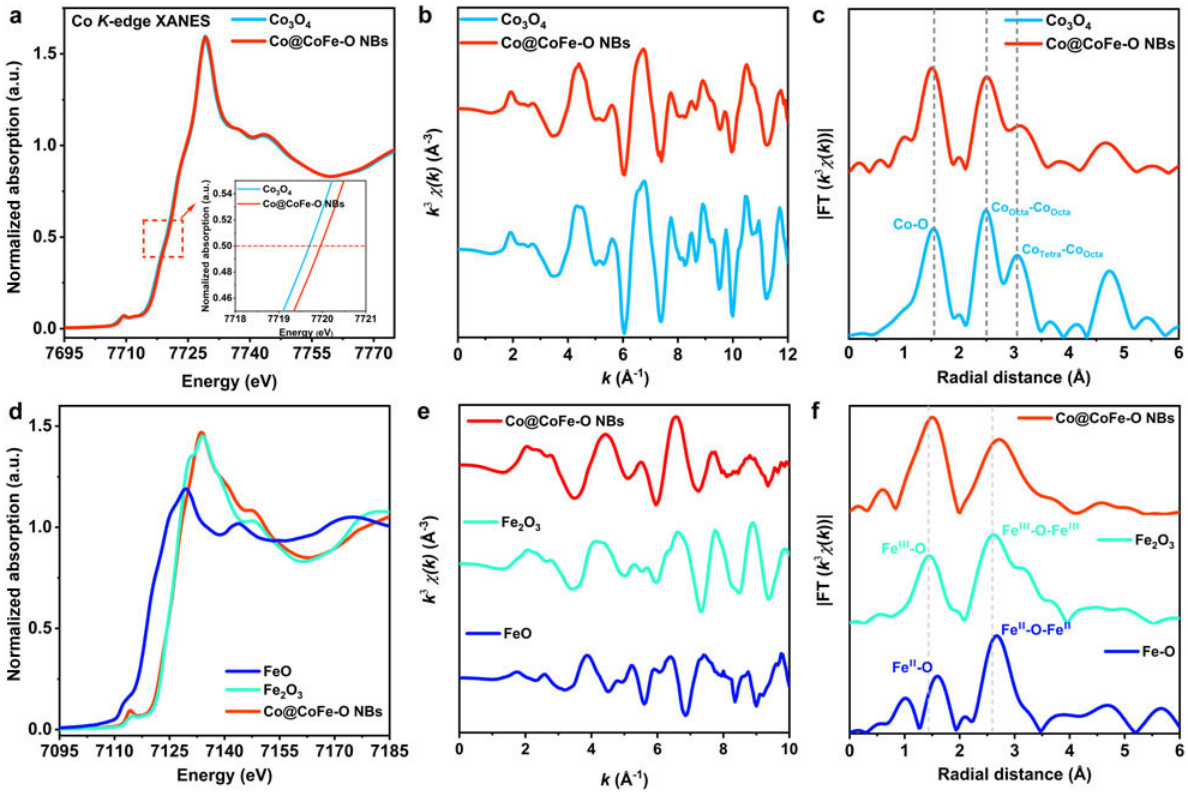

Figure S51. (a) Co *K*-edge XANES spectra of Co@CoFe-O NBs vs. references. (b, c) Co *K*-edge EXAFS and FT-EXAFS spectra of Co@CoFe-O NBs vs. references. (d) Fe *K*-edge XANES spectra of Co@CoFe-O NBs vs. references. (e, f) Fe *K*-edge EXAFS and FT-EXAFS spectra of Co@CoFe-O NBs vs. references.

Evaluation of the Co *K*-edge XAS data (**Figures S51a-c**) shows that the as-prepared Co@CoFe-O NBs match well with the Co_3O_4 reference, verifying the similar coordination environments of Co centers in both samples. However, the rising absorption edge position of the Co *K*-edge XANES spectrum for Co@CoFe-O NBs shows a slightly positive energy shift compared with the Co_3O_4 reference, which is possibly due to the presence of oxygen nonstoichiometries after Fe substitution.[95,96] In addition, the line shape of the Fe *K*-edge XANES spectrum (**Figure S51d**) of Co@CoFe-O NBs is different from FeO but overlaps well with the Fe_2O_3 reference. This finding implies that the valence state of Fe cations in Co@CoFe-O NBs is mainly +3. Further, the EXAFS oscillation (**Figure S51e**) in the k range from 0 to 10 $Å^{-1}$ for Co@CoFe-O NBs presents a similar trend with reference Fe_2O_3, suggesting that the local coordination environment of Fe centers in Co@CoFe-O NBs arises from a related connection of $\{FeO_6\}$ octahedra. Based on the above analysis, we conclude that partial substitution of Co by Fe in Co@CoFe-O NBs does not influence the host spinel crystal structure or the octahedral coordination of Fe centers.

4.2 XPS characterization of as-prepared products

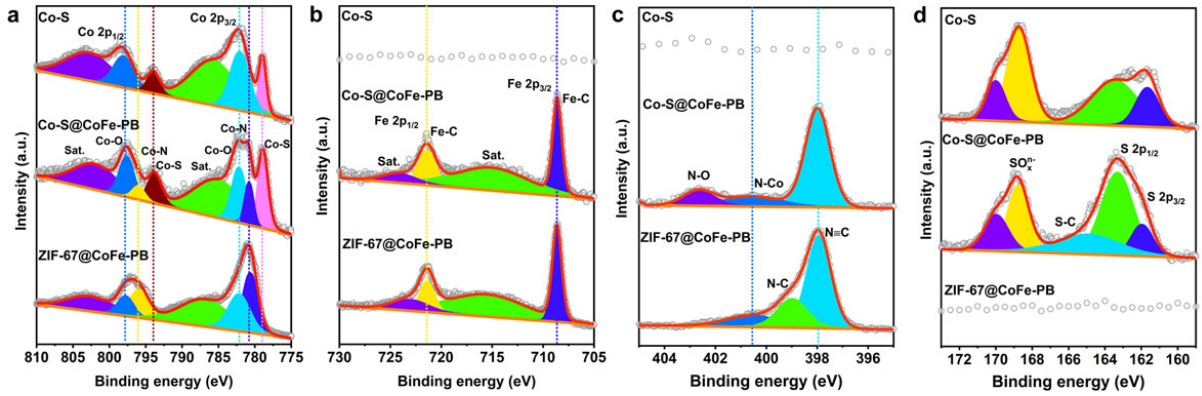

Figure S52. High-resolution XP spectra of ZIF-67@CoFe-PB, Co-S@CoFe-PB, and Co-S. (a) Co 2p. (b) Fe2p. (c) N1s. (d) S2p.

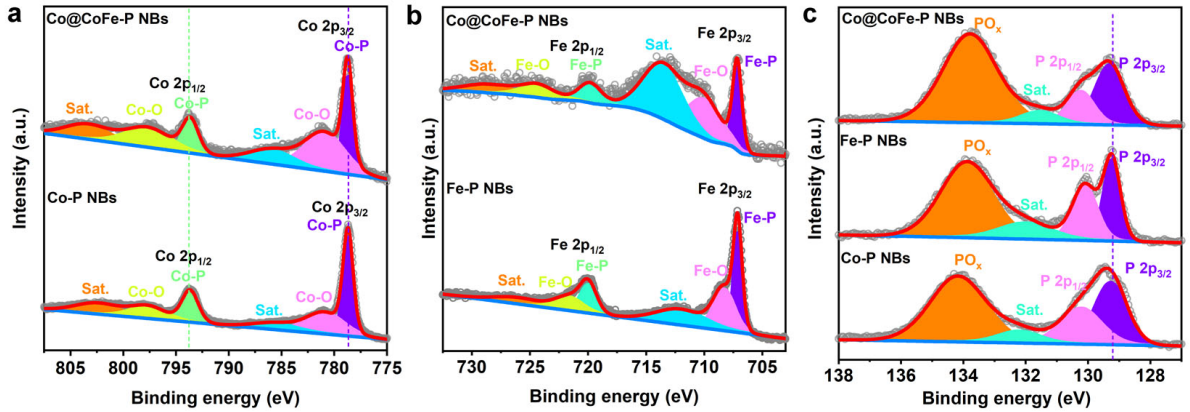

Figure S53. (a-c) High-resolution XP spectra of Co 2p, Fe2p, and P 2p for as-prepared Co-P NBs, Fe-P NBs, and Co@CoFe-P NBs.

The surface oxidation states of the synthesized ZIF-67@CoFe-PB NCs, Co-S NBs, and Co-S@CoFe-PB NBs were first examined by the deconvoluted high-resolution Co 2p, Fe2p, N1s, and S 2p (**Figure S52**) XP spectra. The XPS results (**Figure S52a**) imply the presence of Co-N (780.65V eV for Co $2p_{2/3}$ and 796.10 eV for $Co2p_{1/3}$) and of Co-S bonds (779.05V eV for Co $2p_{2/3}$ and 794.10 eV for $Co2p_{1/3}$) in the Co 2p regions,[86] Fe-C bonds (708.65 eV for Fe $2p_{2/3}$ and 721.50 eV for Fe $2p_{1/3}$) in the Fe 2p regions (**Figure S52b**),[5] N-C bonds (397.97 eV) in the N 1s regions (**Figure S52c**),[7] and S-Co bonds (162.00 eV for S $2p_{2/3}$ and 163.35 eV for S $2p_{1/3}$) in the S 2p regions (**Figure S52d**),[85] in agreement with our previous XAS analyses (**Figure S47**). The surface chemical valence states in Co-P NBs, Fe-P NBs, and Co@CoFe-P NBs were also examined. As illustrated in **Figure S53a**, the Co centers in Co@CoFe-P NBs display comparable surface electronic structures with those in Co-P NBs. Specifically, both Co-P and Co@CoFe-P NBs feature Co $2p_{3/2}$ and Co $2p_{1/2}$ core-level emissions. Moreover, the peaks located at around 778.75 and 793.80 eV, 781.15, and 797.75 eV are attributed to Co-O and Co-P bonds, respectively.[32,46,76,85] The presence of Fe-O and Fe-P bonds is evident from XP spectra of Fe 2p in Fe-P NBs and Co@CoFe-P NBs (**Figure S53b**). From the P 2p orbitals (**Figure S53c**), we observe that the as-prepared phosphide products comprise three main peaks. The first two peaks located at approximately 129.30 eV and 130.20 eV are corresponding to the P $2p_{3/2}$ and P $2p_{1/2}$, respectively, from M-P bonds (M=Co, Fe), and another peak located at 133.75 eV is arising from the high valence state of P ions in PO_x.[37,81] In addition, the ratios of peak areas

between M-P bonds and PO_x in Co@CoFe-P NBs (0.54) are lower than in Co-P NBs (0.95) and Fe-P NBs (0.83), suggesting that more oxygen atoms are incorporated into the crystal lattice of Co@CoFe-P NBs.

5. Electrochemical performance

5.1 HER and OER performance of as-prepared products

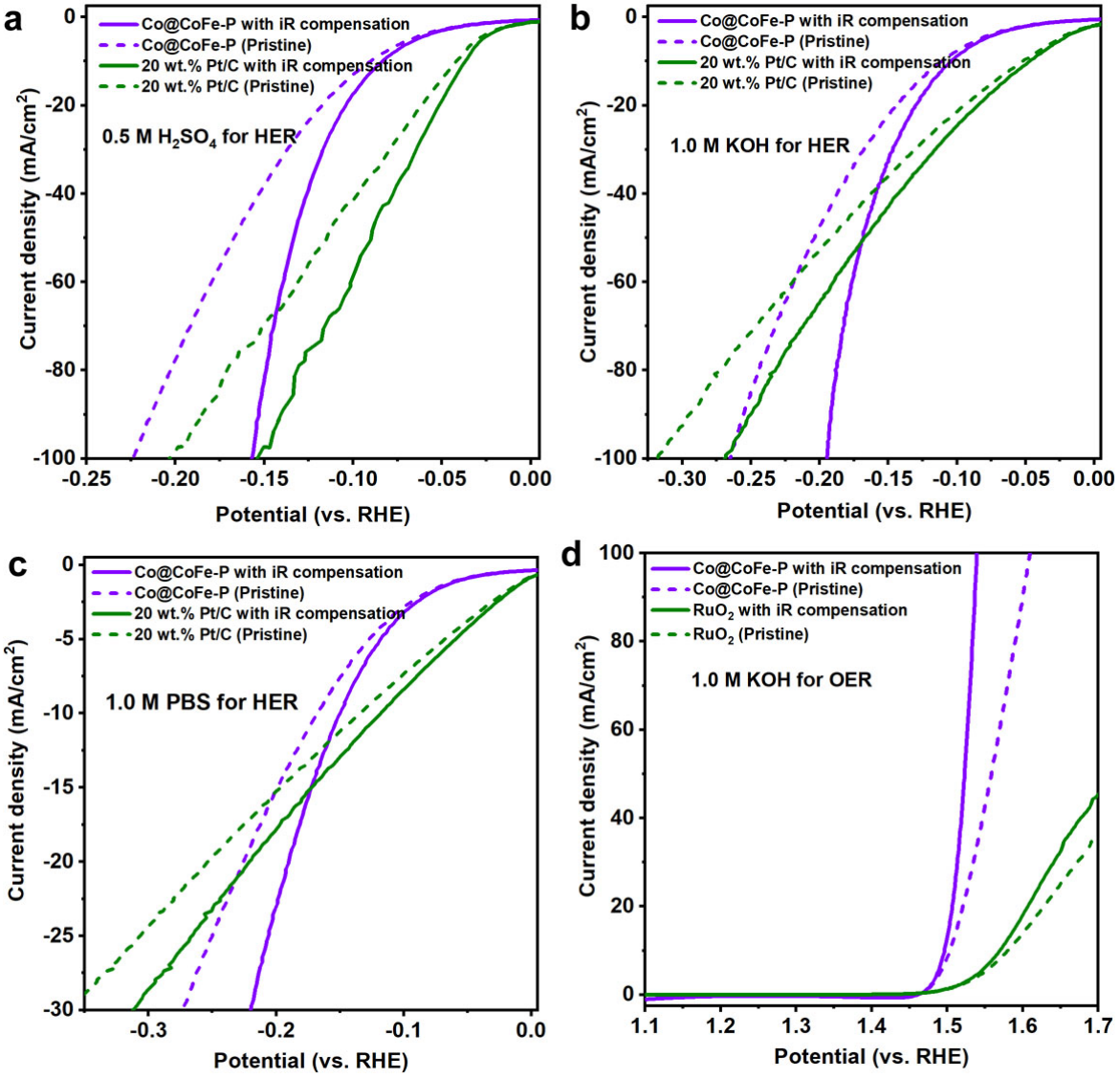

Figure S54. LSV curves before and after 90% iR-correction: (a) Co@CoFe-P (1-20) and 20 wt.% Pt/C for HER in 0.5 M H_2SO_4; (b) Co@CoFe-P (1-20) and 20 wt.% Pt/C for HER in 1.0 M KOH; (c) Co@CoFe-P (1-20) and 20 wt.% Pt/C for HER in 1.0 M PBS; (d) Co@CoFe-P (1-20) and RuO_2 for OER in 1.0 M KOH.

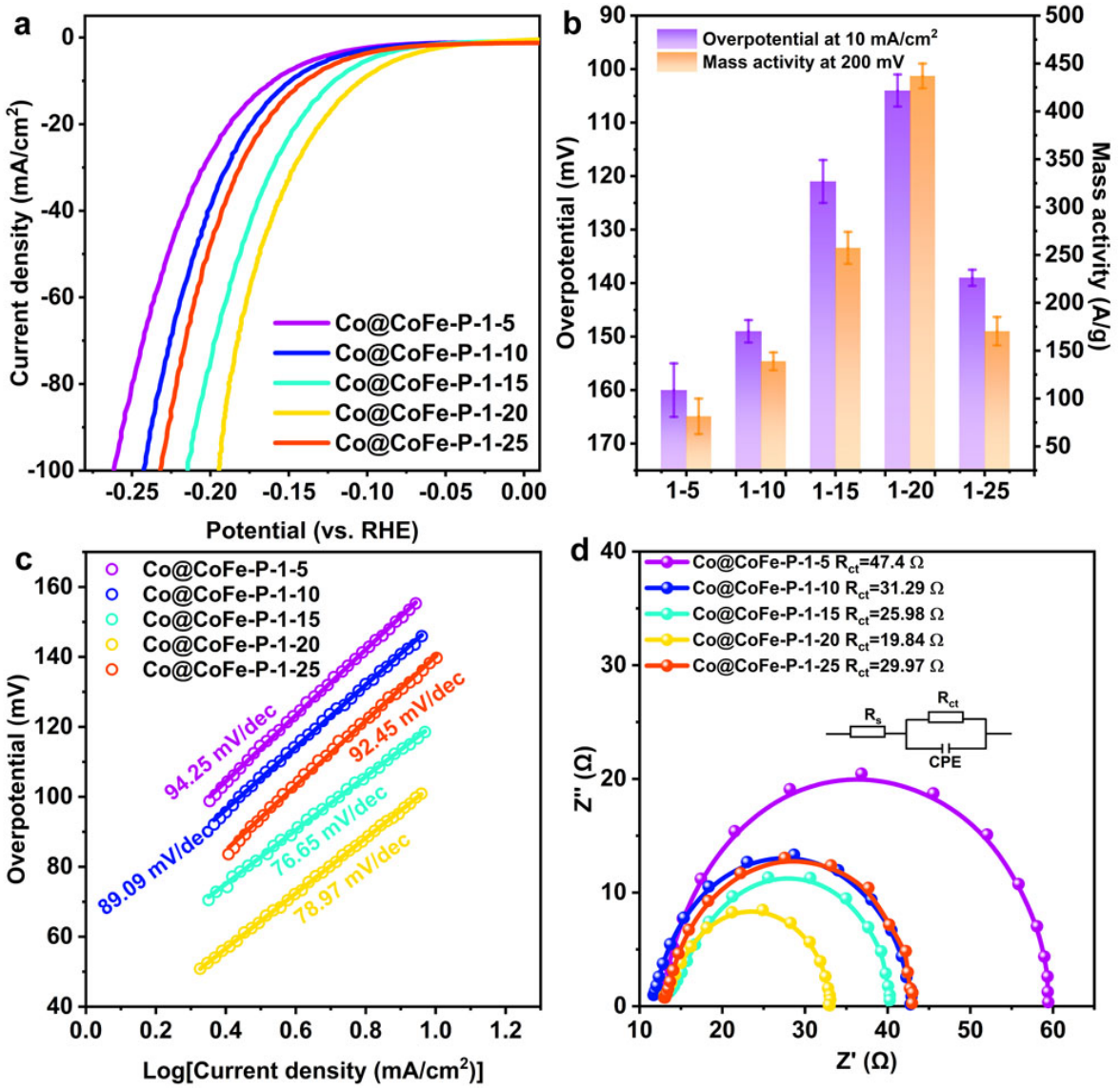

Figure S55. Electrocatalytic performance of Co@CoFe-P with different amounts of NaH_2PO_2 in 1.0 M KOH for HER. (a) LSV curves. (b) Comparison of overpotential at 10 mA/cm^2 and mass activities (at an overpotential of 200 mV) of five catalysts. (c) Tafel plots. (d) Nyquist plots (at an overpotential of 150 mV).

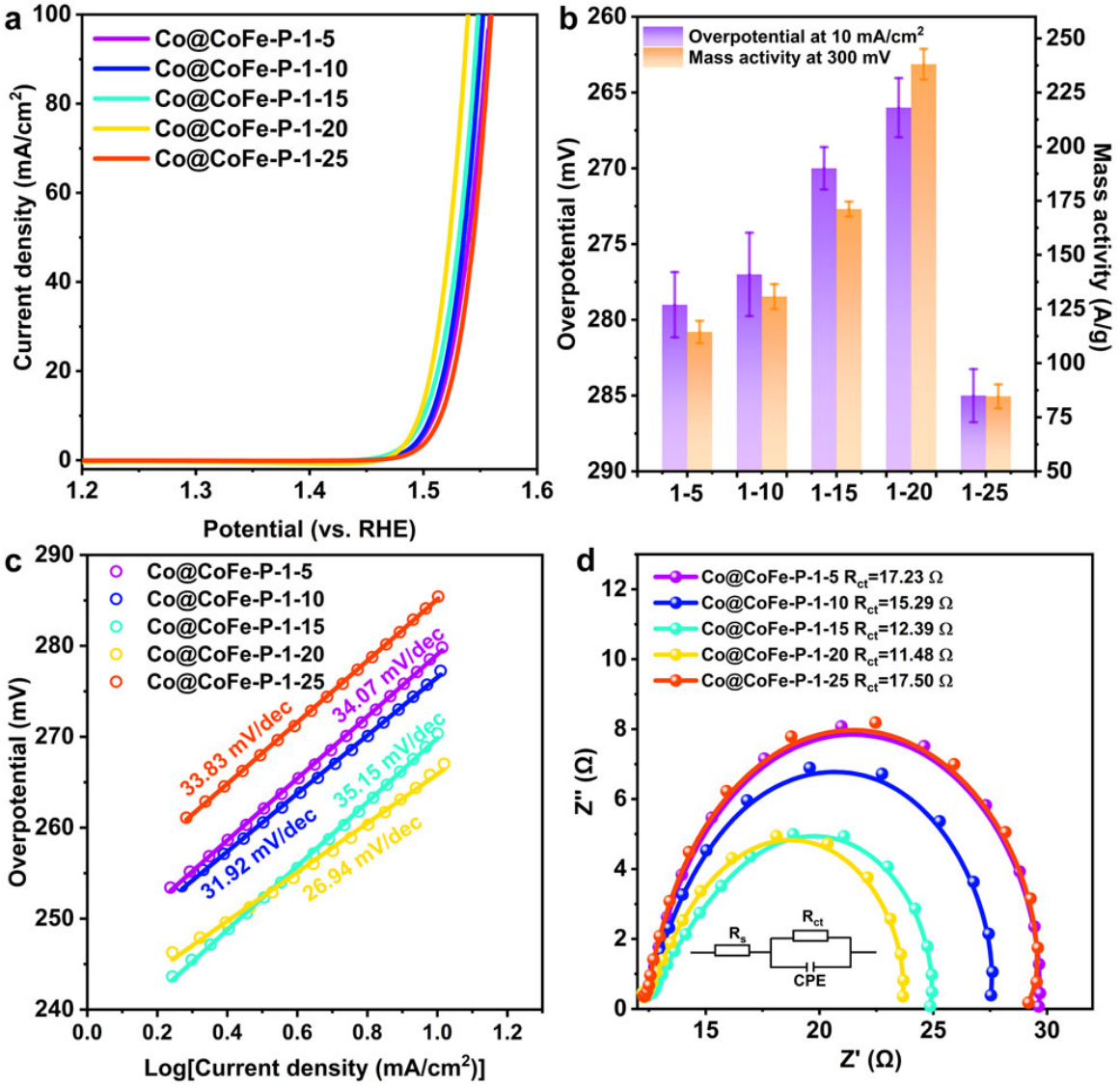

Figure S56. Electrocatalytic performance of Co@CoFe-P obtained with different amounts of NaH_2PO_2 in 1.0 M KOH for OER. (a) LSV curves. (b) Comparison of overpotential at 10 mA/cm^2 and mass activities (at an overpotential of 300 mV) of five catalysts. (c) Tafel plots. (d) Nyquist plots (at an overpotential of 300 mV).

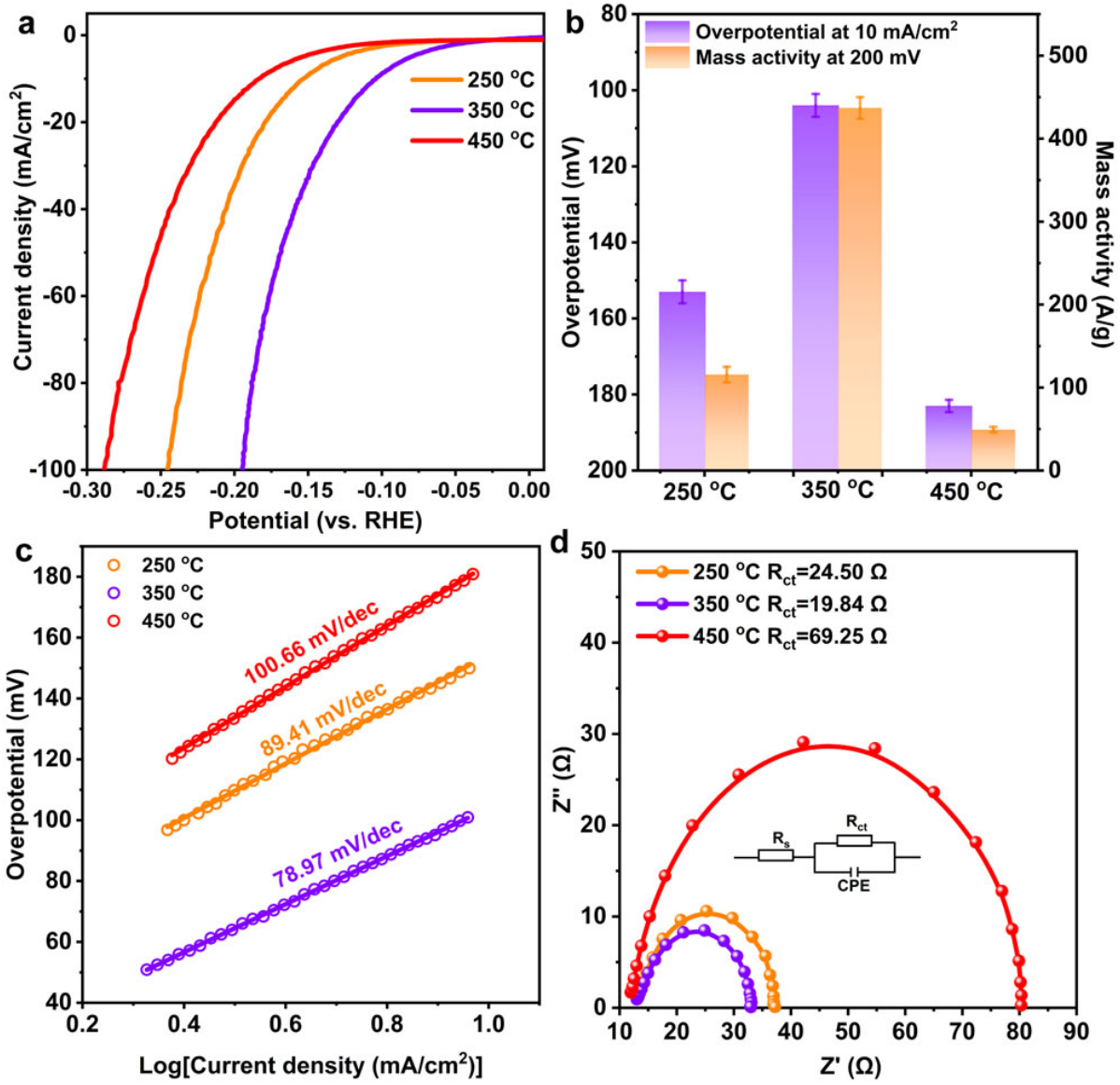

Figure S57. Electrocatalytic performance of Co@CoFe-P (1-20) at different phosphorization temperatures in 1.0 M KOH for HER. (a) LSV curves. (b) Comparison of overpotential at 10 mA/cm^2 and mass activities (at an overpotential of 200 mV) of three catalysts. (c) Tafel plots. (d) Nyquist plots (at an overpotential of 150 mV).

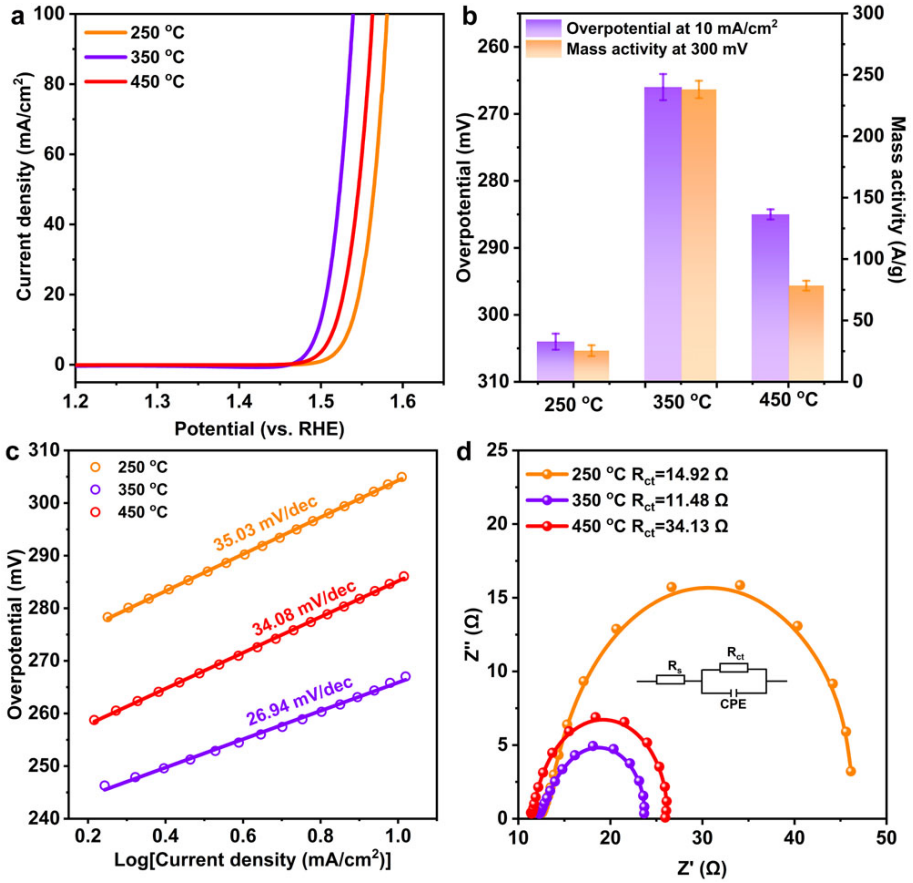

Figure S58. Electrocatalytic performance of Co@CoFe-P (1-20) at different phosphorization temperatures in 1.0 M KOH for OER. (a) LSV curves. (b) Comparison of overpotential at 10 mA/cm^2 and mass activities (at an overpotential of 300 mV) of three catalysts. (c) Tafel plots. (d) Nyquist plots (at an overpotential of 300 mV).

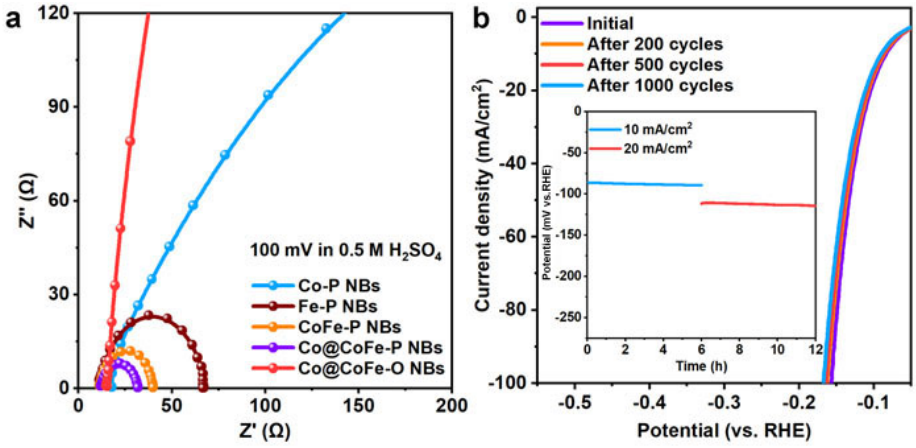

Figure S59. (a) Nyquist plots of as-prepared catalysts vs. references in 0.5 M H_2SO_4 for HER. (b) LSV curves of as-prepared Co@CoFe-P before and after 200, 500, and 1000 CV cycles for the stability test in 0.5 M H_2SO_4. The inset in (b) shows the corresponding chronopotentiometry tests of Co@CoFe-P NBs catalyst at current densities of 10 and 20 mA/cm^2.

As demonstrated by EIS characterizations (**Figure S59a**), the smallest semicircle corresponding to the lowest charge transfer resistance of 19.97 Ω is present for Co@CoFe-P NBs, which outperforms CoFe-P NBs (28.46 Ω), Fe-P NBs (56.75 Ω), Co-P NBs (603.56 Ω), and Co@CoFe-O NBs (7017.30 Ω). These results indicate enhanced electron transfer properties through employing hierarchical nanostructuring and phosphorization strategies. The

electrochemical stability, which is another important parameter for practical applications, has been further evaluated by both CV cycling and chronopotentiometry techniques. As shown in **Figure S59b**, the as-synthesized Co@CoFe-P NBs maintain the initial high HER activity after 1000 CV cycles and 12 h of chronopotentiometry tests.

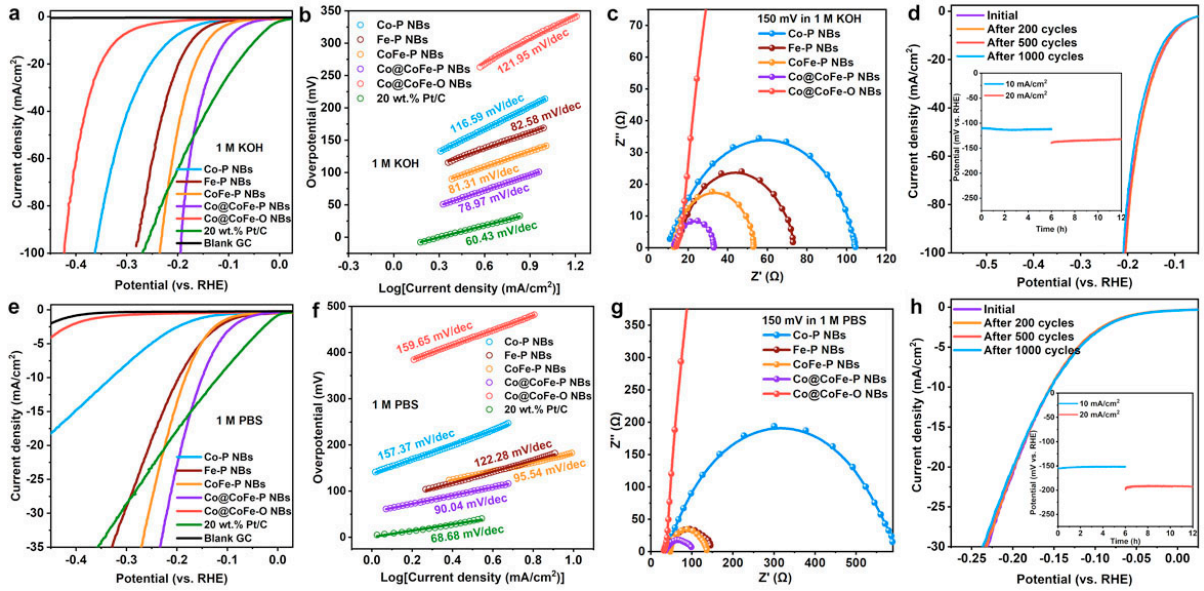

Figure S60. (a, e) LSV curves with a scan rate of 5 mV/s at room temperature of as-prepared Co-P NBs, Fe-P NBs, CoFe-P NBs, Co@CoFe-P NBs, and Co@CoFe-O NBs vs. commercial reference catalysts in 1.0 M KOH (pH 13.8) and 1.0 M phosphate buffer solution (PBS, pH 7.0) for HER, respectively. (b, f) Tafel plots of as-investigated catalysts in 1.0 M KOH and 1.0 M PBS for HER, respectively. (c, g) Nyquist plots of as-investigated catalysts in 1.0 M KOH and 1.0 M PBS for HER, respectively. (d, h) LSV curves of as-prepared Co@CoFe-P before and after 200, 500, and 1000 CV cycles for the stability test in 1.0 M KOH and 1.0 M PBS for HER, respectively. The insets in (d, h) show the corresponding chronopotentiometry tests of Co@CoFe-P NBs catalyst at current densities of 10 and 20 mA/cm^2.

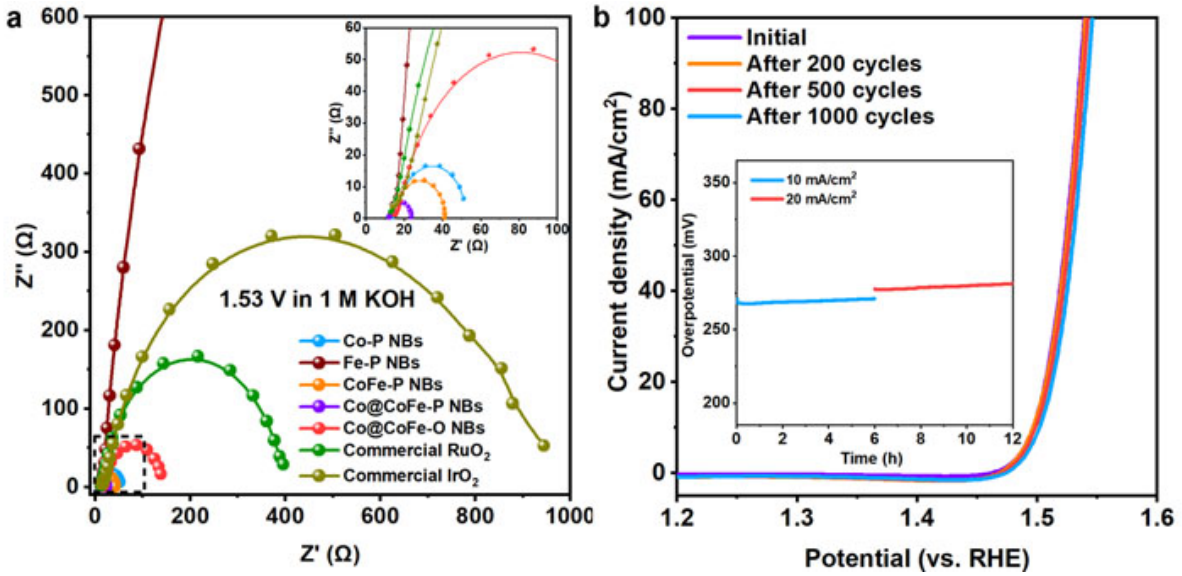

Figure S61. (a) Nyquist plots of as-prepared catalysts vs. references in 1 M KOH for OER. (b) LSV curves of as-prepared Co@CoFe-P before and after 200, 500, and 1000 CV cycles for the stability test in 1 M KOH for OER. The inset in (b) shows the corresponding chronopotentiometry tests of Co@CoFe-P NBs catalyst at current densities of 10 and 20 mA/cm^2.

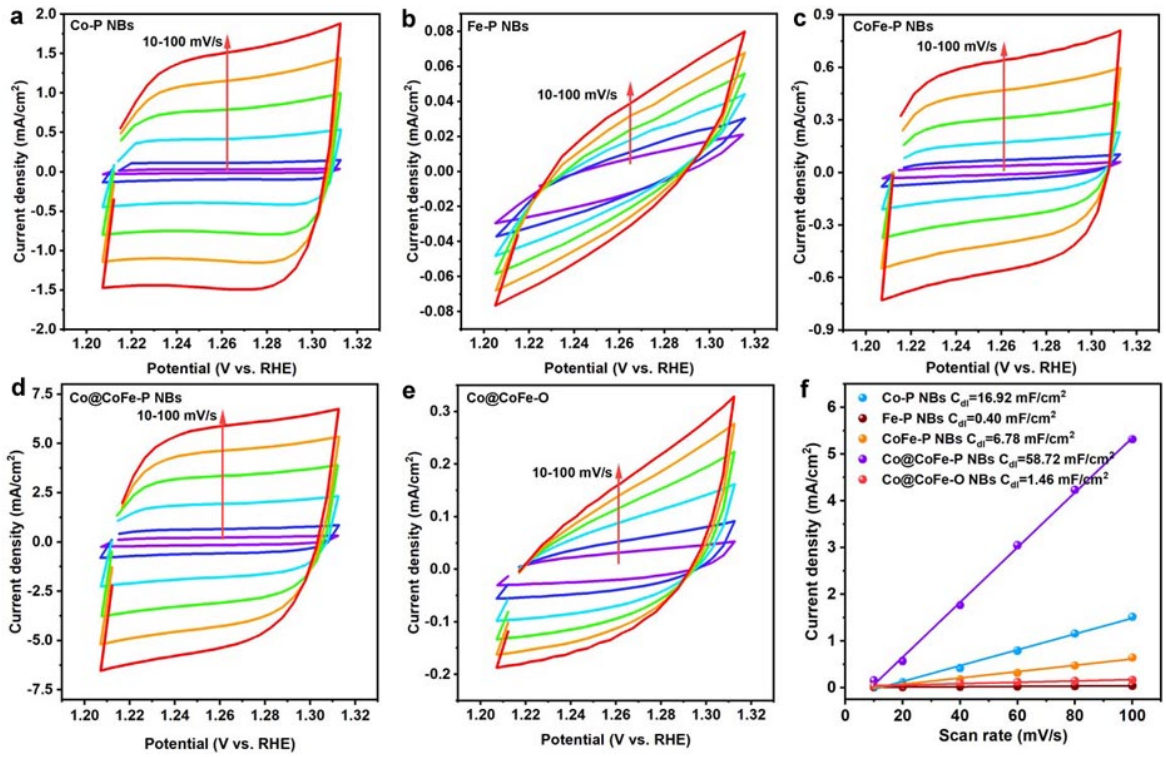

Figure S62. CV curves (a-e) and double-layer capacitance (C_{dl}) (f) of as-prepared catalysts in 1.0 M KOH.

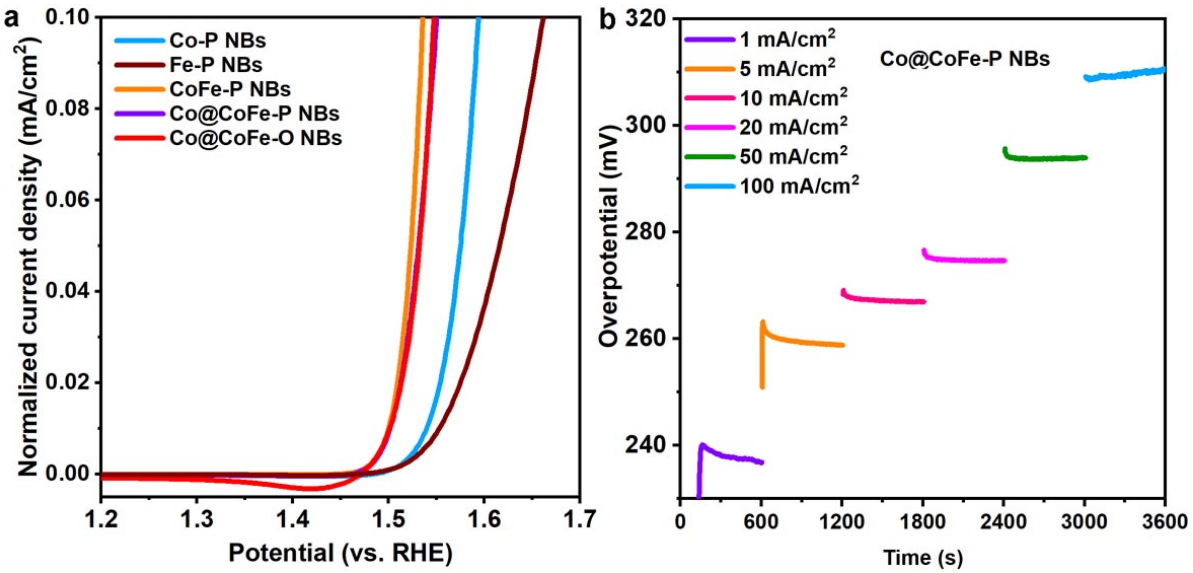

Figure S63. (a) LSV curves (current normalized by ECSA) of as-prepared catalysts. (b) Multi-current-step chronopotentiometric test of as-prepared Co@CoFe-P NBs electrode with current densities from 1 to 100 mA/cm^2 in 1.0 M KOH.

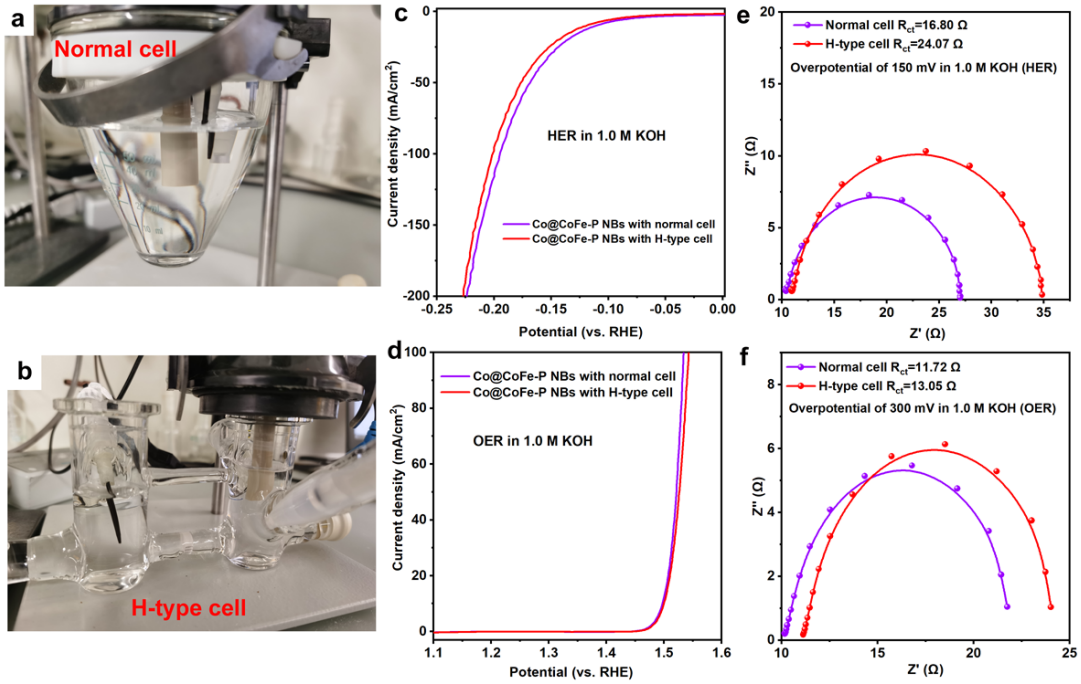

Figure S64. (a, b) Photos of electrochemical test setups with normal and H-type cells. (c, d) LSV curves of Co@CoFe-P NBs with two different cells for HER and OER in 1.0 M KOH. (e, f) Nyquist plots (at an overpotential of 300 mV).

We further employed a H-type cell to evaluate the HER and OER performance of Co@CoFe-P NBs in 1.0 M KOH. As shown in **Figure S64**, both the HER and OER activities evaluated with a H-type cell are quite similar to that of a normal cell. The activities with a H-type cell show a slight decline compared with those observed for a normal cell. This is a common phenomenon arising from the increased resistance.

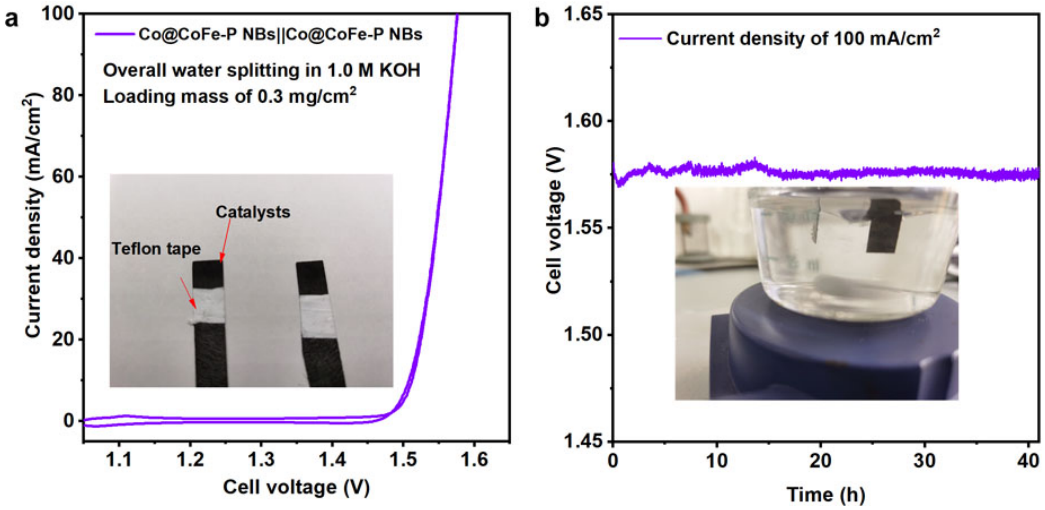

Figure S65. (a) Cyclic voltammetry (CV) curves of two-electrode system assembled with Co@CoFe-P NBs||Co@CoFe-P NBs in 1.0 M KOH (loading mass of 0.3 mg/cm^2). (b) Stability measurements of Co@CoFe-PNBs||Co@CoFe-P NBs loaded on carbon paper.

To investigate the electrochemical stability for overall water splitting, we conducted the CV and chronopotentiometric tests for the as-prepared catalysts with a low loading mass of 0.3 mA/cm^2. As shown in **Figure S65a**, the CV curve with a low loading mass shows a positive shift with a decreased baseline current density compared with that of a high loading mass

(**Figure 3e**). This is due to the decreased numbers of active sites and the weakening effects of double-layer capacitance in Co@CoFe-P NBs with a low loading mass. **Figure S65b** presents the stability measurement of Co@CoFe-P NBs||Co@CoFe-P NBs at a high current density of 100 mA/cm^2. From the data, the as-prepared Co@CoFe-P NBs can maintain the initial activity over 40 h without any obvious decline. This further confirms the superior catalytic performance of Co@CoFe-P NBs for overall water splitting.

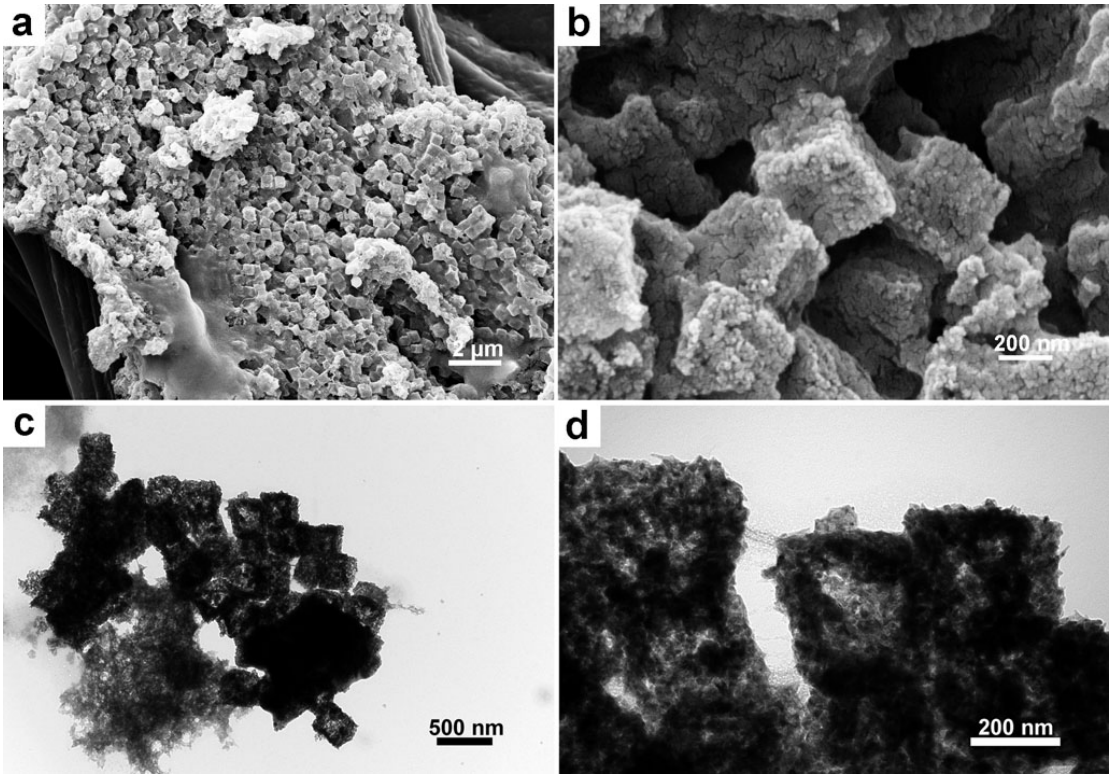

Figure S66. FESEM (a, b) and TEM (c, d) images of Co@CoFe-P after long time measurements for HER.

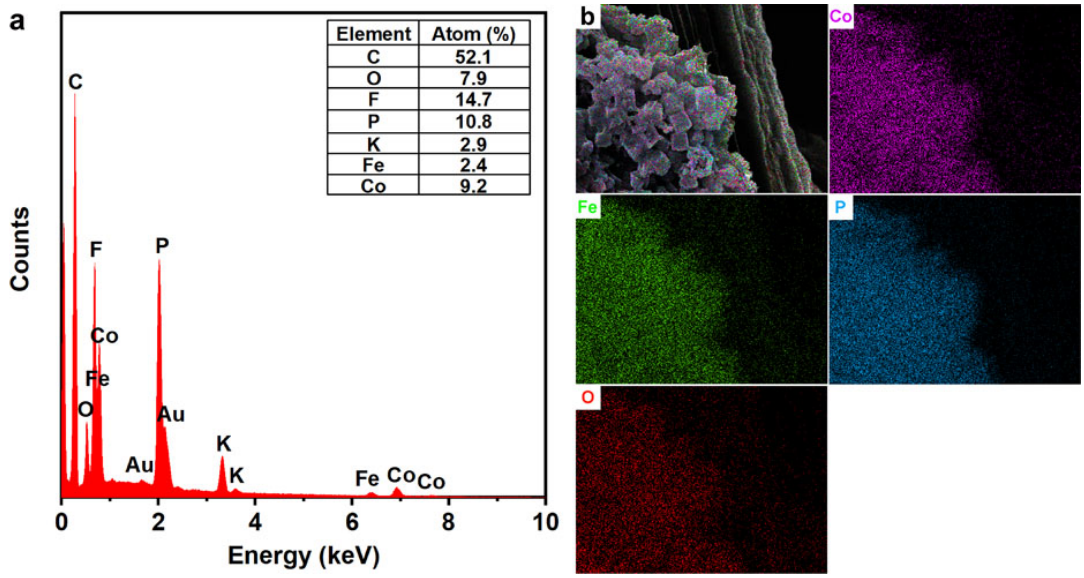

Figure S67. FESEM-EDX spectrum (a) and element mappings (b) of Co@CoFe-P after long time measurements for HER. (**Note: signals of F and K arise from Nafion and KOH, respectively.**)

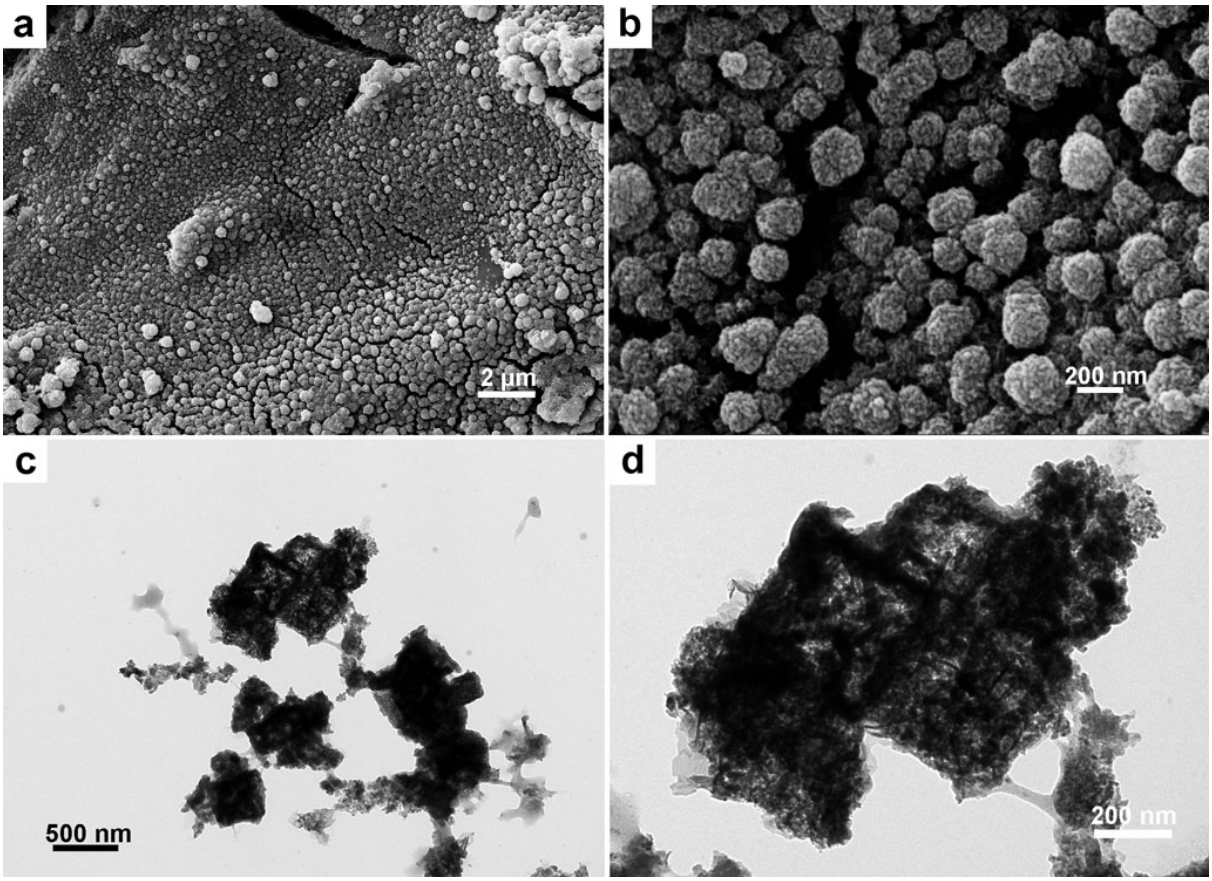

Figure S68. FESEM (a, b) and TEM (c,d) images of Co@CoFe-P after long time measurements for OER.

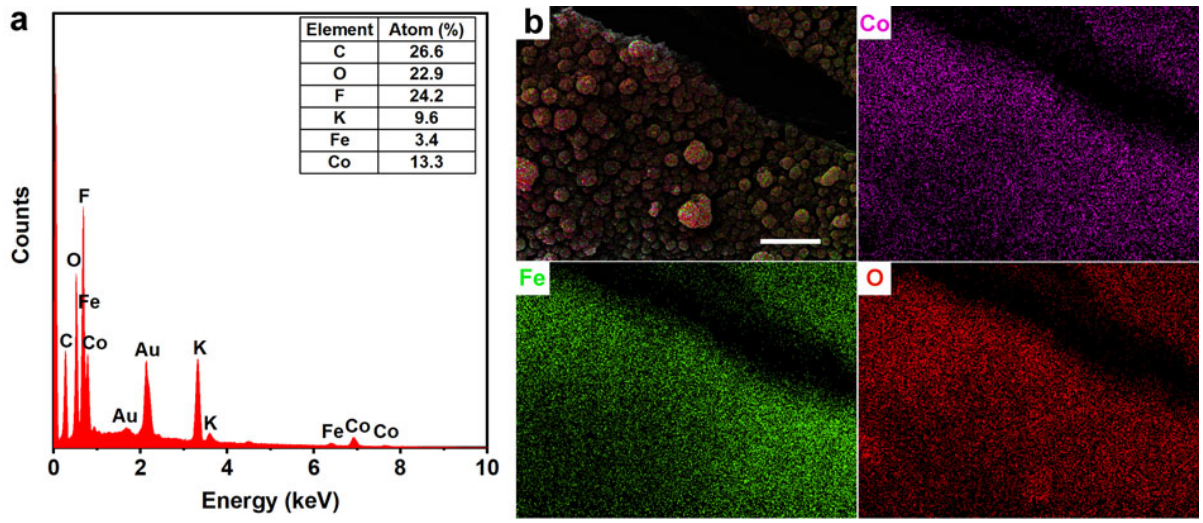

Figure S69. FESEM-EDX spectrum (a) and element mappings (b) of Co@CoFe-P after long time measurements for OER. (**Note: signals from F and K arise from Nafion and KOH, respectively.**)

Post-catalytic SEM and TEM characterization (**Figures S66 and S68**) reveal that Co@CoFe-P NBs retained their pristine nanobox morphology both after the HER and OER processes. These results suggest the robust morphological stability of the as-prepared Co@CoFe-P NBs, which renders it a very promising candidate for low-cost and noble metal-free overall water splitting.

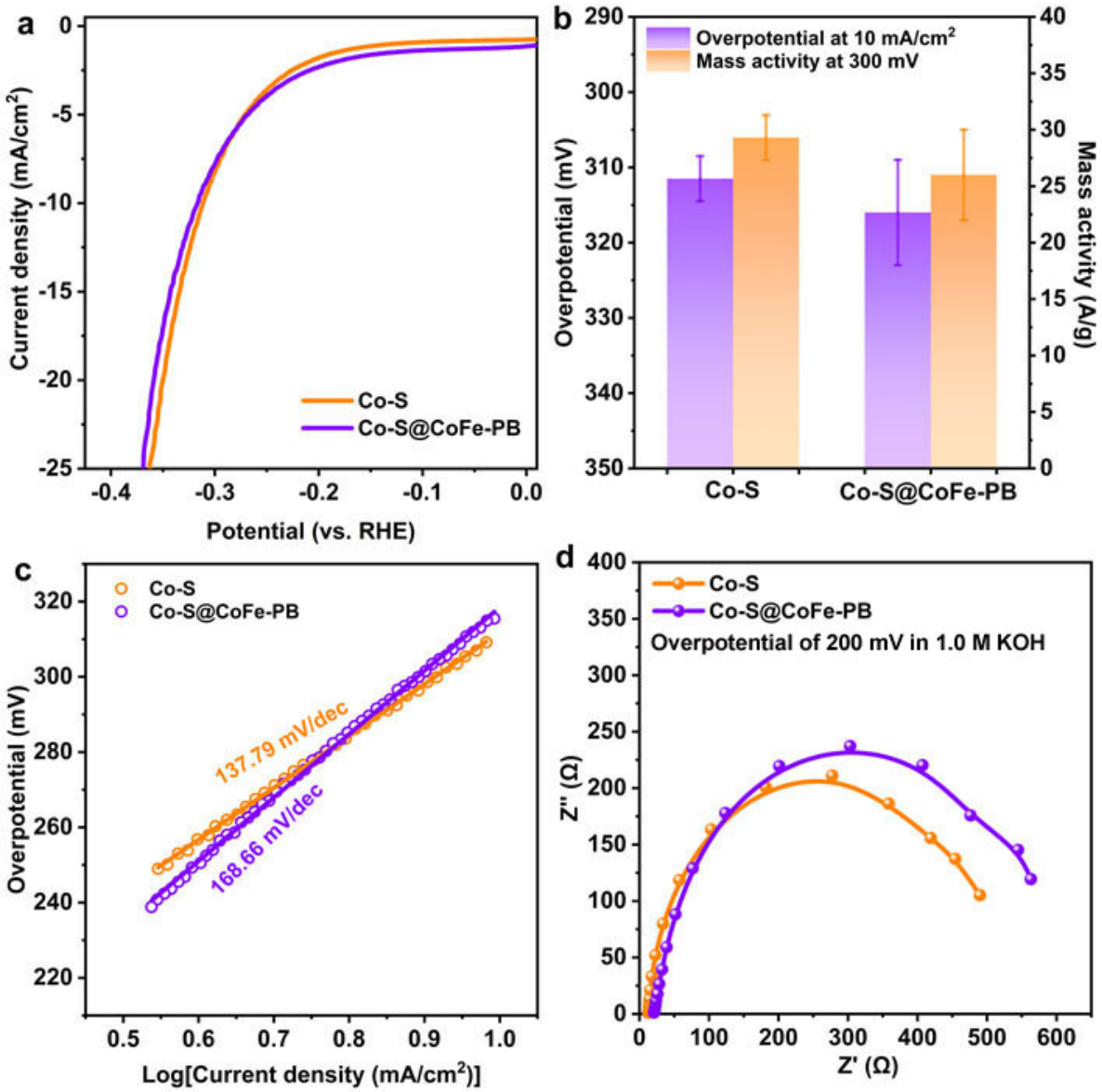

Figure S70. Electrocatalytic performance of Co-S and Co-S@CoFe-PB in 1.0 M KOH for HER. (a) LSV curves. (b) Comparison of overpotentials at 10 mA/cm^2 and mass activities (at an overpotential of 300 mV) of two catalysts. (c) Tafel plots. (d) Nyquist plots (at an overpotential of 200 mV).

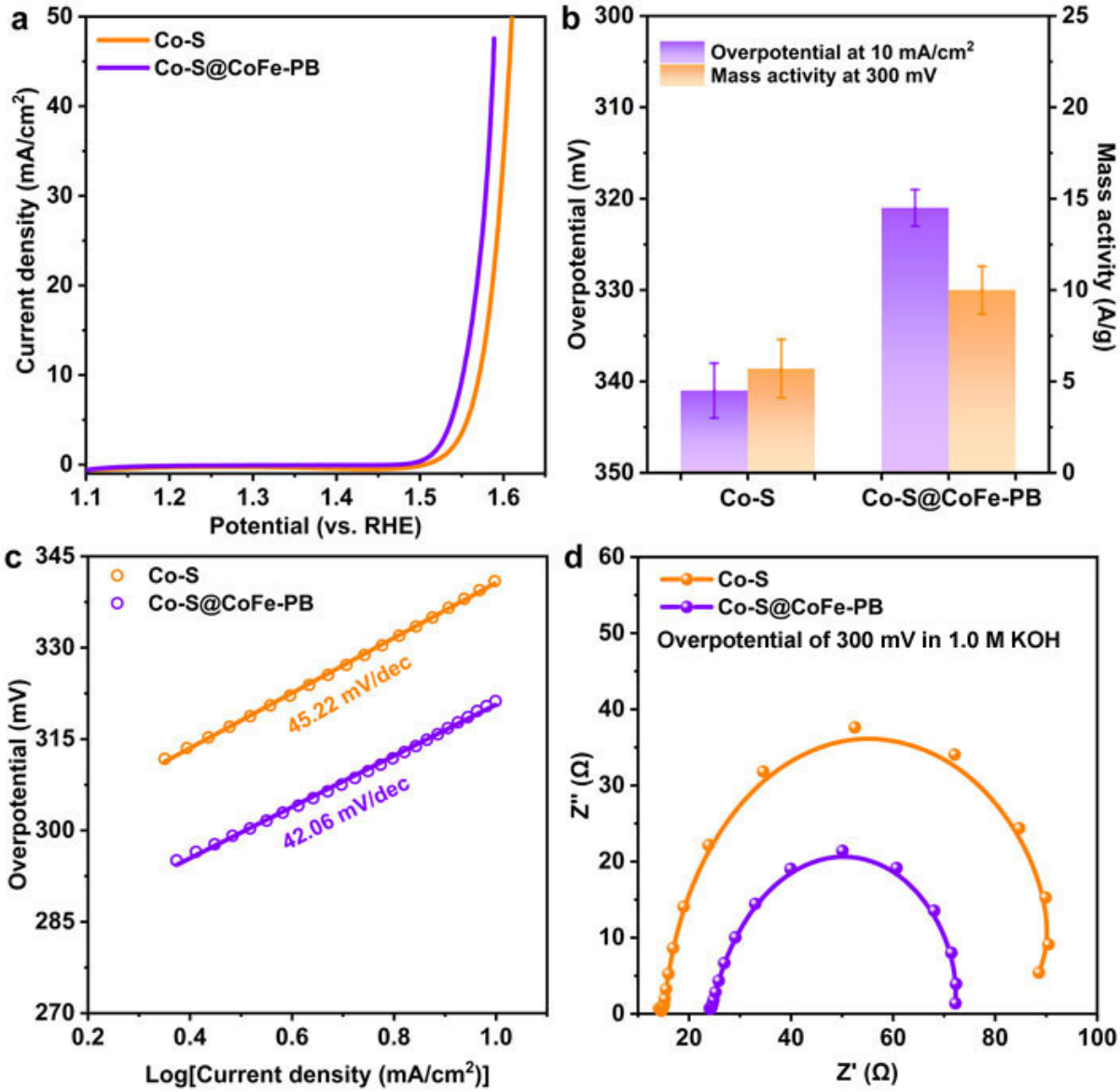

Figure S71. Electrocatalytic performance of Co-S and Co-S@CoFe-PB in 1.0 M KOH for OER. (a) LSV curves. (b) Comparison of overpotentials at 10 mA/cm^2 and mass activities (at an overpotential of 300 mV) of two catalysts. (c) Tafel plots. (d) Nyquist plots (at an overpotential of 300 mV).

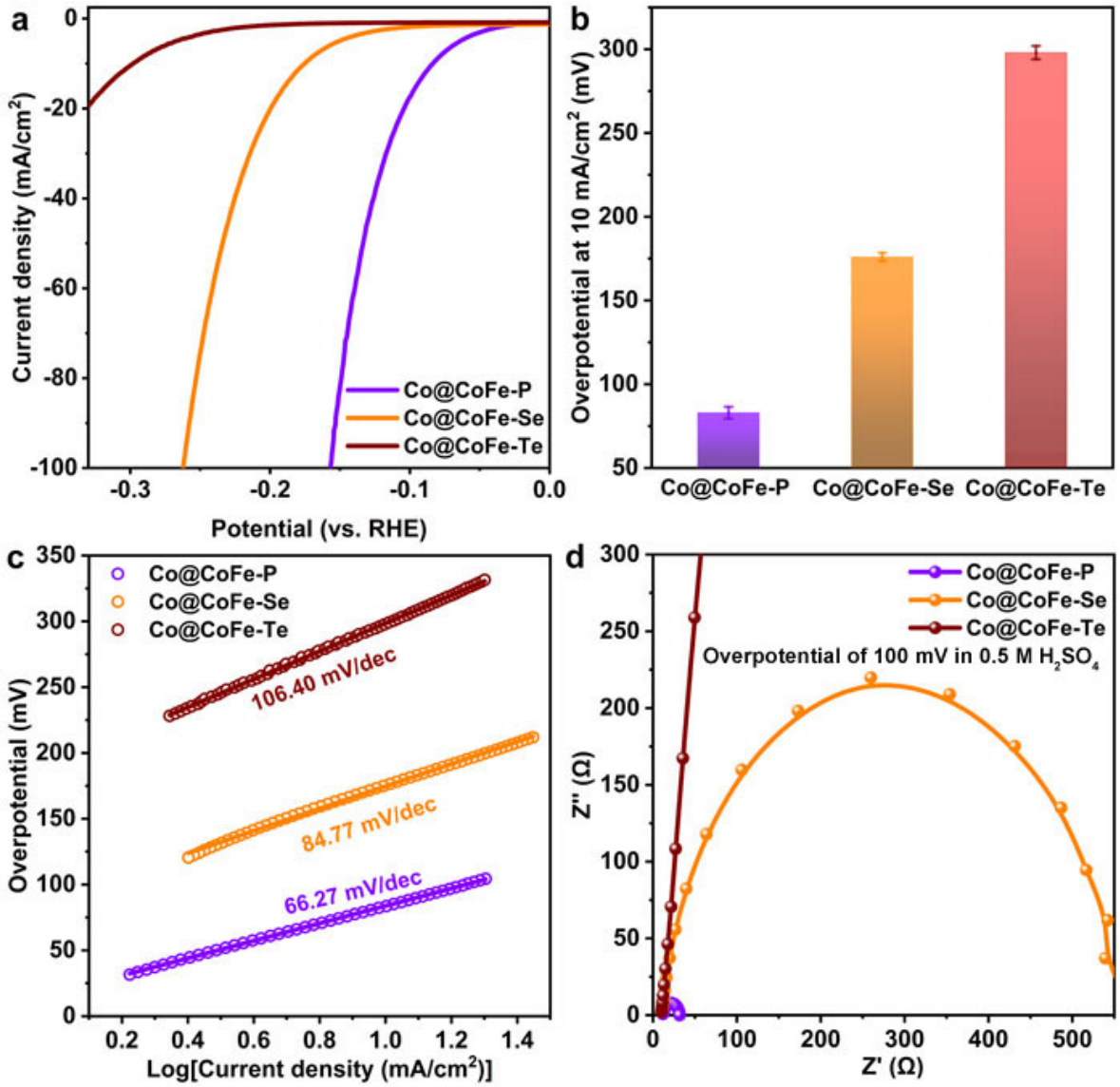

Figure S72. Electrocatalytic performance of Co@CoFe-M (M=P, Se, and Te) in 0.5 M H_2SO_4 for HER. (a) LSV curves. (b) Comparison of overpotentials at 10 mA/cm^2 of three catalysts. (c) Tafel plots. (d) Nyquist plots (at an overpotential of 100 mV).

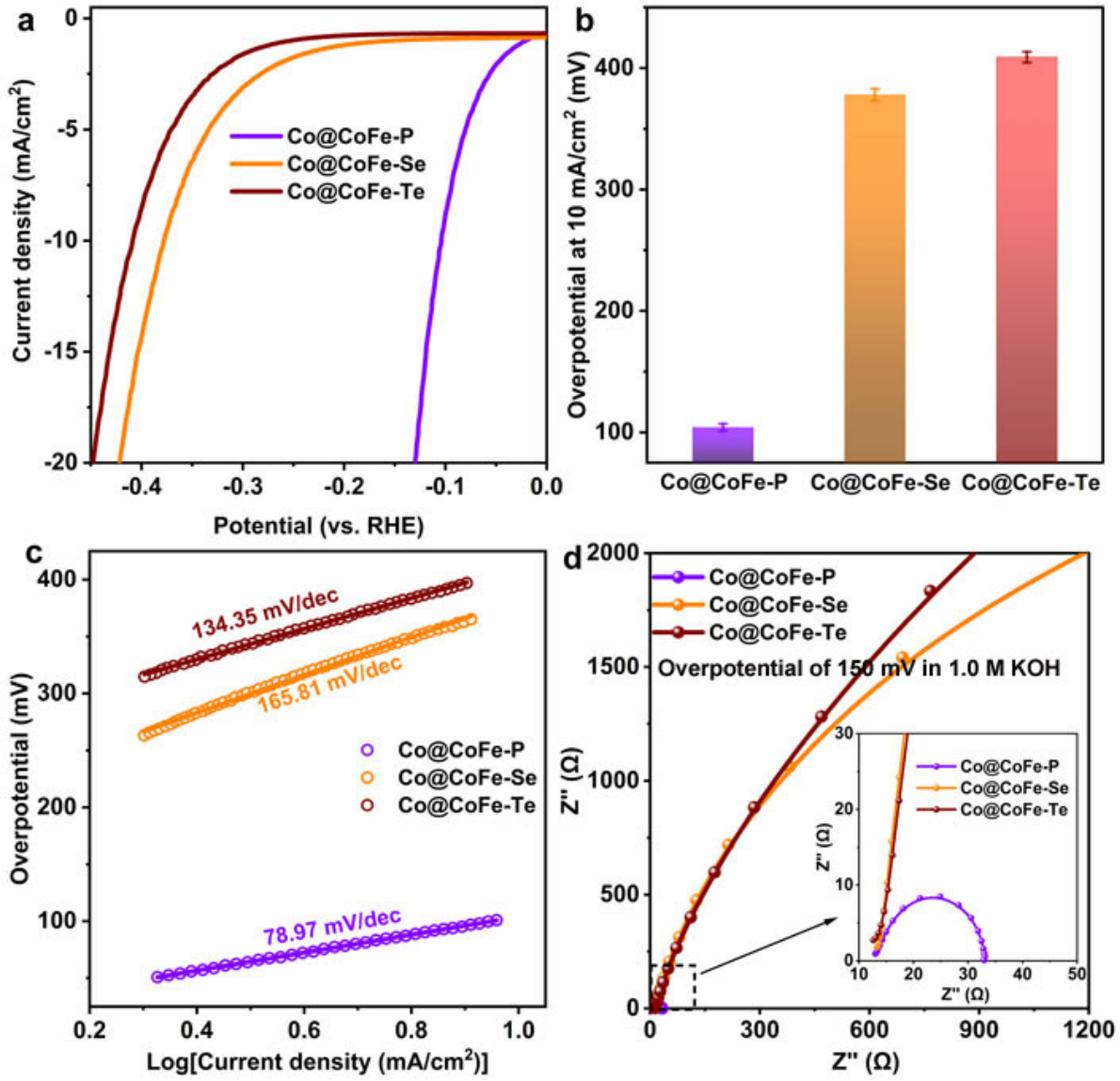

Figure S73. Electrocatalytic performances of Co@CoFe-M (M=P, Se, and Te) in 1.0 M KOH for HER. (a) LSV curves. (b) Comparison of overpotentials at 10 mA/cm^2 of three catalysts. (c) Tafel plots. (d) Nyquist plots (at an overpotential of 150 mV).

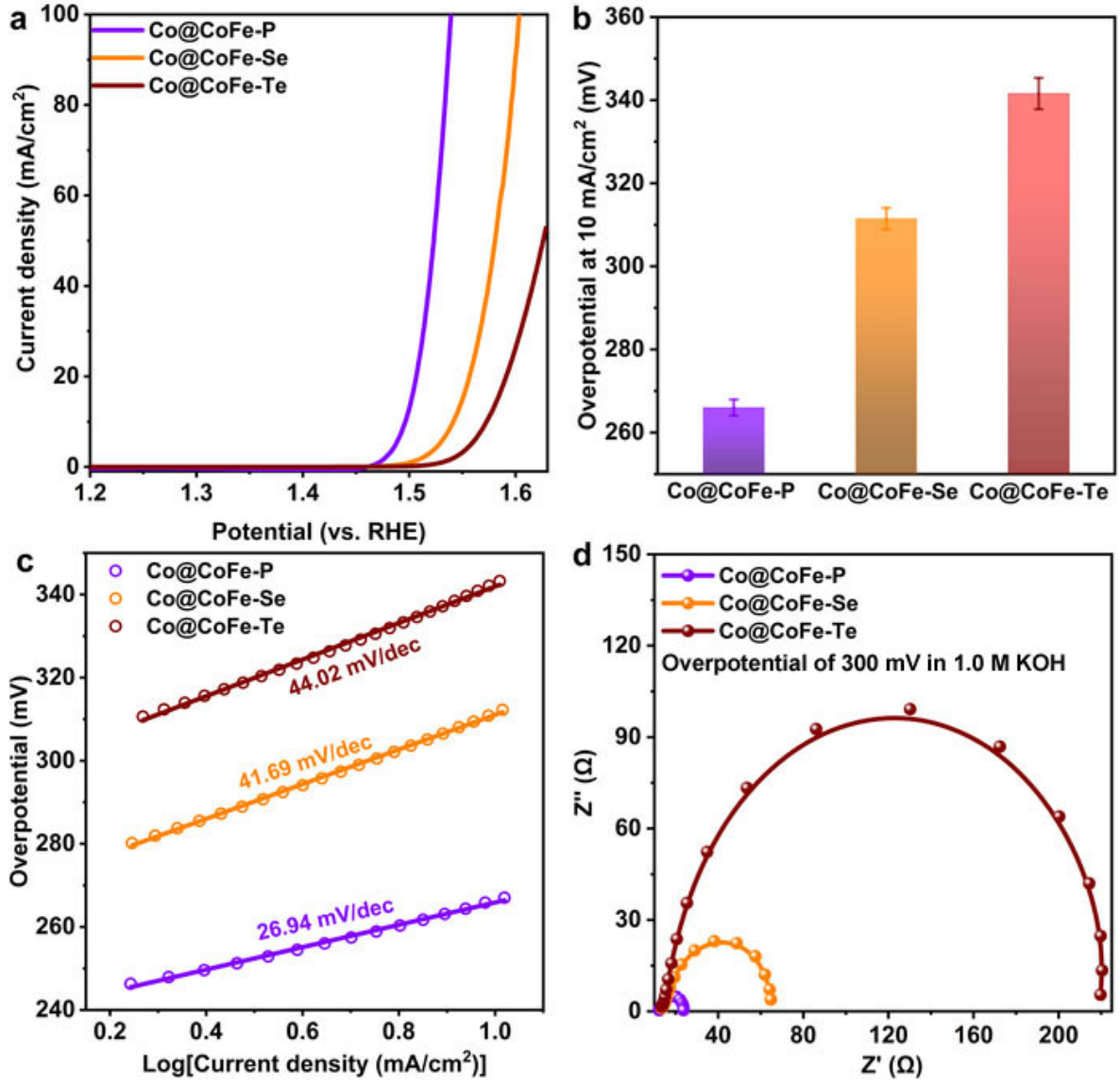

Figure S74. Electrocatalytic performances of Co@CoFe-M (M=P, Se, and Te) in 1.0 M KOH for OER. (a) LSV curves. (b) Comparison of overpotentials at 10 mA/cm^2 of three catalysts. (c) Tafel plots. (d) Nyquist plots (at an overpotential of 300 mV).

5.2 Sodium-ion battery performance of Co-S@CoFe-PB

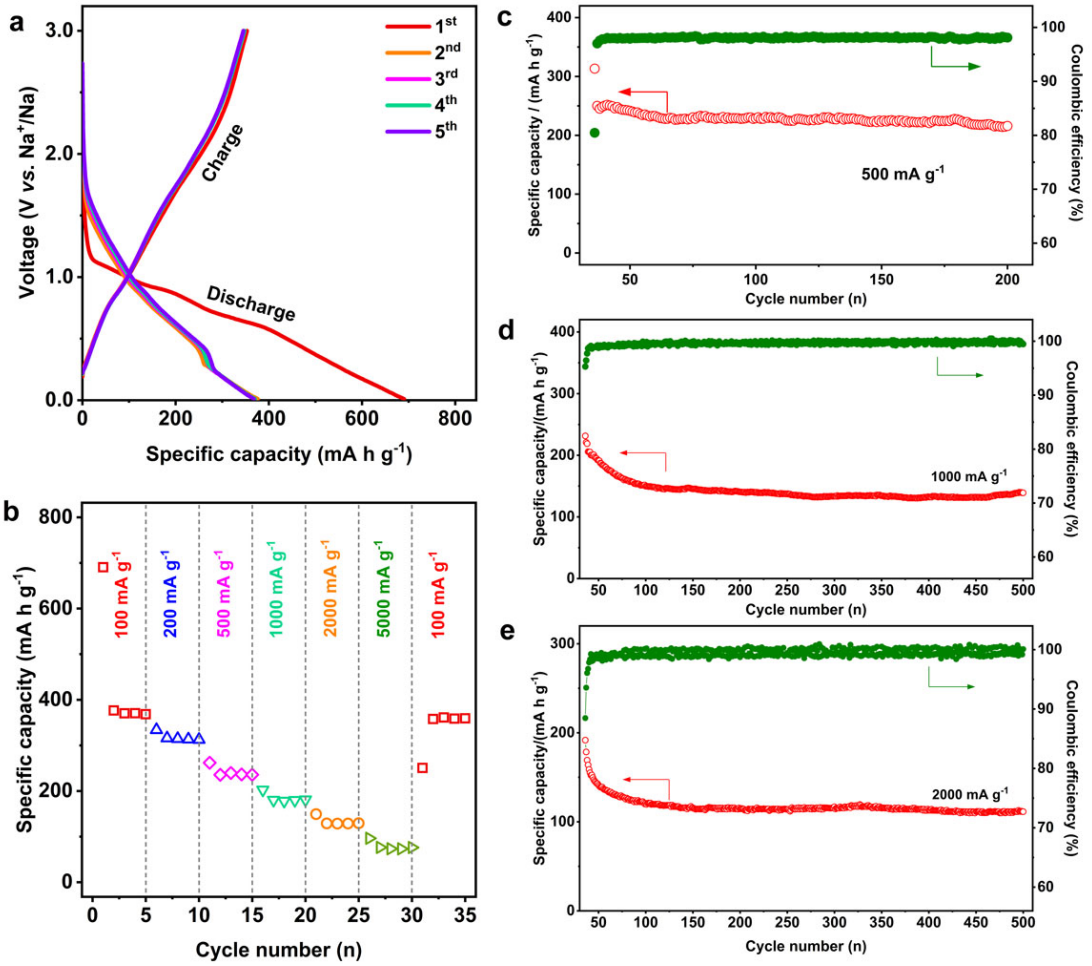

Figure S75. Electrochemical performance of Co-S@CoFe-PB electrodes for sodium-ion batteries. (a) Charge/discharge curves at the current density of 100 mA g^{-1}. (b) Rate performance for a current density range of 100 to 5000 mA g^{-1}. (c-e) Long-term cycling stability at current densities of 500 mA g^{-1}, 1000 mA g^{-1}, and 5000 mA g^{-1}.

Our previous work systematically investigated the employment of CoFe-PB NCs for water splitting and highlighted the underlying leaching issues of $Fe(CN)_6^{3-}$ under alkaline conditions.[5] We revealed that after immersion of as-prepared CoFe-PB into the electrolyte, $Fe(CN)_6^{3-}$ moieties were immediately leaching from the structure into the electrolyte. Therefore, the as-prepared CoFe-PB was transformed into $Co(OH)_2$ under alkaline conditions. In line with our previous study,[5] when assembling the as-prepared Co-S@CoFe-PB NBs as electrocatalysts towards water splitting under alkaline conditions, the initial real catalytic species were assigned to the reconstructed Co-S@$Co(OH)_2$ species. Since $Co(OH)_2$ is not a very good HER catalyst, thereby, the as-prepared Co-S@CoFe-PB NBs exhibit very similar electrocatalytic performance compared with that of Co-S NBs (**Figures S70-S71**). To extend the practical application of the as-prepared hierarchically nanostructured Co-S@CoFe-PB NBs, we further tested their performance in sodium-ion batteries. Recent works indicate that the use of hollow configurations can compensate for the drawbacks caused by volume changes during the sodium ions insertion/extraction process. Moreover, the well-developed hierarchical shells can facilitate the transportation of sodium ions and retain long-time cycling stability.[97-99] As shown in **Figure S75**, the as-prepared Co-S@CoFe-PB NBs can deliver a high charge capacity

of 380 mAh g^{-1} and exhibit good cycling stability over 500 cycles at 2 Ah g^{-1}, which is competitive with most recent studies.[100-101] It is also noteworthy that the sodium-ion battery performance of as-prepared Co-S@CoFe-PB NBs can be further optimized by adjusting the experimental synthesis parameters, e.g., hydrothermal reaction temperatures and reaction times. In the current study, we only examined the potential application of as-investigated materials in sodium-ion batteries. Our future work will be focused on the adjustment of experimental parameters to optimize the sodium-ion battery performance of Co-S@CoFe-PB NBs.

6. Post-catalytic characterization

6.1 XPS characterization of Co@CoFe-P after HER and OER

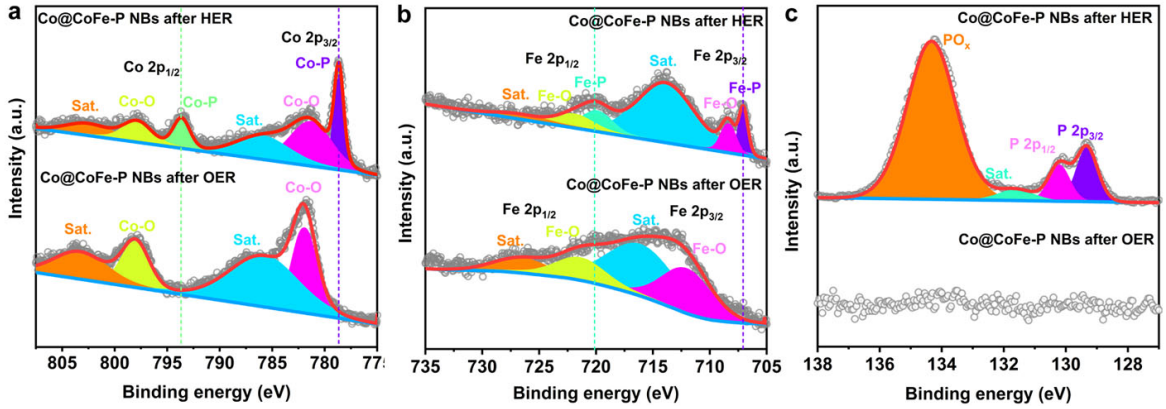

Figure S76. (a-c) High-resolution Co 2p, Fe2p, and P 2p XP spectra of Co@CoFe-P samples after HER and OER tests.

6.2 CV curves of the investigated catalysts

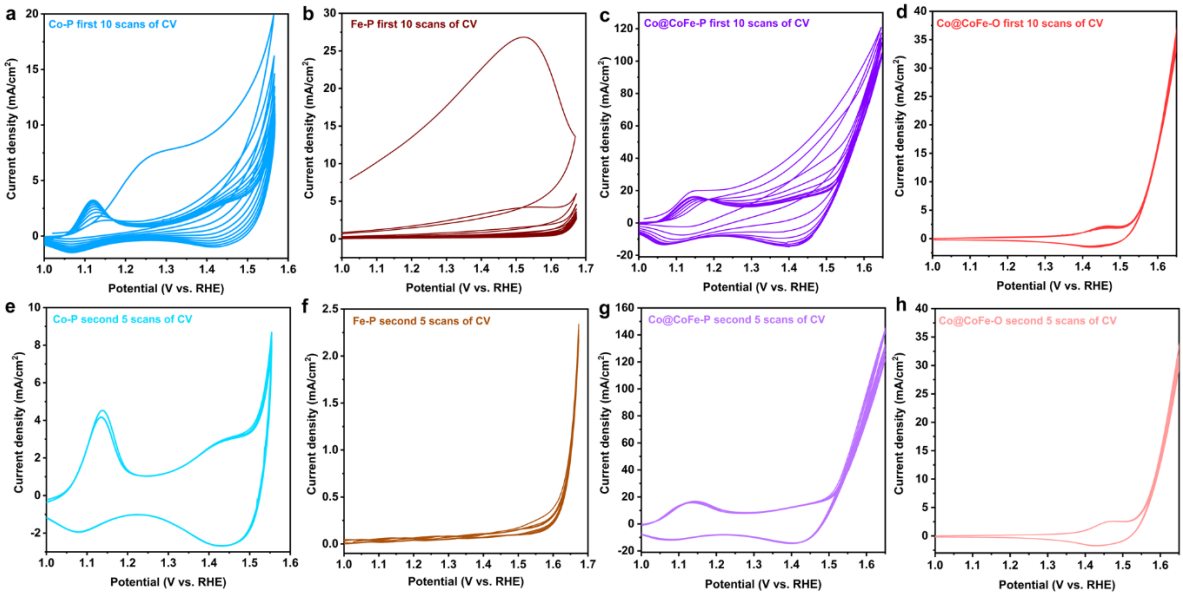

Figure S77. (a-d) 10 CV curves with fresh electrodes of Co-P, Fe-P, Co@CoFe-P, and Co@CoFe-O NBs towards OER. (e-h) 5 CV curves of the same electrodes used in Figures (a-d) after EIS and ECSA measurements. (**Note: No rotation was applied here.**)

Supplementary Discussion II: Post-catalytic characterization

We first conducted *ex situ* XPS and CV tests to investigate the intrinsic structure-activity relationships during the water splitting half-reactions. The XPS results (**Figure S76**) evidence that the ratio of peak area between M-O bonds (M: metals) and PO_x groups decreased to 0.27 in Co@CoFe-P NBs after HER compared with that of pristine samples (0.54) (**Figures S53 and S76**). Regarding Co@CoFe-P NBs after OER, the post-catalytic XPS studies (**Figure S76**) reveal that all the peaks assigned to M-P bonds are gone, while the peaks arising from M-O bonds remain, exhibiting a similar surface electronic structure to metal oxides/(oxy)hydroxides.[13, 31] **Figures S77** presents the CV properties of Co-P NBs, Fe-P NBs, Co@CoFe-P NBs, and Co@CoFe-O NBs for OER in 1.0 M KOH with a scan rate of 50 mV/s without any applied rotation. All the phosphide samples undergo irreversible changes in their voltammograms in the initial 5 CV scans, followed by the reproducible voltammograms in the subsequent scans (**Figures S77a-c**). After the same electrodes were tested for EIS and ECSA measurements, 5 new CV scans were performed. As expected, all the phosphide electrodes displayed reversible voltammograms during the secondary CV tests (**Figure S77e-g**). However, such irreversible and subsequently reproducible voltammograms, respectively, were not observed for the Co@CoFe-O NB electrodes (**Figure S77d,h**). These results altogether suggest potentially irreversibly structural reconstructions in phosphide-based catalysts during the anodic polarization process. To the best of our knowledge, the appearances of two prominent redox peaks close to 1.13 V and 1.42 V for Co-P NBs (**Figure S77e**) arise from the redox reaction of $Co(OH)_2$/CoOOH and CoOOH/CoO_2, respectively.[102-103] This demonstrates that the investigated Co-based phosphide electrodes undergo structural reconstructions into $Co(OH)_2$/CoOOH/CoO_2 during the OER process. Structural changes as indicated by CV results were often underrated in most previous studies and rather referred to as catalytic activation for the anodic catalysts.[53-55] Based on these findings, we conclude that the as-prepared phosphide materials undergo structural reconstruction during HER and OER processes, which calls for the determination of the real active species involved in both reactions.

7. *Operando* XAS characterization

7.1 Detailed setup for *operando* XAS tests

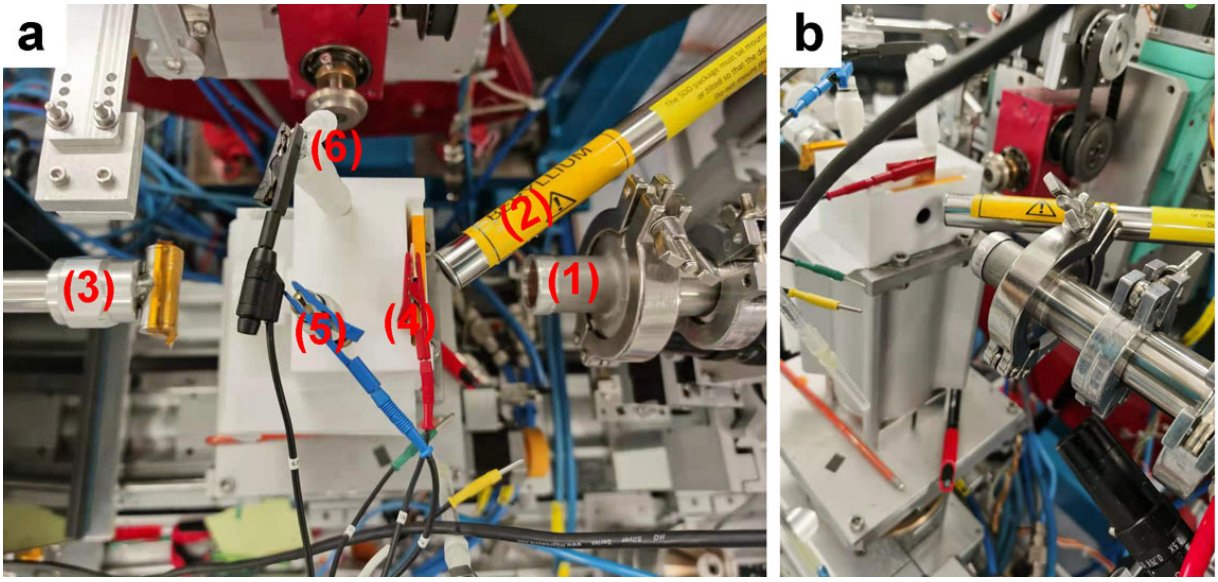

Figure S78. (a, b) Top-view and side-view of the in-housed developed *operando* electrochemical cell and the detailed setup for the *operando* XAS test (pictures taken at ESRF, SNBL, BM31). (1) X-ray beam; (2) Vortex® fluorescence (silicon drift) detector; (3) flight tube for transmission signals; (4) working electrode with carbon paper; (5) reference electrode with Hg/HgO (1.0 M KOH); (6) counter electrode with graphite rod.

7.2 *Operando* XAS investigations of Co-P towards HER

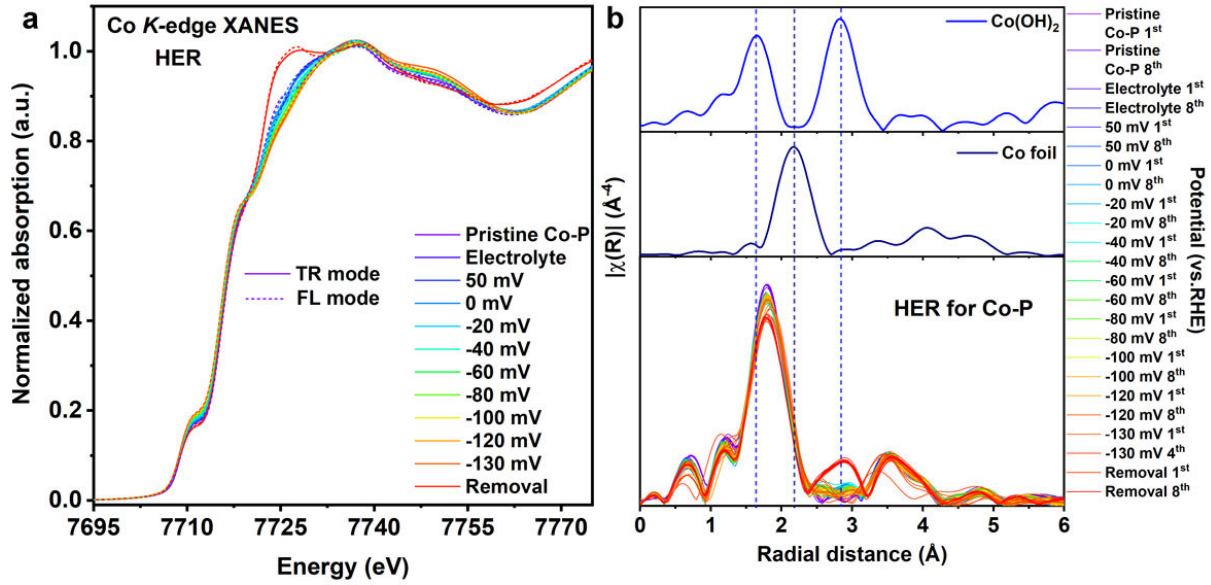

Figure S79. (a) Merged *operando* Co *K*-edge XANES spectra of Co-P recorded at potentials from 50 mV to -130 mV (vs. RHE) in 1.0 M KOH towards HER via both TR and FL modes. (b) *Operando* Co *K*-edge FT-EXAFS spectra (recorded 8 times) of Co-P towards HER vs reference Co foil and $Co(OH)_2$.

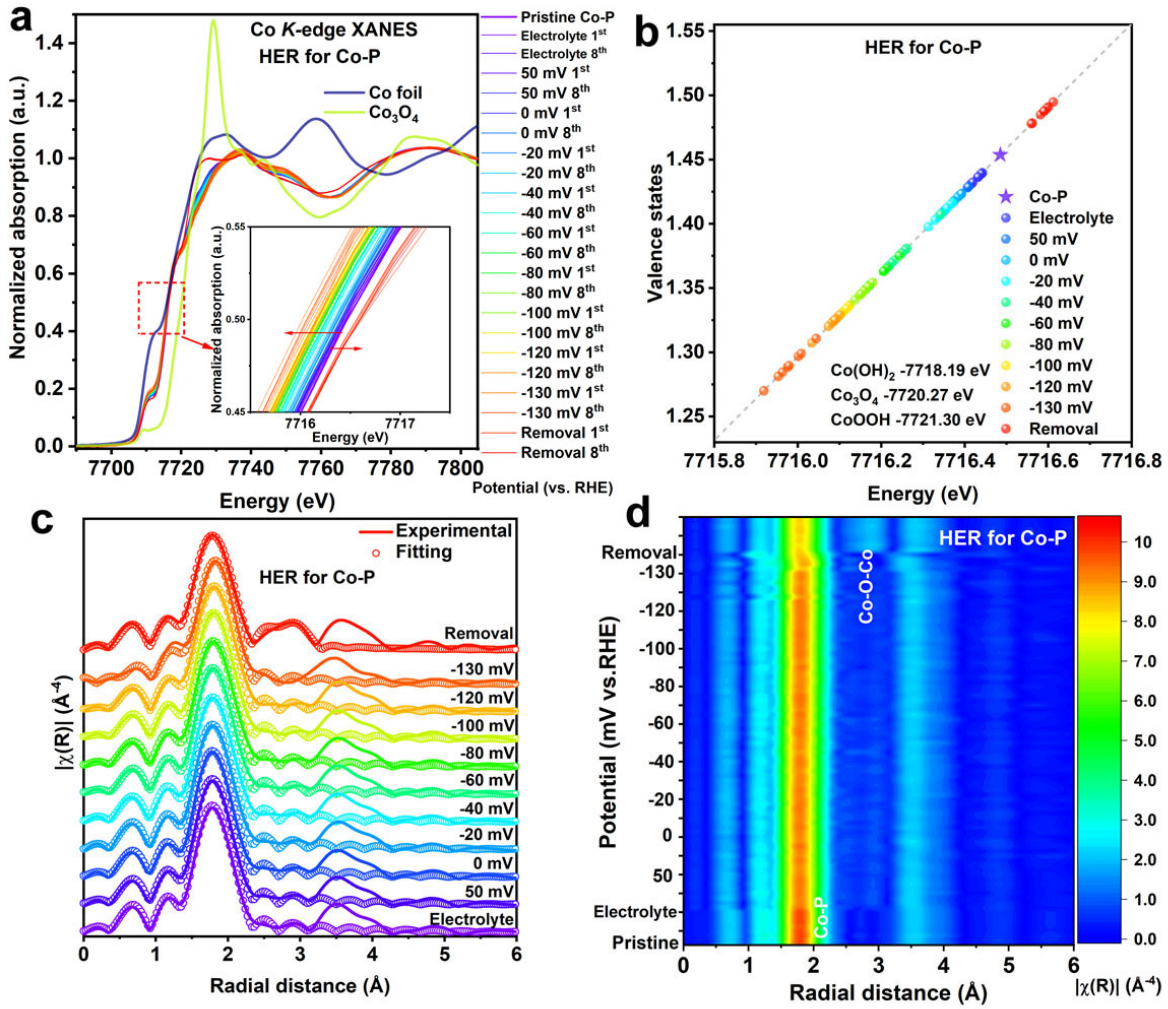

Figure S80. (a) *Operando* Co *K*-edge XANES spectra of Co-P recorded at different potentials in 1.0 M KOH for HER. (b) Calculated Co valence states of Co-P recorded at different potentials in 1.0 M KOH for HER. (c) Fitting of *operando* Co *K*-edge FT-EXAFS spectra (merged) of Co-P recorded at different potentials in 1.0 M KOH for HER. (d) 2D contour plots of *operando* Co *K*-edge FT-EXAFS spectra of Co-P recorded at different potentials in 1.0 M KOH for HER. (When the potential is higher than the onset potential for HER, the formation of gas bubbles drastically influences the quality of EXAFS data recorded in transmission mode. Therefore, we only present the XANES data without showing the EXAFS data when there were lots of bubbles formed.)

Supplementary Discussion III: Dynamics of active species in Co-P during the HER process

To clearly monitor the changes in the local electronic structures during the reaction process, the different *operando* XAS data recorded at the same potential except for the fitting of FT-EXAFS spectra were not merged (**Figures S79 and S80**). Moreover, *operando* XAS measurements recorded in fluorescence (FL) mode were also carried out to further investigate the evolution of the local electronic structure during the catalytic process. As shown in **Figure S79a**, the *operando* XANES spectra recorded in both TR and FL modes (merged data) exhibit a similar line shape, confirming the reproducibility of the variations in the local electronic structure of Co centers during the measurements. **Figure S80a** shows *operando* XAS results of as-prepared Co-P NBs in 1.0 M KOH for HER. As shown in the *operando* XANES spectra (**Figures S79a and S80a)**, the rising absorption edge of the sample immersed into the electrolyte exhibits a slightly negative energy shift, along with a broader and stronger peak intensity at approximately 7725 eV with respect to the pristine sample. Based on recent *operando* XAS works,[33,87] the negative energy shift is mainly ascribed to the chemisorption of H_2O/OH^- species from the electrolyte. After applying the cathodic potential (**Figure S80a**), the rising absorption edge shifts towards lower energy, with the lowest energy position observed at negative 130 mV vs. RHE. These changes are consistent with the observations for the valence states of Co in Co-P NBs, where the average valence state of Co ions reaches the lowest value of +1.28 (+1.45 for pristine) at negative 130 mV vs. RHE (**Figure S80b**).

The evolutions of the local coordination environments of Co centers in Co-P NBs were further investigated by fitting the *operando* FT-EXAFS spectra using the Co-O and Co-P scattering paths (**Figures S79b and S80c,d**). From the results in **Figure S80c** and **Table S7**, it is observed that under cathodic polarization, the CN_{Co-O} in Co-P NBs decreases obviously and the average Co-O bond distance increases slightly. However, the structural variations of Co-P bonds can be neglected. This is also seen in the 2D contour plots of the *operando* FT-EXAFS spectra (**Figure S80d**), where the intensity maximum at ~1.78 Å (backscattering of Co-O and Co-P paths) shows a slight decrease during the cathodic polarization process. Interestingly, after removing the applied potential, the CN_{Co-O} further increased to 0.58, and the average valence state of Co increased to +1.49, i.e. slightly higher than that of pristine Co-P NBs (0.55 for CN_{Co-O} and +1.45 for Co) (**Figure S80b and Table S7**). From the analyses of the atomic coordination environments of Co centers, it is concluded that the *in situ* reconstructed P-Co-O configuration undergoes structural relaxations during the cathodic polarization process, which evidences that it acts as the real HER active site in Co-P NBs. As shown in **Figures S79b** and **S80d**, a low intensity at a radial distance of 2.88 Å in the FT-EXAFS spectra and the 2D contour plot is observed after removing the applied cathodic potential. The observed weaker second shell scattering can be ascribed to the backscattering from the Co-Co path with edge-sharing Co^{II}-O-Co^{II} bonds (**Figures S79b, S80d and Table S7)**. In the current study, during the cathodic polarization process, our *operando* XAS results reveal that the Co ions in the P-Co-O moieties reach a low oxidation state (smaller than +2, e.g., Co^0/Co^+)[104] to trigger the HER process. After the applied potential is removed, the reoxidation of Co induced the incorporation of O atoms and partial P leaching (**Table S1**), which further results in a structural distortion of the edge/face-sharing Co octahedra in Co-P NBs. Thereby, the structural properties of the Co octahedral moieties (Co-$P_{6-x}O_x$) are altered and more intense backscattering would be expected from the Co-Co path with edge-sharing Co^{II}-O-Co^{II} configurations.[105] This conclusion is

consistent with the observed prominent peak at ~7725 eV in the XANES spectra and with the increased valence state of Co after removing the applied cathodic potential (**Figures S79a and S80a,b**).

7.3 *Operando* XAS investigations of Co@CoFe-P towards HER

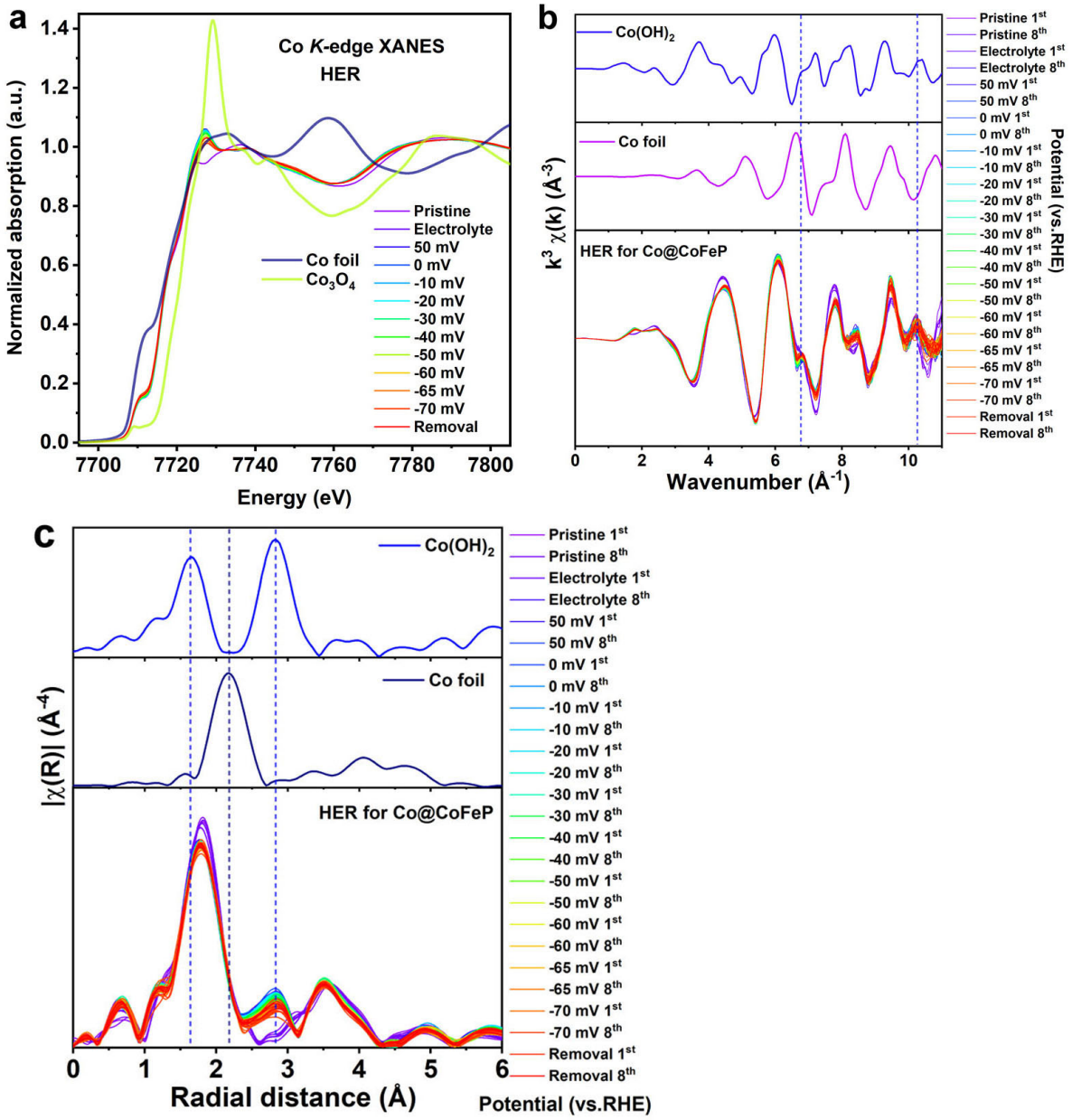

Figure S81. (a) Merged *operando* Co *K*-edge XANES spectra of Co@CoFe-P recorded at potentials from 50 mV to -70 mV (vs. RHE) in 1.0 M KOH towards HER as well as the Co foil and Co_3O_4 references. (b, c) *Operando* Co *K*-edge EXAFS and FT-EXAFS spectra (recorded 8 times) of Co@CoFe-P towards HER vs. Co foil and $Co(OH)_2$ references.

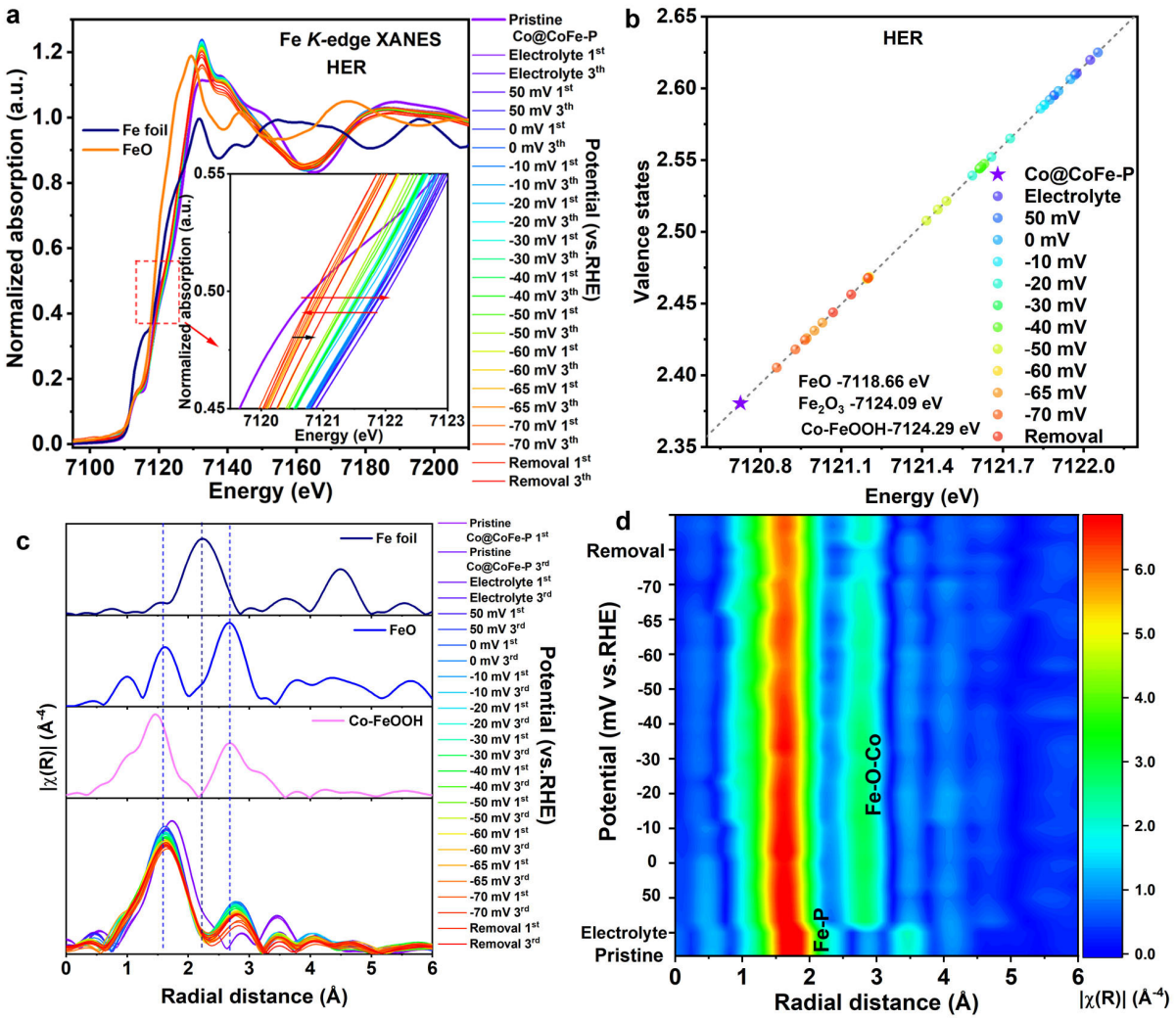

Figure S82. (a) *Operando* Fe *K*-edge EXAFS spectra (recorded 3 times) of Co@CoFe-P recorded at potentials from 50 mV to -70 mV (vs. RHE) in 1.0 M KOH towards HER as well as the references (Fe foil and FeO). (b) Calculated Fe valence states of Co@CoFe-P during HER. (c) *Operando* Fe *K*-edge FT-EXAFS spectra (recorded 3 times) of Co@CoFe-P towards HER. (d) 2D contour plots of *operando* Fe *K*-edge FT-EXAFS spectra of Co@CoFe-P towards HER.

Supplementary Discussion IV: *Operando* Fe-*K* edge XAS investigations of Co@CoFe-P NBs under HER conditions

Due to the fundamental technical challenges associated with acquiring high quality *operando* Fe *K*-edge XAS data of target compounds with low Fe contents, *operando* EXAFS analysis of the Fe *K*-edge was limited to the k range from 3 to 9 $Å^{-1}$ and the fitting of *operando* FT-EXAFS spectra was not performed. As shown in **Figure S82a,b**, during the cathodic polarization, the oxidation states of Fe ions follow a similar trend compared with that of Co (**Figure 4a,b**). In detail, the Fe valence increased from +2.38 to +2.61 after immersing the sample into the electrolyte. When applying cathodic potential, the oxidation state of Fe reached the lowest value of +2.41 at negative 70 mV vs. RHE. After removing the potential, it slightly recovered to +2.46, indicating the redox reversibility of Fe ions after the HER process. Moreover, the *operando* FT-EXAFS spectra and 2D contour plots (**Figure S82c,d**) indicate a noteworthy scattering peak of the second shell at the radial distance of 2.82 Å, which is slightly longer than the interatomic distance of the Fe^{II}-Fe^{II} path at 2.67 Å in reference FeO and the Co^{II}-Fe^{III} path at 2.69 Å in reference Co-FeOOH. With this information at hand, we proposed that the appearance of this second shell scattering in **Figure S82c,d** can mainly be ascribed to the formation of Co^{II}-O-Fe^{II} bonds (or P-Co-O-Fe-P configurations). Furthermore, the 2D contour plots of *operando* FT-EXAFS spectra (**Figure S82d**) illustrate a gradually decreasing trend in the scattering peak intensity of P-Co-O-Fe-P configurations during the cathodic polarization process. Moreover, it can be restored after removing the applied potential, indicating the reversibility of the atomic configuration of P-Co-O-Fe-P after the HER process. This is also consistent with our observations for Co *K*-edge FT-EXAFS spectra (**Figure 4c,d**). These *operando* results suggest that the *in situ* reconstructed P-Co-O-Fe-P configurations play a crucial role in the intrinsic HER activity of as-prepared Co@CoFe-P NBs.

7.4 *Operando* XAS investigations of Co-P towards OER

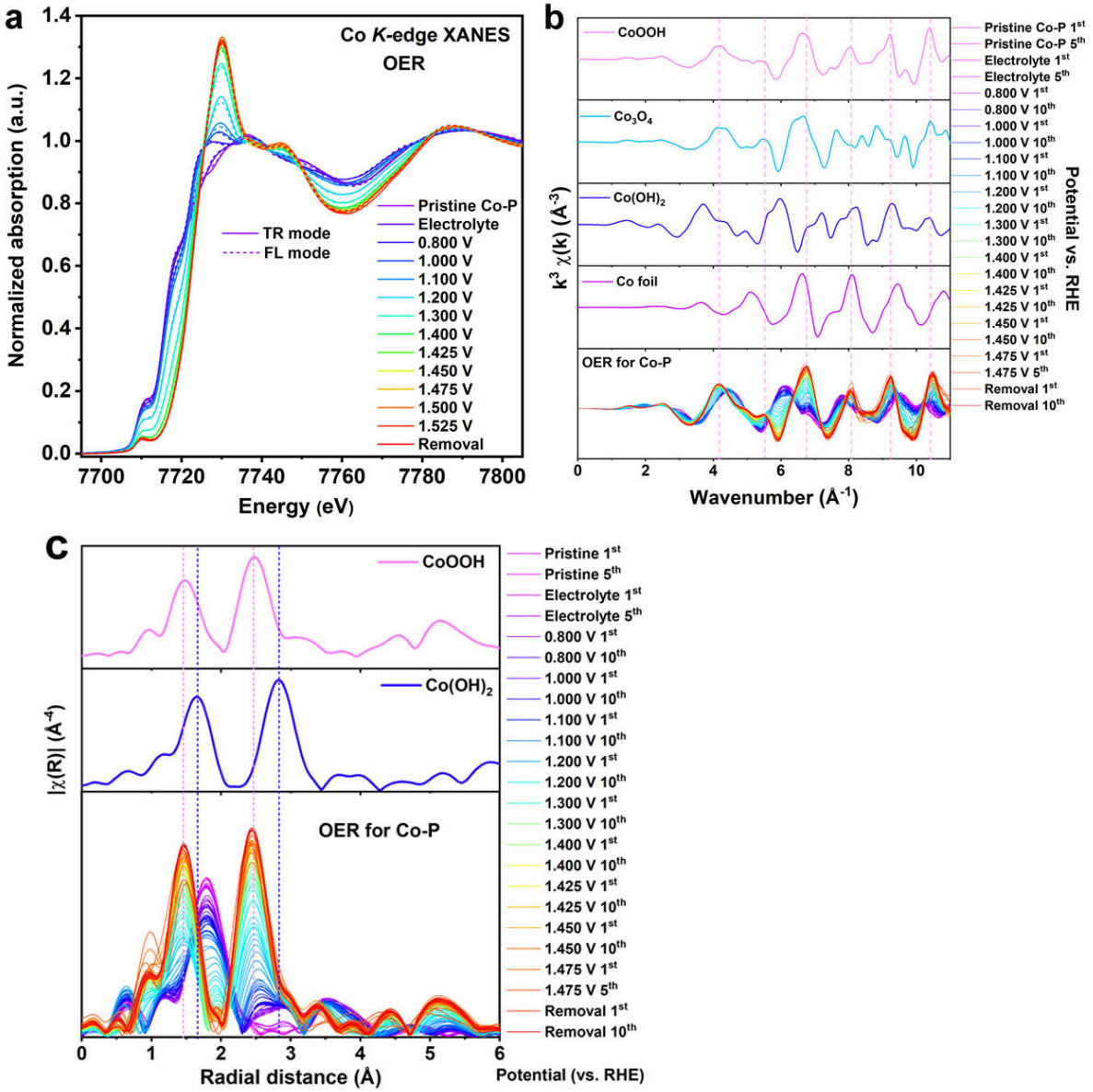

Figure S83. (a) Merged *operando* Co *K*-edge XANES spectra of Co-P recorded at potentials from 0.800 V to 1.525 V (vs. RHE) in 1.0 M KOH towards OER via both TR and FL modes. (b, c) *Operando* Co *K*-edge EXAFS and FT-EXAFS spectra (recorded 10 times) of Co-P towards HER vs. Co foil, $Co(OH)_2$, Co_3O_4, and CoOOH as references.

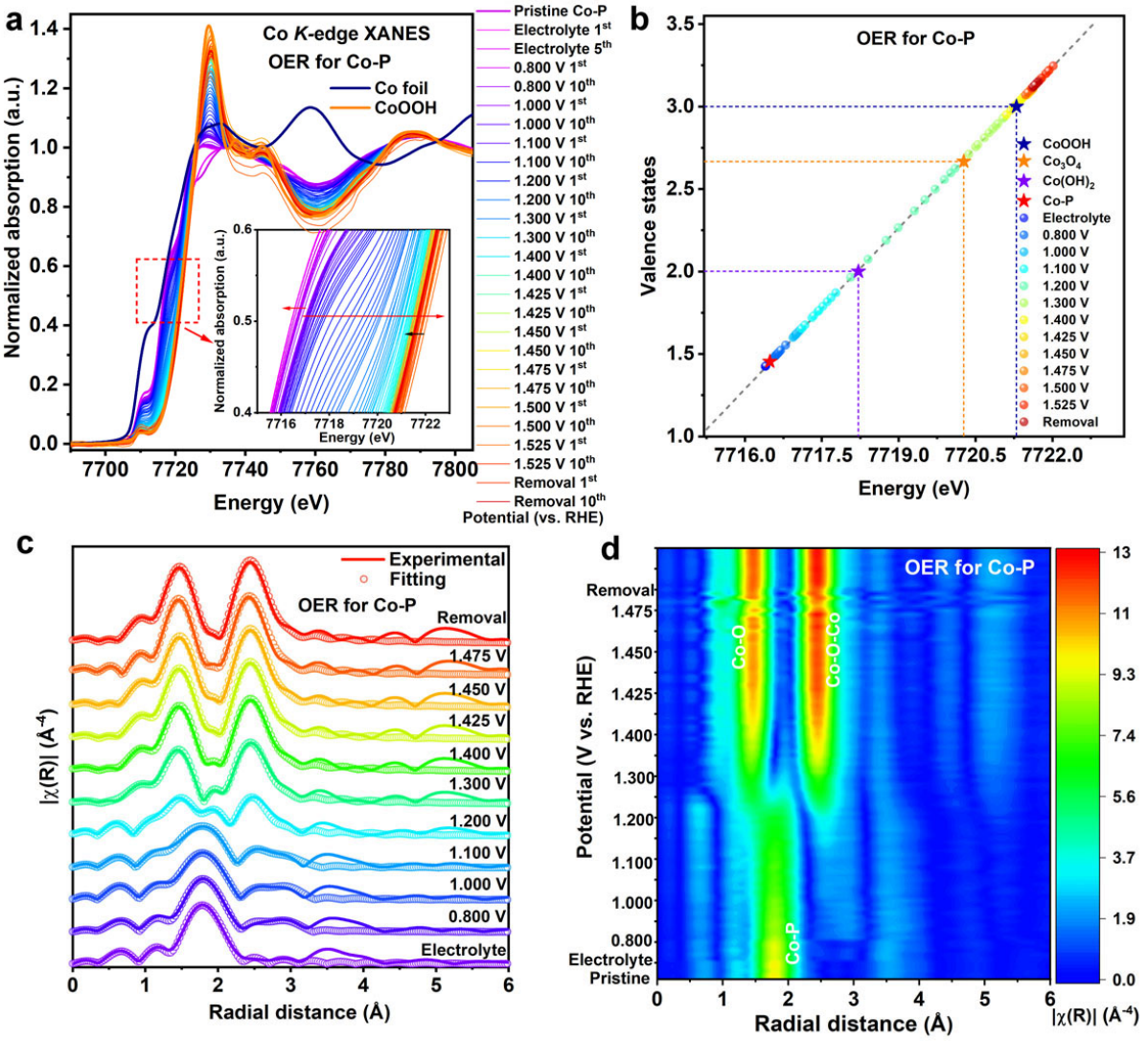

Figure S84. (a) *Operando* Co *K*-edge XANES spectra of Co-P recorded at different potentials in 1.0 M KOH for OER. (b) Calculated Co valence states of Co-P recorded at different potentials in 1.0 M KOH for OER. (c) Fitting of *operando* Co *K*-edge FT-EXAFS spectra (merged) of Co-P recorded at different potentials in 1.0 M KOH for OER. (d) 2D contour plots of *operando* Co *K*-edge FT-EXAFS spectra of Co-P recorded at different potentials in 1.0 M KOH for OER. (When the potential is higher than the onset potential for OER, the formation of gas bubbles drastically influences the quality of EXAFS data recorded in transmission mode. Therefore, we only present the XANES data without showing the EXAFS data when there was strong gas evolution.)

Supplementary Discussion V: Dynamics of active species in Co-P during the OER process

We further employed *operando* XAS to unveil the dynamics of structural reconstructions and to understand the intrinsic catalytic mechanisms for Co-P NBs and Co@CoFe-P NBs under OER conditions. **Figure S83** reveals similar line shapes in the XANES spectra of Co-P NBs recorded in both TR and FL mode, suggesting the reproducibility of the changes in the local electronic structures of Co centers during the OER process. As shown in **Figure 84a,** similar to the HER test (**Figure S80a**), the rising absorption edge of Co-P NBs immersed into the electrolyte shifts to lower energy compared to that of the pristine sample.[33,87] As the anodic potential increases from 0.8 V to 1.525 V vs. RHE, it moves towards higher energy. Likewise, the peak intensity at ~7730 eV increases as a function of the applied potential, indicating a gradual increase of the oxidation state of Co as shown in **Figure S84b**, and an increase of CN_{Co-O}. A maximum value of +3.24, compared to that of the pristine sample of +1.45, is attained at an anodic potential of 1.525 V vs. RHE. After removing the applied anodic potential, the value decreases again to +3.13, suggesting partial reversibility in the valence state of Co after the OER. The local coordination environments of Co centers were further evaluated from *operando* EXAFS spectra analyses. As shown in **Figure S83b** for different anodic polarizations, the *operando* EXAFS spectra show new oscillations appearing at k values of 4.17, 5.23, 6.75, 8.07, 9.25, and 10.42 $Å^{-1}$. These newly generated oscillations match well with $Co(OH)_2$ and CoOOH references. Moreover, $Co(OH)_2$ shows different EXAFS oscillations at k values of 4.17 and 6.75 $Å^{-1}$ with respect to CoOOH, thus corroborating the structural transformation from $Co(OH)_2$ to CoOOH based on EXAFS data (**Figure S83b**). As expected, a closer investigation of the *operando* EXAFS spectra of Co-P NBs (**Figure S83b**) reveals that the structural transformation ($Co(OH)_2$ to CoOOH) occurs at 1.1 V vs. RHE. Furthermore, the local coordination environments of Co centers in Co-P NBs were investigated by *operando* FT-EXAFS spectra (**Figure S83d and S84c**). The fitting results (**Table S9**) show that CN_{Co-P} gradually decreases from 5.45 (electrolyte) to 0 (1.425 V vs. RHE). Unlike the changes in CN_{Co-P}, both CN_{Co-O} and CN_{Co-Co} (**Table S9**) increase from 0.58 (electrolyte) to 5.09 (1.425 V vs. RHE) and from 0 (electrolyte) to 4.25 (1.425 V vs. RHE), respectively. The presence of Co^{II} and Co^{III} can be distinguished from the second Co-Co scattering shell since the interatomic distance of Co^{II}-Co^{II} of 3.18 Å in $Co(OH)_2$ is distinct from the Co^{III}-Co^{III} distance of 2.85 Å in CoOOH (**Figure S83c, Table S5**). As shown in **Table S9**, $CN_{CoII-CoII}$ reaches a maximum value of 0.89 at 1.0 V vs. RHE but thereafter disappears after 1.1 V vs. RHE. In contrast, $CN_{CoIII-CoIII}$ continuously increases from 0.49 to 4.39 as the potential increases from 1.1 V to 1.475 V vs. RHE.

From our observations (**Figure S83b**), the structural transformation from $Co(OH)_2$ to CoOOH occurs at the anodic potential of 1.1 V vs. RHE. This reconstruction agrees with previous CV analyses (**Figure S77 and Supplementary Discussion II**) and is also consistent with the theoretical standard redox potential of $Co(OH)_2$/CoOOH (1.030 V vs. RHE).[102,103] The *operando* FT-EXAFS spectra and the 2D contour plots (**Figures S83c and S84c,d**) show that when the anodic potential is higher than 1.1 V vs. RHE, the intensity of the second shell scattering peak at 2.52 Å increases due to the formation of a larger number of Co^{III}-O-Co^{III} bonds. Moreover, the first shell scattering peak at 1.78 Å (contributed by Co^{II}-O and Co-P bonds) gradually decreases until 1.1 V vs. RHE and becomes broader from 1.1 V to 1.2 V vs. RHE. For the cathodic potentials of 1.2 V to 1.3 V vs. RHE, the first shell scattering peak splits into two new peaks with the first located at 1.47 Å for Co^{III}-O bonds and the second one at 1.92 Å

for Co-P bonds. For applied potentials above 1.4 V vs. RHE, the scattering from Co-P bonds disappears and only the scattering from Co^{III}-O bonds remains in the first shell. Furthermore, peaks corresponding to Co^{III}-O and Co^{III}-Co^{III} shells (**Figure S84d**) are observed with a slightly weakening intensity between 1.45 V to 1.475 V vs. RHE, possibly due to the formation of Co^{IV}-O and Co^{IV}-O-Co^{IV} species.[33,105-107] The observation of Co oxidation states above +3 above 1.4 V vs. RHE supports our proposed formation of Co^{IV} species (**Figure S84b**). After removing the applied potential, the oxidation states of Co and the peak intensities of the first and second shell scattering are partially recovered (**Figure S84a,d**), verifying the redox reversibility of Co^{III}/Co^{IV} species after the OER process.

Fitting results for *operando* FT-EXAFS spectra during OER (**Figure S84c** and **Table S9)** further demonstrate decreasing values of $CN_{Co\text{-}P}$ and $CN_{CoII\text{-}CoII}$ and a gradual increase of $CN_{CoIII\text{-}CoIII}$. Based on these findings, we propose the following multistep evolution of the structural reconstruction and the catalytically active species in Co-P NBs. First, the formation of Co-$P_{6-x}O_x$ species occurs from the electrolyte up to 1.0 V vs. RHE, owing to the intrinsic thermodynamic instability of phosphides.[102] Next, the redox reaction of Co^{II}/Co^{III} promotes the structural evolution into Co-$P_{6-x}O_x$@$Co(OH)_2$@CoOOH species at 1.1 V vs. RHE. Increasing the anodic potential from 1.2 V to 1.4 V vs. RHE produces Co-$P_{6-x}O_x$ @$Co(OH)_2$(transient)@CoOOH species. The entire structural reconstruction from Co-P to CoOOH is completed above 1.425 V vs. RHE. During O_2 release (above 1.450 V vs. RHE), the *in situ* reconstructed $Co^{IV}O_2$ (Co^{IV}-O-Co^{IV}) units act as the real catalytically active species.[33,105-107] Finally, when the applied potential is removed, the active species of $Co^{IV}O_2$ recover to CoOOH. Regarding the anodic potential between 1.2 V to 1.4 V vs. RHE, we believe that Co-P would first be converted into transient $Co(OH)_2$ species and then be further oxidized to CoOOH. The absence of $Co(OH)_2$ in the fitting of FT-EXAFS spectra of Co-P NBs is primarily due to its very short lifetime at high potential ($Co(OH)_2$/CoOOH at 1.030 V vs. RHE), which cannot be detected in EXAFS spectra (**Figure S84c,d and Tables S9**). The overall structural reconstructions in Co-P NBs can be described with the following equations:

$$CoP + 2xOH^- \longrightarrow CoPO_x + x\,H_2O + 2xe^- \qquad \text{(electrolyte)}$$

$$CoPO_x + 2OH^- \longrightarrow Co(OH)_2 + PO_x^{2-} \qquad (<1.1\text{ V vs. RHE})$$

$$Co(OH)_2 \longrightarrow CoOOH + H^+ + e^- \qquad (1.1\text{V to } 1.45\text{ V vs. RHE})$$

$$CoOOH \longrightarrow CoO_2 + H^+ + e^- \qquad (>1.45\text{V vs. RHE})$$

7.5 *Operando* XAS investigations of Co@CoFe-P towards OER

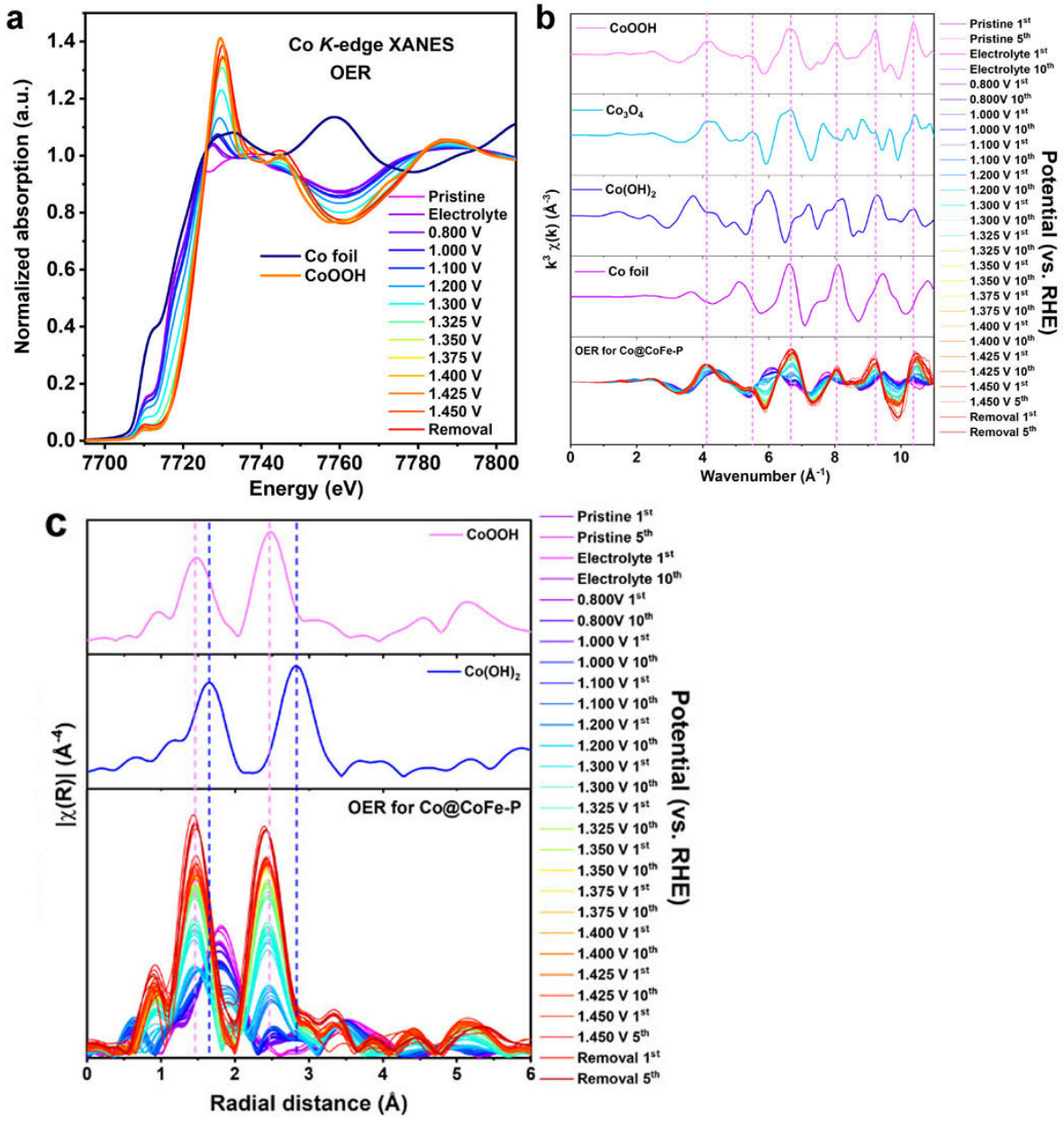

Figure S85. (a) Merged *operando* Co *K*-edge XANES spectra of Co@CoFe-P NBs recorded at potentials from 0.800 V to 1.450 V (vs. RHE) in 1.0 M KOH towards OER vs. reference Co foil and CoOOH. (b, c) *Operando* Co *K*-edge EXAFS and FT-EXAFS spectra (recorded 10 times) of Co@CoFe-P NBs towards OER vs. references: Co foil, $Co(OH)_2$, Co_3O_4, and CoOOH.

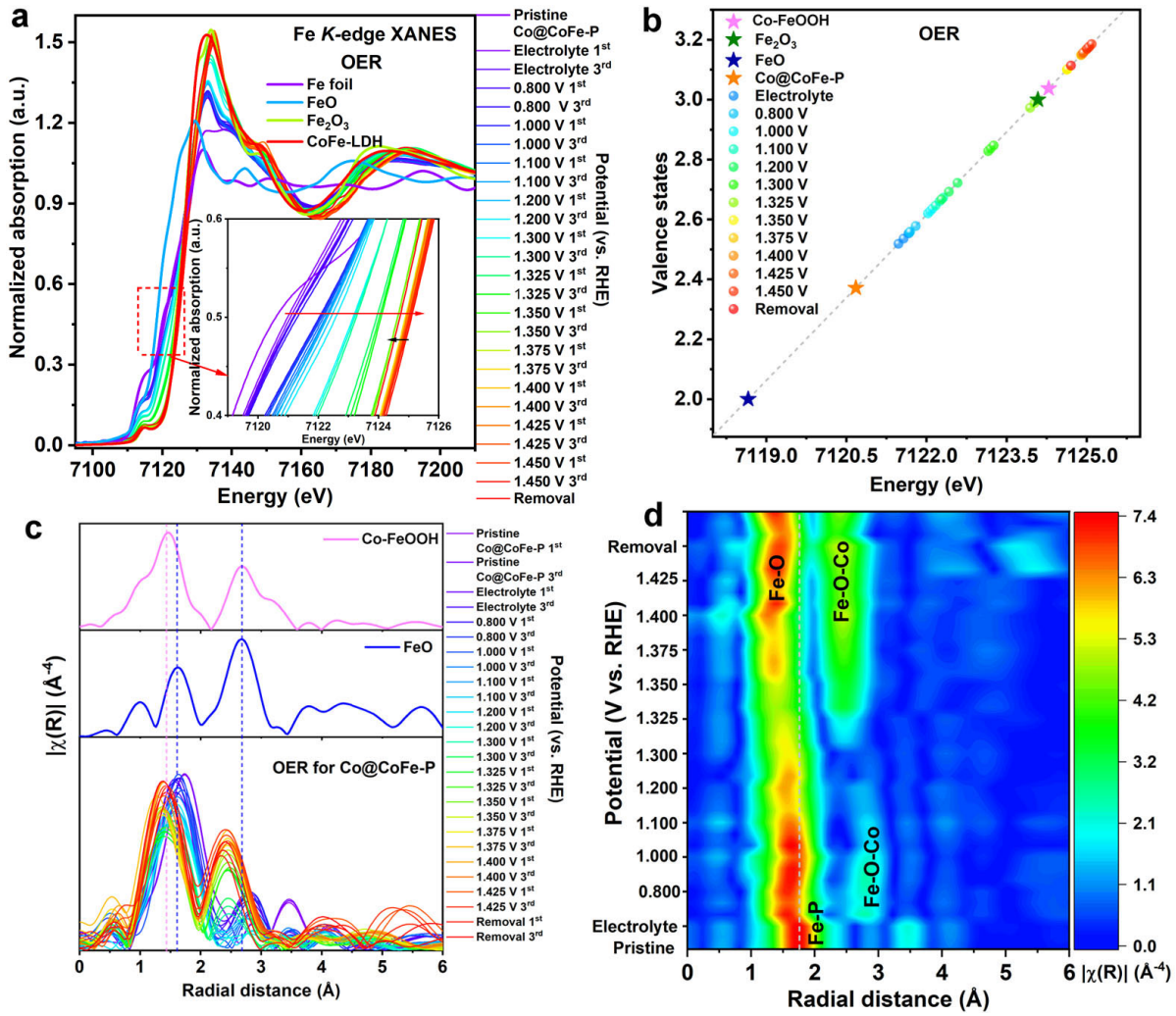

Figure S86. (a) *Operando* Fe *K*-edge XANES spectra (recorded 3 times) of Co@CoFe-P recorded at potentials from 0.800 V to 1.450 V (vs. RHE) in 1.0 M KOH towards OER vs. reference Fe foil, FeO, Fe_2O_3, and Co-FeOOH. (b) Calculated Fe valence states of Co@CoFe-P recorded at different potentials. (c) *Operando* Fe *K*-edge FT-EXAFS spectra (recorded 3 times) of Co@CoFe-P recorded at different potentials as well as of FeO and Co-FeOOH references. (d) 2D contour plots of *operando* Fe *K*-edge FT-EXAFS spectra (recorded 3 times) of Co@CoFe-P recorded at different potentials.

Supplementary Discussion VI: *Operando* Fe-*K* edge XAS investigations of Co@CoFe-P NBs under OER conditions

Figure S86a,b presents the *operando* Fe *K*-edge XANES spectra and the changes of Fe oxidation states of Co@CoFe-P NBs towards OER. The energy position of the rising absorption edge presents a continuously increasing trend towards higher energy with higher anodic potential, indicating the increase of the Fe oxidation state. For an applied potential above 1.325 V vs. RHE (**Figure S86b**), the oxidation state of Fe reaches +3. Furthermore, a maximum value of +3.18 is obtained with an anodic potential of 1.450 V vs. RHE. The local coordination environments of Fe centers were further monitored with *operando* FT-EXAFS spectra. As shown in **Figure S86c,d**, for Co@CoFe-P NBs immersed into the electrolyte, a prominent second shell scattering is observed in the FT-EXAFS spectra with a radial distance at 2.82 Å, which reflects the formation of Co^{II}-O-Fe^{II} bonds. When the anodic potential is higher than 1.0 V vs. RHE, the intensity of the second shell scattering shows a decreasing trend, indicating the formation of Co^{III}-O-Fe^{II} bonds. It should be noted the second shell scattering of the Co^{II}-Fe^{II} path becomes less pronounced at the potential between 1.2 V to 1.3 V vs. RHE. However, the second shell scattering reappears at 2.48 Å and shows an increasing trend as the potential is above 1.3 V vs. RHE. Based on the changes of the oxidation states of Co and Fe (**Figure 4f and Figure S86b**), the newly formed scattering peak of the second shell at 2.48 Å arises from Co^{III}-O-Fe^{III} bonds. With a further increase of the potential up to 1.4 V vs. RHE, both the first and second shell scatterings exhibit slightly weaker intensities, mainly ascribed to the formation of the high valent Co^{IV} and Fe^{IV} species (**Figure 4f and Figure S86b**). After removing the applied potential, the oxidation state and the coordination environments of Fe ions were somewhat recovered (**Figure S86b,d**), indicating the redox reversibility of Fe^{III}/Fe^{IV} species after the catalytic reaction.

7.6 *Operando* XAS investigations of Co-FeOOH towards OER

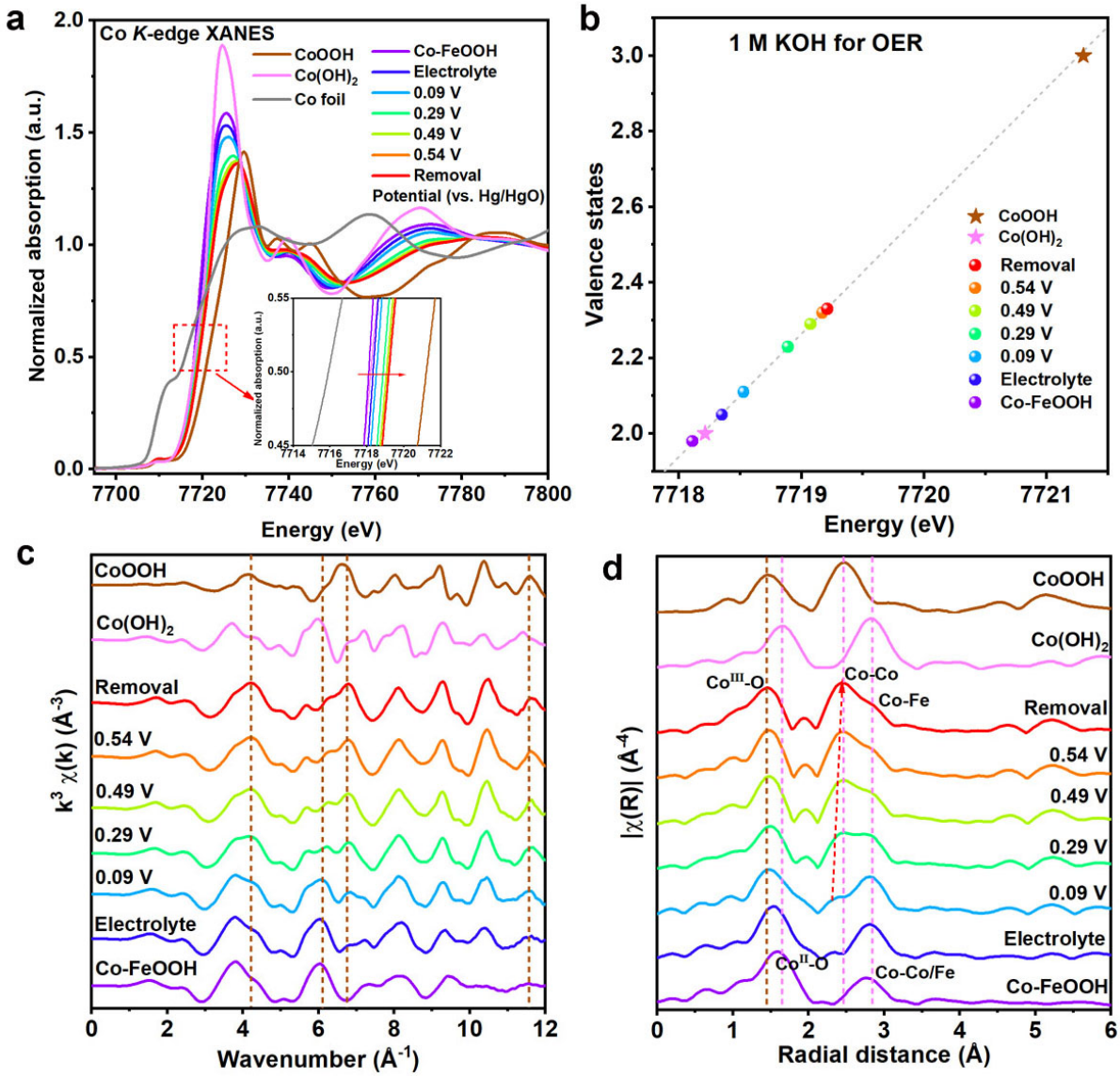

Figure S87. (a) *Operando* Co *K*-edge XANES spectra (recorded 3 times) of Co-FeOOH recorded at potentials from 0.09 V to 0.54 V (vs. Hg/HgO) in 1.0 M KOH towards OER vs. reference Co foil, $Co(OH)_2$, and CoOOH. (b) Calculated Co valence states of Co-FeOOH recorded at different potentials. (c, d) *Operando* Co *K*-edge EXAFS and FT-EXAFS spectra (recorded 3 times) of Co-FeOOH recorded at different potentials as well as reference samples of $Co(OH)_2$, and CoOOH.

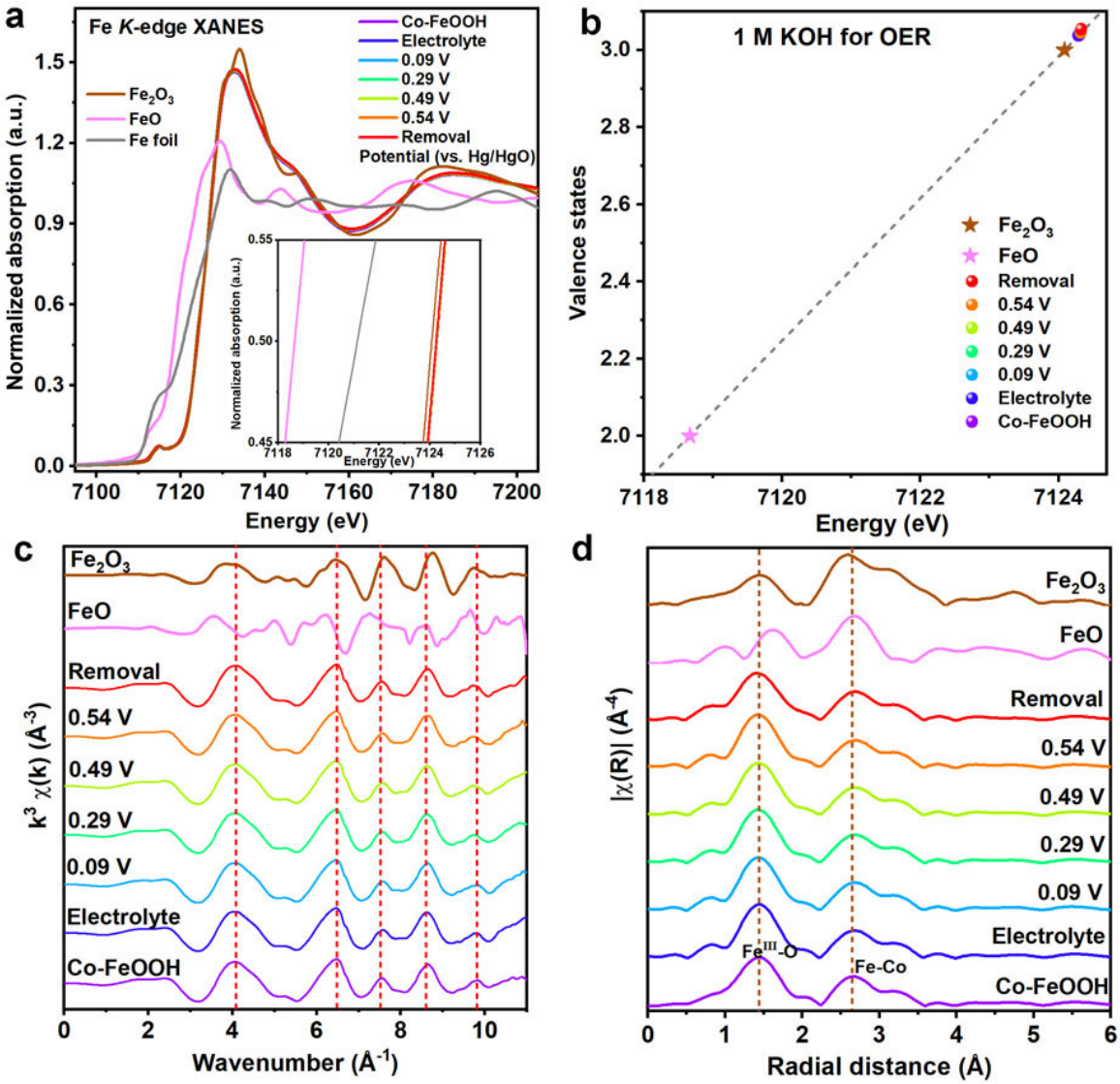

Figure S88. (a) *Operando* Fe *K*-edge XANES spectra (recorded 3 times) of Co-FeOOH at potentials from 0.09 V to 0.54 V (vs. Hg/HgO) in 1.0 M KOH towards OER versus Fe foil, FeO, and Fe_2O_3 as references. (b) Calculated Fe valence states of Co-FeOOH recorded at different potentials. (c, d) *Operando* Fe *K*-edge EXAFS and FT-EXAFS spectra (recorded 3 times) of Co-FeOOH at different potentials as well as FeO and Fe_2O_3 references.

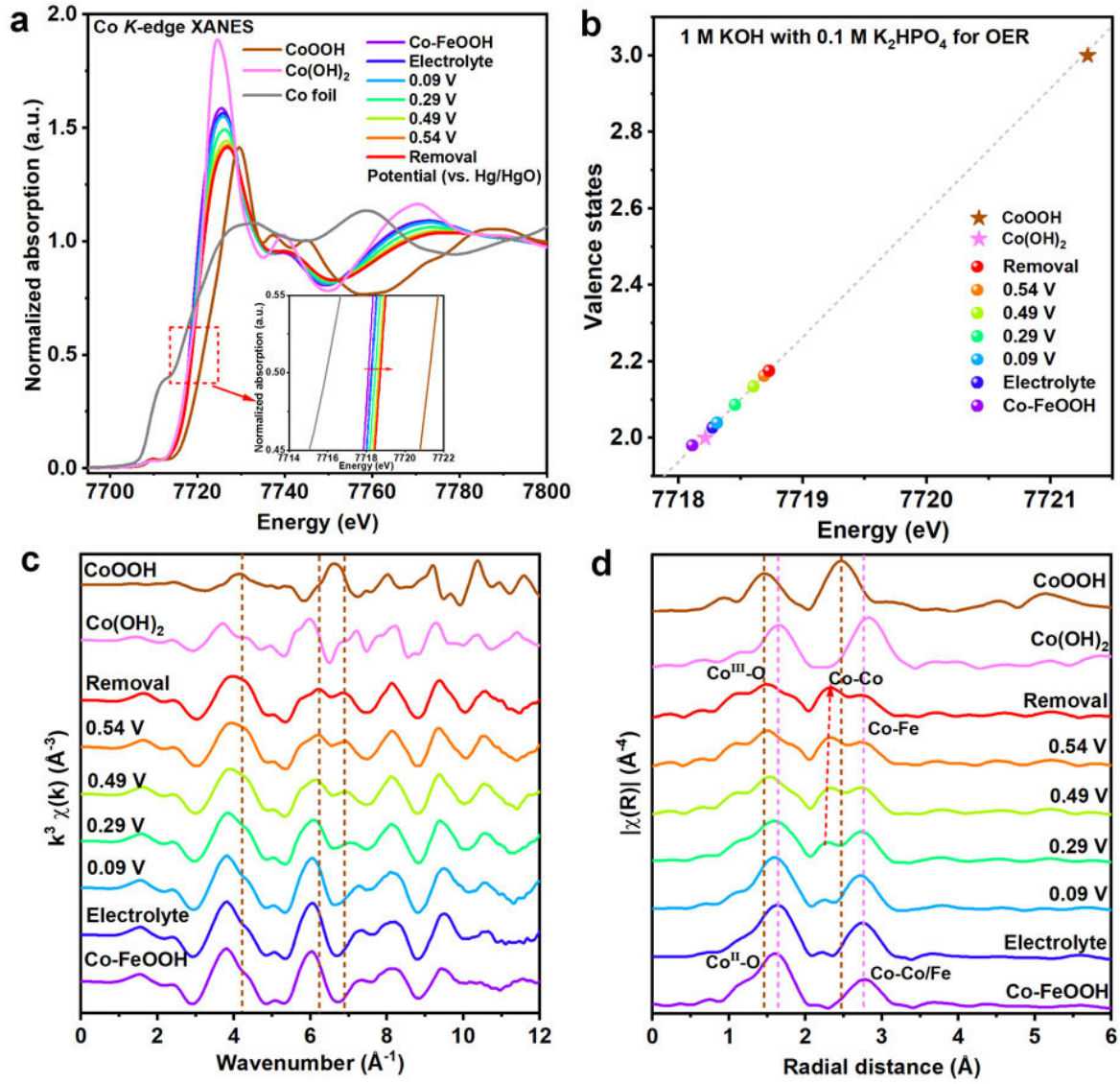

Figure S89. (a) *Operando* Co *K*-edge XANES spectra (recorded 3 times) of Co-FeOOH at potentials from 0.09 V to 0.54 V (vs. Hg/HgO) in 1.0 M KOH with 0.1 M K_2HPO_4 towards OER vs. reference Co foil, $Co(OH)_2$, and CoOOH. (b) Calculated Co valence states of Co-FeOOH recorded at different potentials. (c, d) *Operando* Co *K*-edge EXAFS and FT-EXAFS spectra (recorded 3 times) of Co-FeOOH at different potentials as well as $Co(OH)_2$ and CoOOH references.

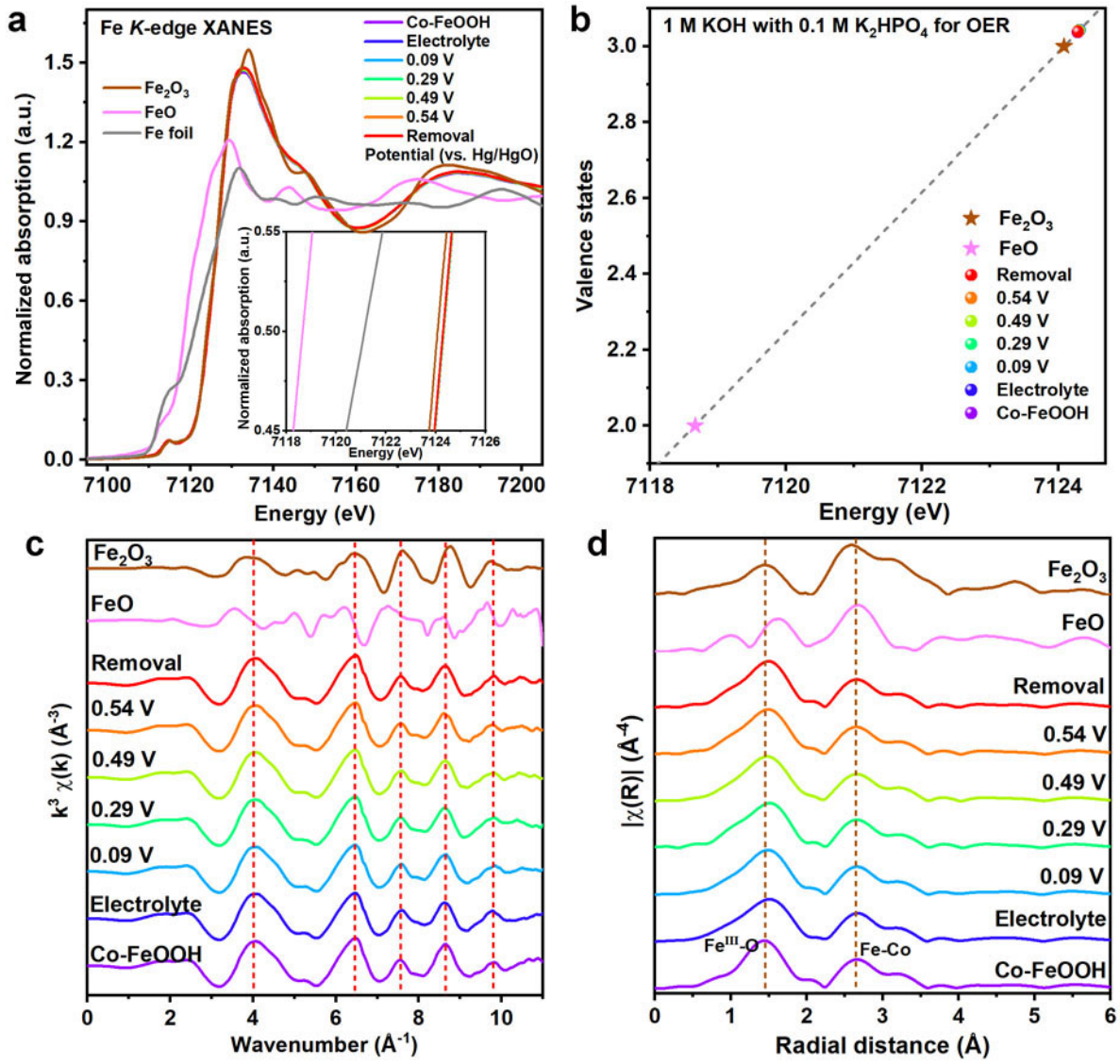

Figure S90. (a) *Operando* Fe *K*-edge XANES spectra (recorded 3 times) of Co-FeOOH at potentials from 0.09 V to 0.54 V (vs. Hg/HgO) in 1.0 M KOH with 0.1 M K_2HPO_4 towards OER vs. reference Fe foil, FeO, and Fe_2O_3. (b) Calculated Fe valence states of Co-FeOOH recorded at different potentials. (c, d) *Operando* Fe *K*-edge EXAFS and FT-EXAFS spectra (recorded 3 times) of Co-FeOOH recorded at different potentials as well FeO and Fe_2O_3 references.

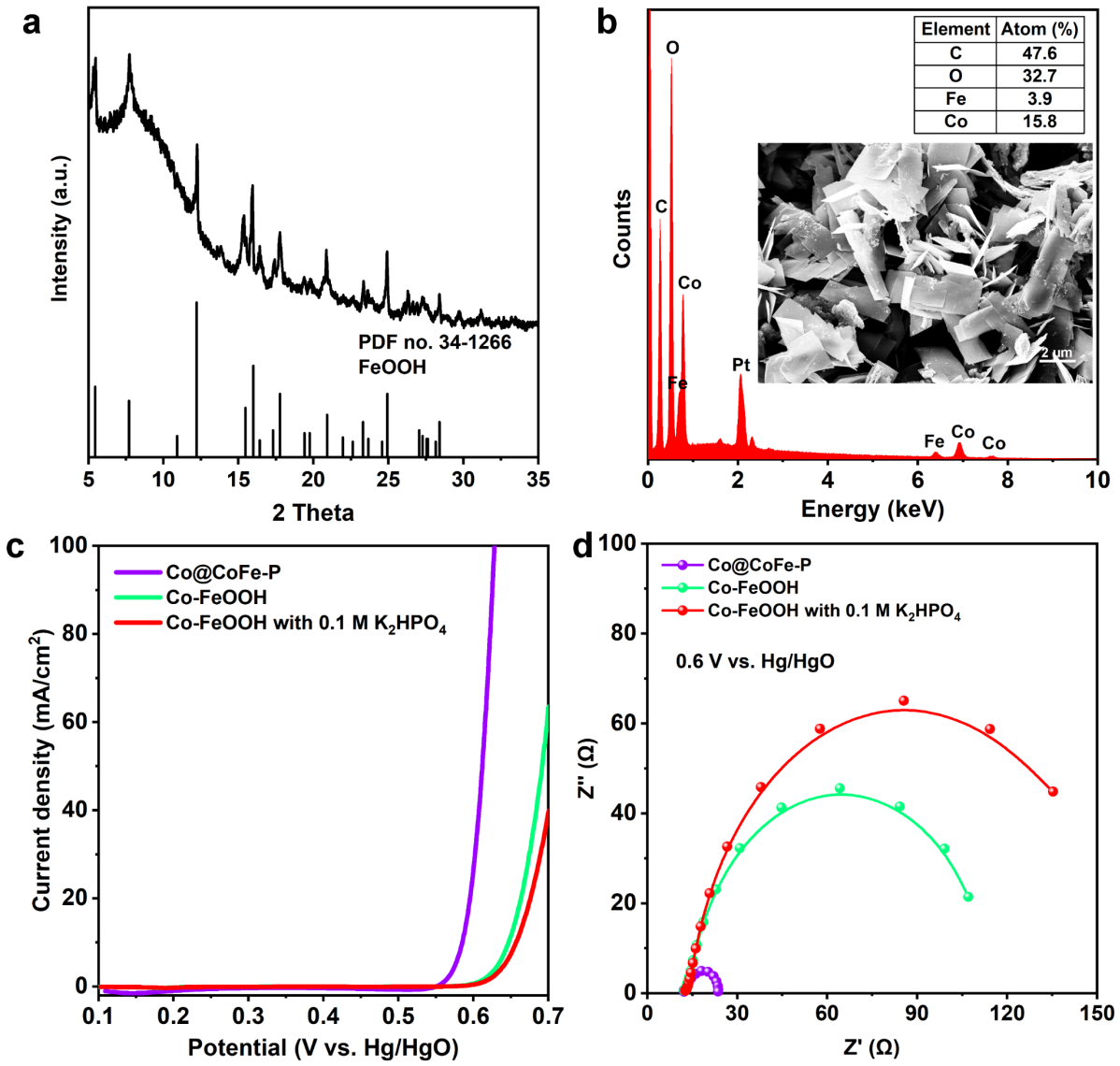

Figure S91. (a) PXRD pattern of as-prepared Co-FeOOH. (b) EDX spectrum and SEM image of as-prepared Co-FeOOH. (c) LSV curves of Co@CoFe-P and Co-FeOOH in 1.0 M KOH and Co-FeOOH in 1.0 KOH with 0.1 M K_2HPO_4. (d) Nyquist plots.

Supplementary Discussion VII: *Operando* XAS investigations of Co-FeOOH under OER conditions

To further unveil the origins of the intrinsic OER activity of as-prepared Co@CoFe-P NBs, we recorded the *operando* XAS data of Co-FeOOH during the OER. As demonstrated in **Figure S87a,b**, with the anodic polarizations, the valence states of Co show an increasing tendency with a maximum of +2.32 at 0.54 V vs. Hg/HgO (1.0 M KOH). Moreover, the *operando* Co *K*-edge EXAFS and FT-EXAFS spectra of Co-FeOOH at 0.54 V vs. Hg/HgO (1.0 M KOH) present similar scattering features compared with that of CoOOH. This demonstrates the formation of Co^{3+} species in Co-FeOOH for OER. However, the *operando* Fe *K*-edge XAS data remain unchanged during the OER process (**Figure S88**). Based on the results of *operando* Fe *K*-edge XAS in Co@CoFe-NB (**Figure S86**), the backscattering of Co^{II}-Fe^{III} and Co^{III}-Fe^{III} shows a distinct radial distance in the Fe *K*-edge FT-EXAFS spectra. Therefore, it is safe to conclude that the unchanged second scattering peak is mainly contributed by the backscattering of the Co^{II}-Fe^{III} path. The appearance of scattering peaks at 2.45 Å and 2.85 Å in **Figure S87b** are arising from the backscattering of Co^{III}-Co^{III} and Co^{II}-Fe^{III}, respectively. This further substantiates that Co@CoFe-P NBs as OER catalysts promote the formation of $Co^{III/IV}$-$Fe^{III/IV}$ moieties.

The influence of leached PO_x in the local electronic structures of Co-FeOOH was also investigated with *operando* XAS. As shown in **Figures S89 and S90**, both the Co and Fe *K*-edge XAS data of Co-FeOOH with the addition of 0.1 M K_2HPO_4 show similar spectroscopic features compared with those in pure 1.0 M KOH (**Figures S87 and S88**). With the appearance of PO_x in the electrolyte, the valence state of Co (**Figure S89b**) reached a maximum value of +2.16 at 0.54 V vs. Hg/HgO, which is lower than in the absence of K_2HPO_4 (+2.32, **Figure S87b**). The delayed formation of the high valence state of Co (> +2) with the addition of 0.1 M K_2HPO_4 is mainly due to changes in the pH value (**Table S4**).[7,96] In other words, these results (**Figures S87-S90**) reflect that the formation of $Co^{III/IV}$-$Fe^{III/IV}$ species in Co-FeOOH is much more difficult when compared with Co@CoFe-P. Moreover, the leaching of PO_x species into the electrolyte does not play a vital role in the formation of the high valent (Co^{IV}, Fe^{IV})O_2 species. According to the results for Co-P and Co@CoFe-P, we believe that the main driving force, which promotes the formation of the high valence state of active species, is originating from the highly disordered intermediates during the structural reconstruction (**Figure 4**). These observations can further explain why Co@CoFe-P displays much better OER activity compared with Co-FeOOH (**Figure S91**).

8. *Ex situ* XAS characterization of reference chalcogenides for HER and OER

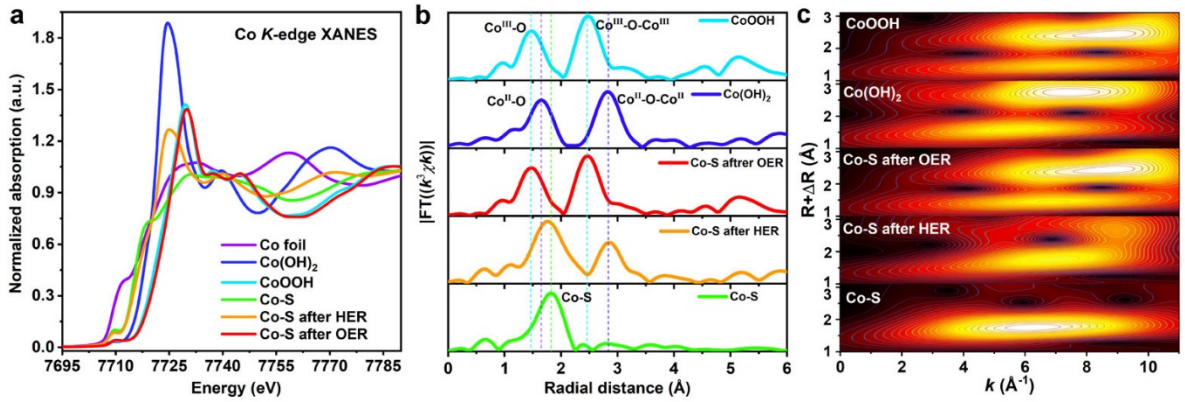

Figure S92. (a, b) Co *K*-edge XANES and FT-EXAFS spectra of as-synthesized Co-S NBs before and after HER (1.0 M KOH) and OER (1.0 M KOH) vs. references. (c) WT contour profiles of Co-S, Co-S after HER, Co-S after OER, $Co(OH)_2$, and CoOOH.

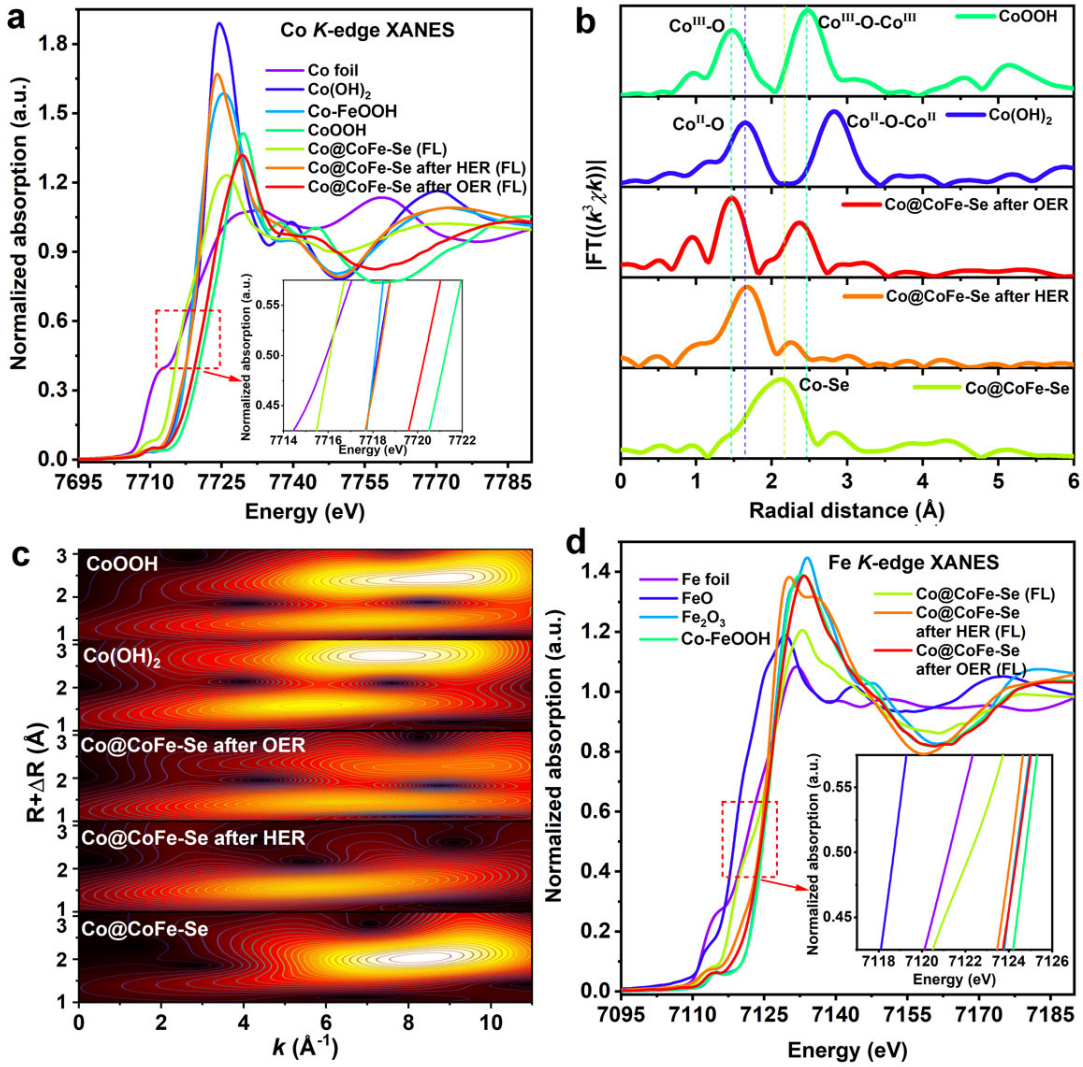

Figure S93. (a, b) Co *K*-edge XANES and FT-EXAFS spectra of as-synthesized Co@CoFe-Se before and after HER (1.0 M KOH) and OER (1.0 M KOH) vs. references. (c) WT contour profiles of Co@CoFe-Se, Co@CoFe-Se after HER, Co@CoFe-Se after OER, $Co(OH)_2$, and CoOOH. (d) Fe *K*-edge XANES spectra of as-synthesized Co@CoFe-Se and the samples after HER (1.0 M KOH) and OER (1.0 M KOH) vs. references.

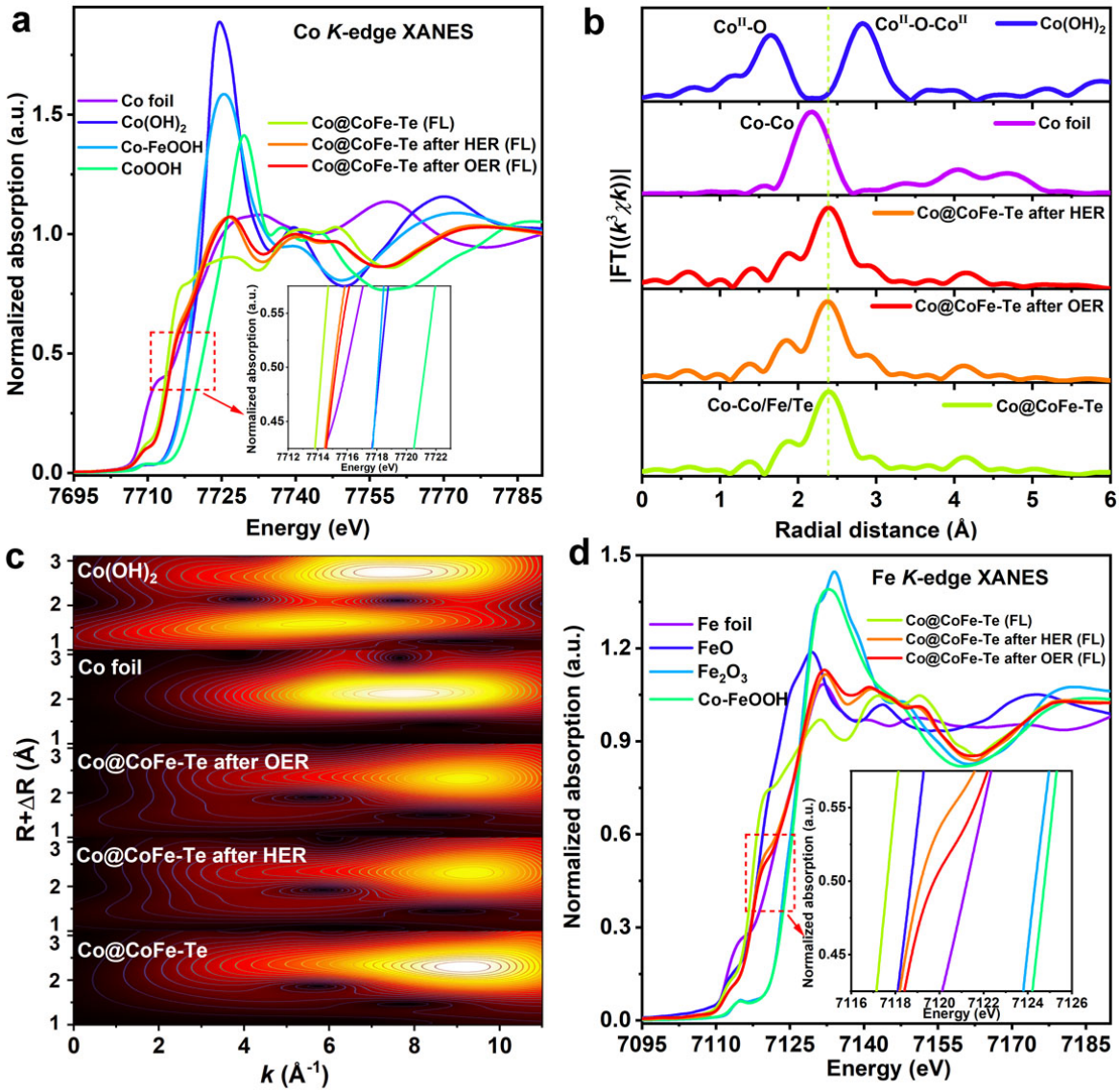

Figure S94. (a, b) Co *K*-edge XANES and FT-EXAFS spectra of as-synthesized Co@CoFe-Te before and after HER (1.0 M KOH) and OER (1.0 M KOH) vs. references. (c) WT contour profiles of Co@CoFe-Te, Co@CoFe-Te after HER, Co@CoFe-Te after OER, Co foil, and CoOOH. (d) Fe *K*-edge XANES spectra of as-synthesized Co@CoFe-Se and the samples after HER (1.0 M KOH) and OER (1.0 M KOH) vs. references.

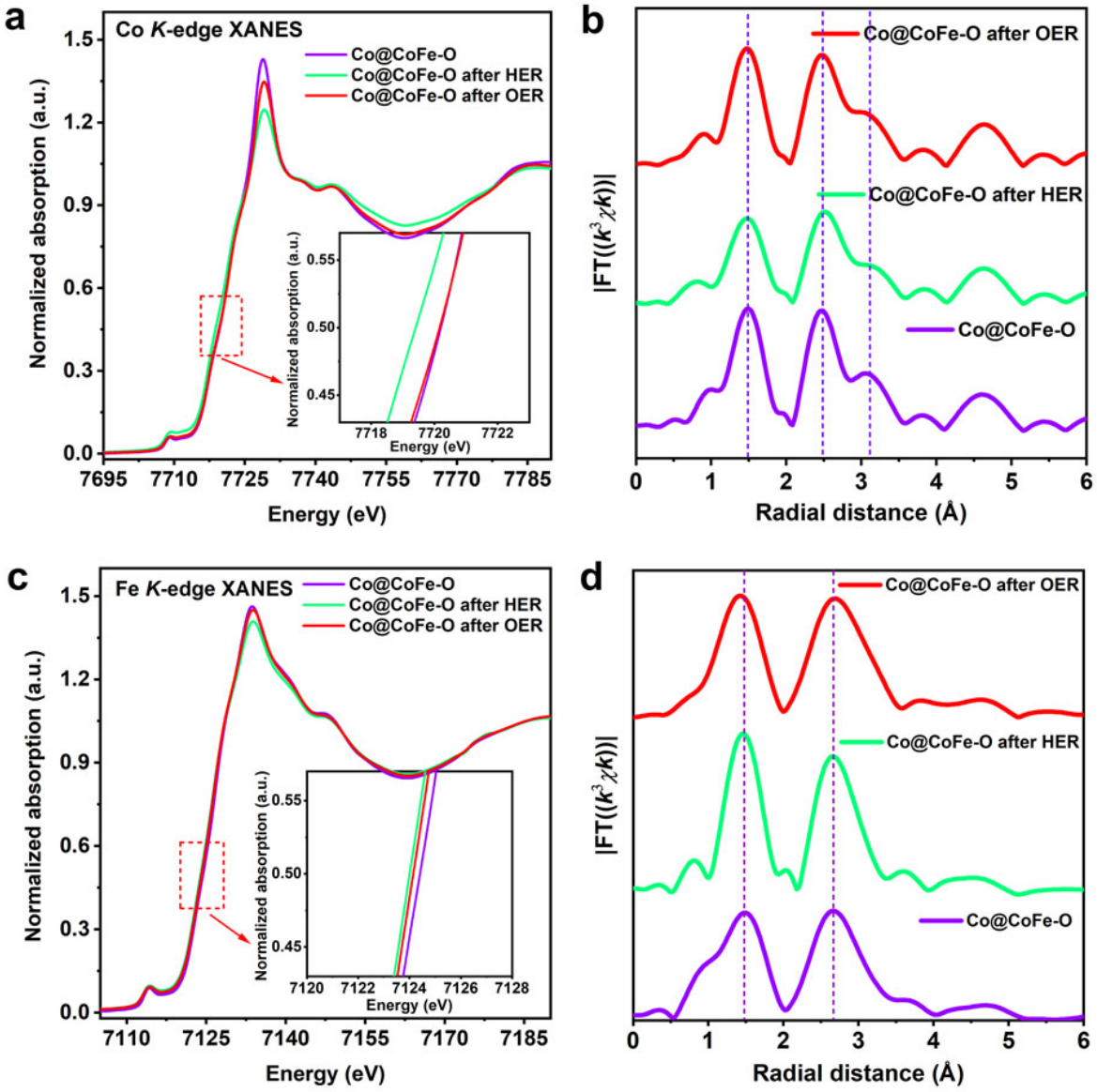

Figure S95. (a, b) Co *K*-edge XANES and FT-EXAFS spectra of as-synthesized Co@CoFe-O before and after HER (1.0 M KOH) and OER (1.0 M KOH). (c, d) Fe *K*-edge XANES and FT-EXAFS spectra of as-synthesized Co@CoFe-O before and after HER (1.0 M KOH) and OER (1.0 M KOH).

Supplementary Discussion VIII: Structural dynamics of reference chalcogenides during the HER and OER processes

As demonstrated in **Figure S92**, we also investigated the underlying structural reconstructions and explored the real catalytic species in as-synthesized Co-S NBs after HER and OER with *ex situ* XAS. Concerning HER, the rising absorption edge of Co *K*-edge XANES spectra (**Figure S92a**) of Co-S after HER shifts towards higher energy, suggesting the formation of high valence states of Co centers after the HER process. Moreover, the appearance of a prominent peak at approximately 7725 eV indicates the stronger bonding contributions from Co and O atoms. These observations were further corroborated with post-catalytic Co *K*-edge FT-EXAFS spectra and WT contour profiles (**Figure S92b,c**), where the scattering contributions from the first Co-S shells are weakened compared with the pristine sample, reflecting the formation of S-Co-O configurations in the as-investigated Co-S NBs after HER. Other than for HER, the XAS results of Co-S NBs after OER (**Figure S92a,b**) exhibit similar electronic structures and coordination environments of Co centers compared with that of CoOOH, which agrees with our studies on Co-P NBs (**Figures S83 and S84**). **Figure S93** shows the *ex situ* Co and Fe *K*-edge XAS of Co@CoFe-Se and of the respective samples after HER and OER. As expected, the as-prepared Co@CoFe-Se underwent related structural reconstructions as Co-S (**Figure S92**) after the catalytic reactions. As shown in **Figures S93a**,**d**, both the Co and Fe *K*-edge XANES spectra of as-synthesized Co@CoFe-Se after HER show a positive shift towards higher energy, implying an increase of the oxidation states of Co and Fe after HER. Further investigation of the FT-EXAFS spectra and WT contour plots (**Figure S93b,c**) verifies that the backscattering contributions from the first shell of Co-Se bonds after the HER process are suppressed, mainly due to the formation of Co/Fe-O bonds. For the *ex situ* XAS after the OER process (**Figure S93b,c**), post-catalytic Co@CoFe-Se exhibits a similar electronic structure and coordination environment of Co centers compared to CoOOH, indicating the structural reconstruction into (Co, Fe)OOH in Co@CoFe-Se after the OER test. These observations are also in line with the above *operando* XAS studies of Co@CoFe-P NBs during the OER process (**Figures S85 and S86**). Regarding the XAS of Co@CoFe-Te after HER and OER (**Figure S94**), we observed that the rising absorption edge in both Co and Fe *K*-edge XANES spectra of Co@CoFe-Te shows a positive energy shift after the catalytic processes. Moreover, the post-catalytic samples exhibit an enhanced peak intensity at around 7725 eV in the Co *K*-edge and 7131 eV in the Fe *K*-edge XANES spectra (**Figure S94a,d**), respectively, indicating the formation of Co/Fe-O bonds after the reaction. A close inspection of the WT contour profiles for Co@CoFe-Te after HER and OER processes reveals weaker scattering contributions from Co-Co/Fe/Te bonds (**Figure S94c**). However, those findings are not prominent in the FT-EXAFS spectra (**Figure S94b**), where the samples show similar coordination environments of Co centers compared with that of pristine samples. This is mostly due to the overlapping scattering of M-O and M-Te bonds (M= Co/Fe), so that their scattering difference cannot be distinguished in FT-EXAFS spectra. All these results (**Figures S92-S94**) strongly confirm that the as-prepared TMCs undergo a similar structural reconstruction compared with TMPs during both HER and OER processes. We further recorded the XAS data of Co@CoFe-O before and after the catalytic reactions. As shown in **Figure S95**, both the Co and Fe *K*-edge XAS results demonstrate that the as-prepared Co@CoFe-O retains its initial spinel crystal structure after the OER process, indicating that the oxide-type samples do not undergo structural reconstructions. It should be noted that the intensity of white line features showed a trend to lower intensities, along with a negative energy shift in the rising absorption edge position (**Figure S95a,c**). This suggests that the Co/Fe-O

moieties adopted lower valence states to initiate the HER process, in line with our studies on TMPs and TMCs (**Figure 4 and Figures S92-S94**).

9. RRDE investigations of Co-P and Co@CoFe-P for OER

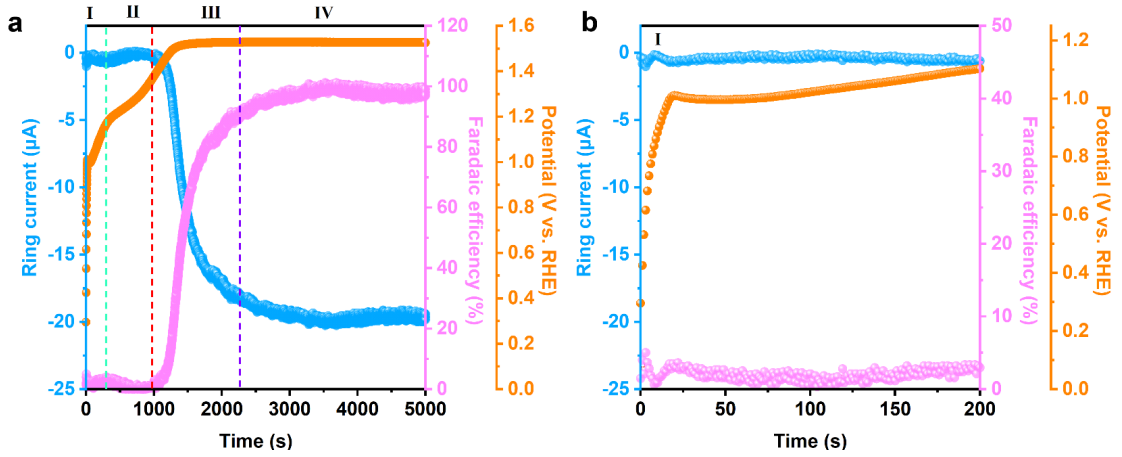

Figure S96. (a) RRDE tests of Co-P NBs towards OER in Ar saturated 1.0 M KOH. (b) Zoom of region I in **Figure 96a**.

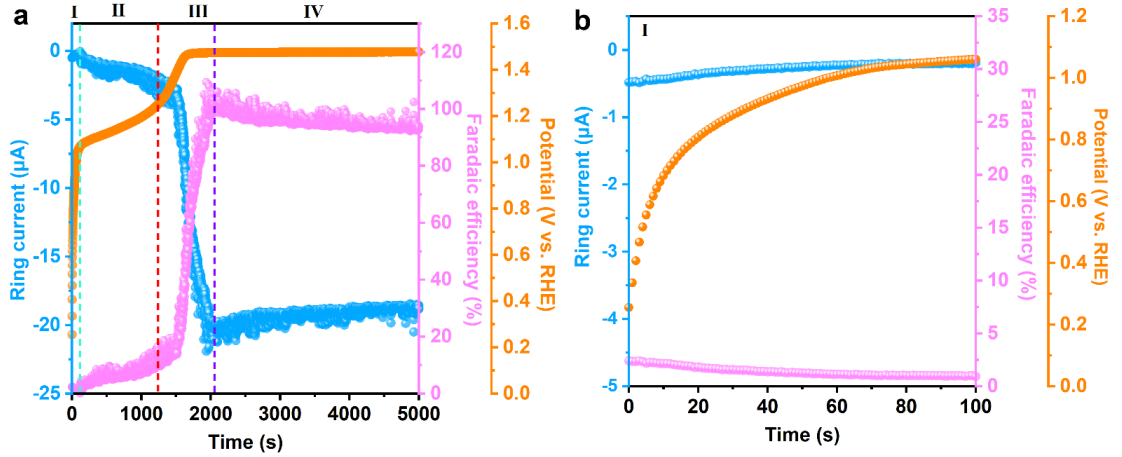

Figure S97. (a) RRDE tests of Co@CoFe-P NBs towards OER in Ar saturated 1.0 M KOH. (b) Zoom of region I in **Figure 97a**.

As demonstrated in **Figures S96 and S97**, Co-P NBs and Co@CoFe-P NBs exhibit similar electrochemical behavior during the RRDE tests. Based on the changes in the working electrode potentials and the calculated Faradaic efficiencies, we observed four different processes involved in the RRDE process. According to the *operando* XAS studies for Co-P NBs in **Figures S83 and S84**, we suggest that the appearance of region I (**Figure S96b**) is mainly due to the initial formation of Co-$P_{6-x}O_x$@$Co(OH)_2$ species, since the working potential is much lower than the standard redox potential for $Co(OH)_2$/CoOOH at 1.030 V vs. RHE.[102] After some time, the structural transformation from $Co(OH)_2$ to CoOOH occurs in region II. Notably, some unreacted Co-$P_{6-x}O_x$ species are first converted into $Co(OH)_2$ and further oxidized to CoOOH in region II. When the remaining Co-$P_{6-x}O_x$ species are quantitatively transformed into CoOOH, a further increase of the working potential triggers the oxidation reaction of CoOOH/CoO_2 at around 1.400 V vs. RHE in region III (**Figure S96a**). Our *operando* XAS results (**Figures S83 and S84**) infer that the *in situ* reconstructed CoO_2 species act as the real OER catalytic species, therefore, an increasing trend of OER current can be detected in region

III. When the equilibrium potential (1.525 V vs. RHE) between the accumulation of CoO_2 species and O_2 generation is reached, almost 100 % Faradaic efficiency is detected in region IV. It should be noted that the equilibrium potential in Co@CoFe-P NBs is observed at 1.475 V vs. RHE (**Figure S97a**), which is much lower than for Co-P NBs at 1.525 V vs. RHE (**Figure S96a**), indicating that partial Fe substitution can promote the structural reconstruction processes and lower the onset potential for OER.

10. *Operando* Raman studies of Co-P and Co@CoFe-P for HER and OER

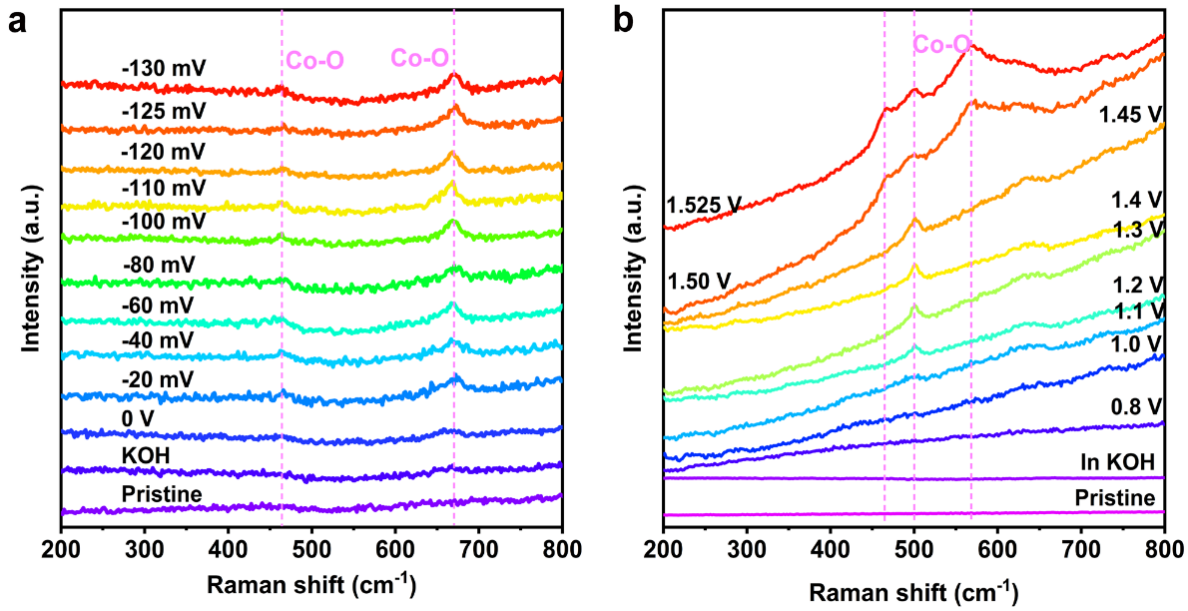

Figure S98. (a) *Operando* Raman measurements of Co-P towards HER between 0 V to -130 mV vs. RHE in 1.0 M KOH. (b) *Operando* Raman measurements of Co-P towards OER between 0.8 V to 1.525 V vs. RHE in 1.0 M KOH.

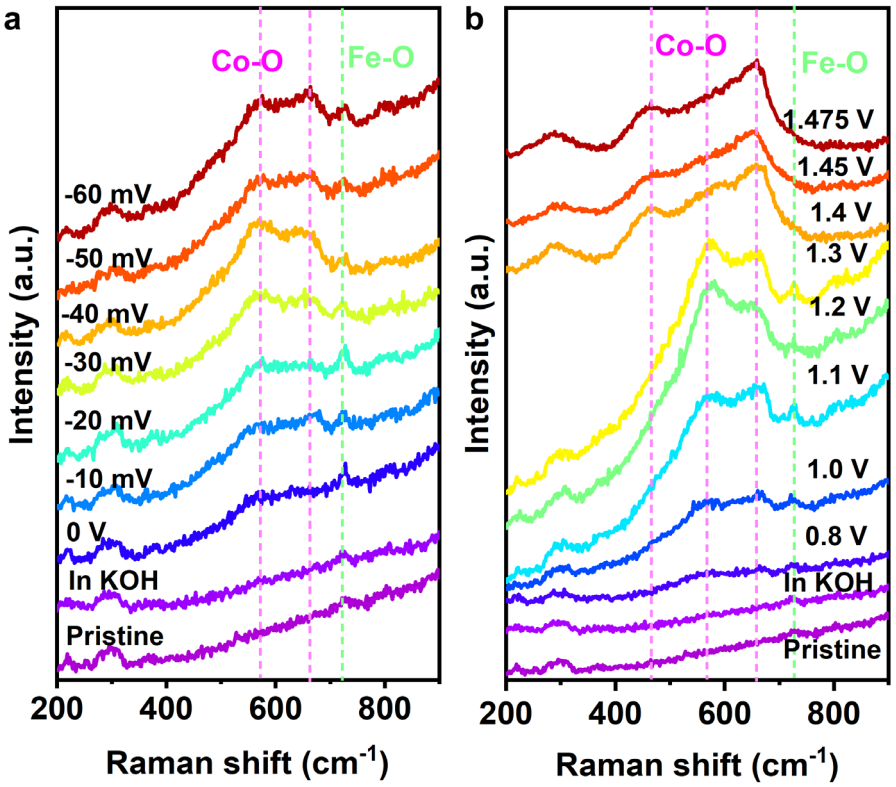

Figure S99. (a) *Operando* Raman measurements of Co@CoFe-P towards HER between 0 V to -60 mV vs. RHE 1.0 M KOH. (b) *Operando* Raman measurements of Co@CoFe-P towards OER between 0.8 V to 1.475 V vs. RHE in 1.0 M KOH.

11. Adsorption slab models and DFT simulations of Co-P and Co@CoFe-P towards HER

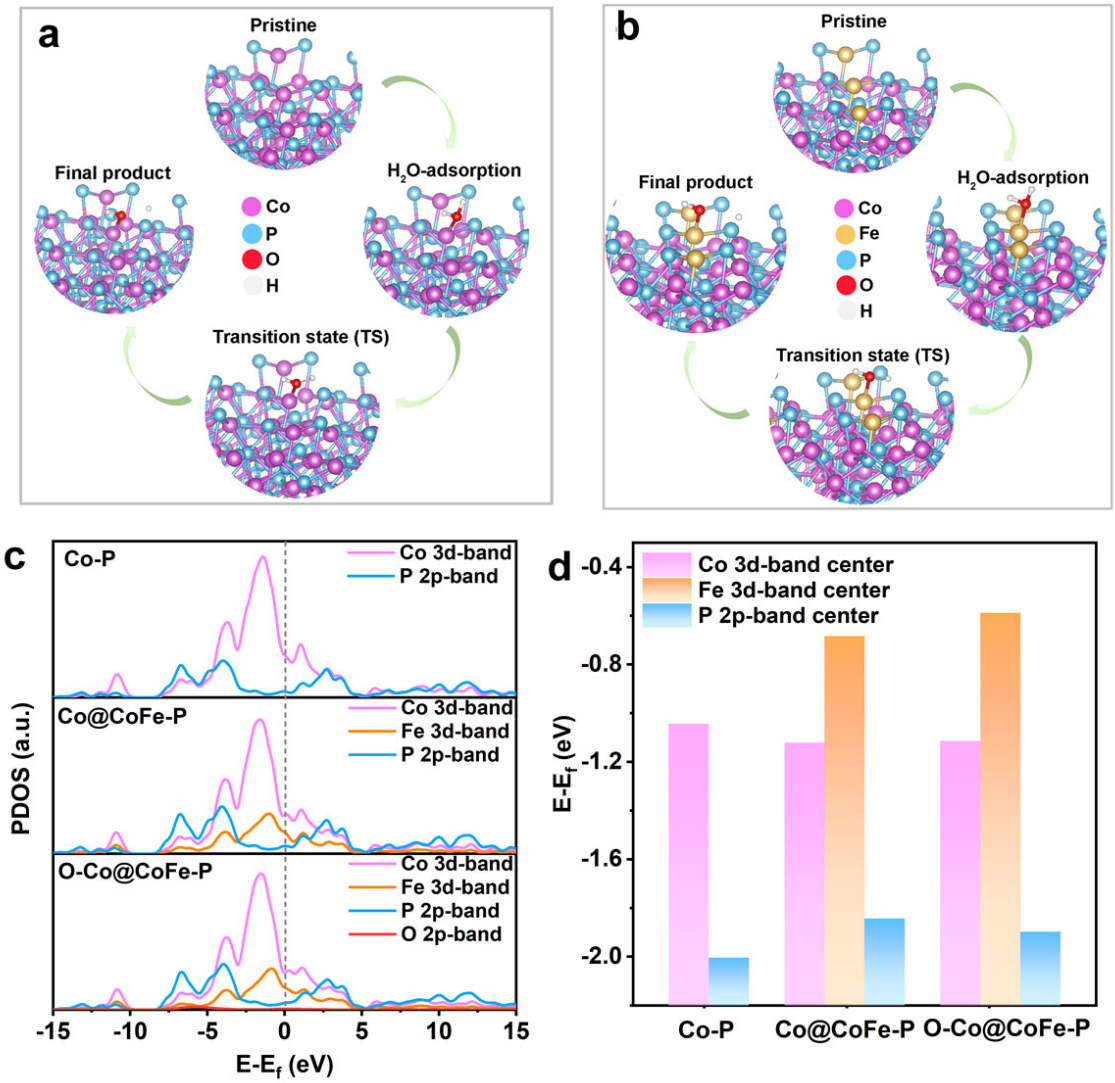

Figure S100. (a) Optimized adsorption slab models of Co-P towards HER in alkaline conditions. (b) Optimized adsorption slab models of Co@CoFe-P towards HER in alkaline conditions. (c) Simulated projected density of states (pDOS) of Co-P, Co@CoFe-P, and O incorporated Co@CoFe-P (O-Co@CoFe-P). (d) Calculated Co 3d, Fe 3d, and P 2p-band centers of three models.

12. KSCN poisoning test of Co@CoFe-P during HER and OER in 1.0 M KOH

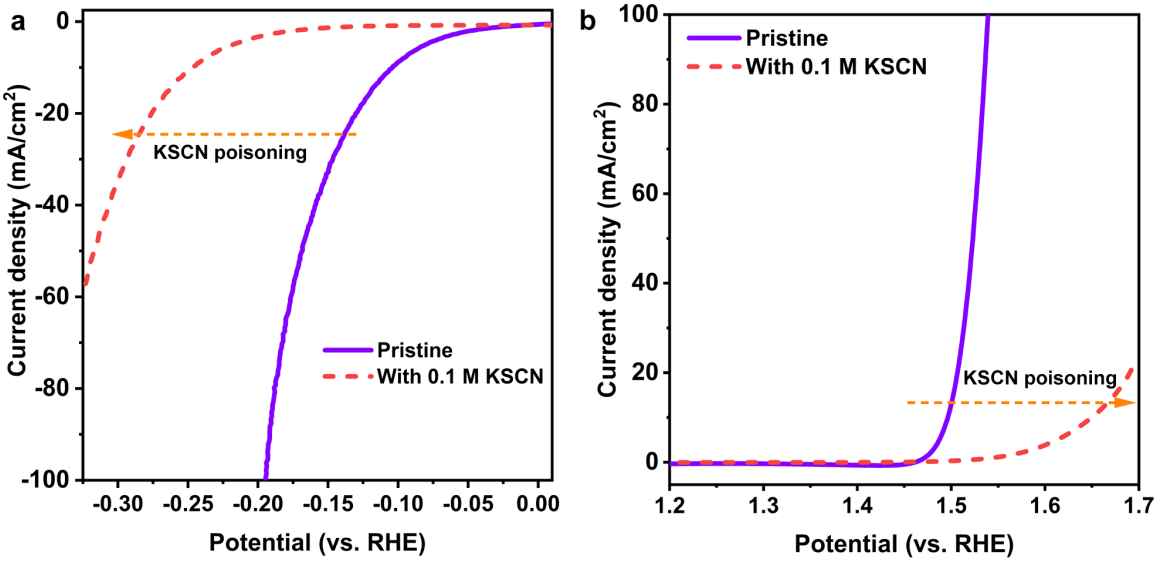

Figure S101. Electrochemical performance of Co@CoFe-P before and after adding 0.1 M KSCN: (a) HER in 1.0 M KOH; (b) OER in 1.0 M KOH.

Supplementary Discussion IX: Theoretical insights into the impact of reconstructed configurations on the atomistic catalytic mechanisms

To understand the influence of metal substitution and structural reconstruction on the electronic structures of the as-prepared catalysts, the projected density of states (pDOS) was calculated on the (111) surface for the proposed model structures of Co-P, Co@CoFe-P, and oxygen-containing Co@CoFe-P (denoted as O-Co@CoFe-P) (**Figure S100**). As shown in **Figure S100c**, the distributions of Co 3d and P 2p orbital states in Co-P spread over the Fermi level without a band gap, indicating the intrinsic metallic properties of Co-P,[76,81] which agrees with our above XANES results (**Figure 2a** and **Figure S48**). After insertion of Fe atoms into the lattice of Co-P, the pDOS of Co@CoFe-P shows a continuously enhanced overlap between Co 3d and P 2p orbital states near the Fermi level, which accounts for the facilitated electron transfer properties in Co@CoFe-P compared with Co-P. Based on the d-band theory,[34,96] an upshift of the metal d-band center close to the Fermi level can enhance the occupancy of antibonding orbital levels, thus promoting the adsorption of water molecules on the active metal centers. In contrast, the downshift of the metal d-band center away from the Fermi level can increase the bond strength between metal and hydrogen atoms, resulting in lower adsorption energy of H* intermediates. Moreover, Fe ($3d^6 4s^2$) is less electronegative compared with Co ($3d^7 4s^2$), which implies that Fe can contribute more electrons when being coordinated by non-metal elements.[34] As a result, the 3d-orbital of Fe is shifted closer to the Fermi level, which leads to a higher d-band center of Fe compared to Co. Therefore, the energy barriers of the adsorption of HER intermediates on the metal sites were regulated. It should be also noted that the slightly higher d-band position of Fe compared to Co can facilitate the adsorption of water molecules.[4] Furthermore, the incorporation of oxygen atoms into the lattice might generate more positive charge states around the metal center, and further shift the metal 3d-band orbital up to facilitate the water adsorption.[34] As shown in **Figure S100d**, partial Fe substitution induces a downshift of the Co 3d band-center in Co@CoFe-P. In comparison, a similar level of the Co 3d band-center with a slightly higher Fe 3d band-center is observed in O-Co@CoFe-P, indicating that the P-Co-O-Fe-P configuration is preferable for the adsorption of HER intermediates. To further shed light on the catalytically active sites of the as-prepared catalysts, the electrocatalytic performances of Co@CoFe-P NBs were tested again in 1.0 M KOH with 0.1 M KSCN (**Figure S101**). This is ascribed to the blocking effect of thiocyanate ions on the catalytic metal sites.[32] As expected, both the HER and OER activities of the as-investigated catalysts decline drastically after poisoning with 0.1 M KSCN, evidencing that the real catalytic active sites in Co@CoFe-P originate from the metal sites.

Table S1. ICP-MS results in fresh 1.0 M KOH before and after HER/OER measurements. (**Note:** *For the ICP-MS data collection, the catalyst inks were drop-dried on carbon paper with a loading mass of 2.0~3.0 mg/cm^2. Chronoamperometry measurements were performed in 50 mL of KOH and maintained at the constant potential for at least 1 h. After the measurement, 1 mL of electrolyte was sampled for ICP-MS tests*.)

Samples	**Co (ng/mL)**	**Fe (ng/mL)**	**P (ng/mL)**
Fresh KOH	0.46	1.58	4.84
HER (electrolyte)	3.08	9.30	232
HER (-60 mV vs. RHE)	4.29	9.65	252
HER (-120 mV vs. RHE)	4.67	9.12	262
HER (potential removed)	4.74	9.99	319
OER (electrolyte)	3.27	8.10	257
OER (1.0 V vs. RHE)	4.64	7.20	267
OER (1.2 V vs. RHE)	3.47	8.48	947
OER (1.35 V vs. RHE)	3.72	8.50	1080
OER (1.45 V vs. RHE)	4.24	8.75	1036
OER (1.5 V vs. RHE)	5.99	8.48	1080
OER (potential removed)	5.47	8.75	1079

Table S2. Elemental analysis of ZIF-67@CoFe-PB and Co@CoFe-P.

Samples	**C (mass-%)**	**H (mass-%)**	**N (mass-%)**
ZIF-67@CoFe-PB	27.530	2.639	20.040
Co@CoFe-P	1.617	0.263	1.981

Table S3. Atomic Co/Fe/P ratio in Co@CoFeP based on FESEM EDX and ICP-MS results.

Samples	**EDX results**	**ICP-MS results**
Co:Fe:P	3.5:1.0:4.3	3.6:1.0:5.0

Table S4. Measured pH values in 1.0 M KOH.

Samples	**Fresh 1.0 M KOH**	**With 0.1 M K_2HPO_4**	**Co@CoFe-P after OER**
pH	13.80	13.61	13.80

Table S5. Fitting parameters of the Co *K*-edge EXAFS spectra for the as-prepared catalysts and references. (**CN**: coordination numbers; **R**: interatomic distances; σ^2: Debye-Waller factors; S_0^2: amplitude reduction factor)

Samples	Path	CN	R (Å)	σ^2	S_0^2	ΔE
$Co(OH)_2$	Co-O	6	2.09(3)	0.0063(8)	0.825	-1.10(2)
	Co-Co	6	3.17(5)	0.0063(5)		
CoOOH	Co-O	6	1.89(9)	0.0035(3)	0.825	-0.58(9)
	Co-Co	6	2.85(3)	0.0038(6)		
Co-S	Co-O	0.37(2)	2.16(1)	0.0018(8)	0.825	0.66(6)
	Co-S	5.66 (1)	2.24(9)	0.0089(9)		
Co-S@CoFe-PB	Co-N/O	4.30(6)	2.05(4)	0.0088(6)	0.825	-3.04(0)
	Co-S	1.46(1)	2.25(0)	0.0084(7)		
Co-P	Co-O	0.30(4)	2.01(7)	0.0070(9)	0.825	0.44(7)
	Co-P	5.79(3)	2.28(2)	0.0089(3)		
Co-P in the air	Co-O	0.82(8)	2.00(8)	0.0070(6)	0.825	-1.27(8)
	Co-P	5.15(6)	2.28(6)	0.0090(2)		
Co@CoFe-P	Co-O	0.61(8)	2.00(6)	0.0047(5)	0.825	1.74(5)
	Co-P	5.29(7)	2.29(9)	0.0095(2)		

Table S6. Fitting parameters of the Fe *K*-edge EXAFS spectra for the as-prepared catalysts and references. (**CN**: coordination numbers; **R**: interatomic distances; σ^2: Debye-Waller factors; S_0^2: amplitude reduction factor)

Samples	Path	CN	R (Å)	σ^2	S_0^2	ΔE
Fe foil	Fe-Fe	8	2.44(4)	0.0094(8)	0.80	-2.40(4)
	Fe-Fe	6	2.79(9)	0.0054(6)		
Fe-P	Fe-O	0.75(0)	1.93(5)	0.0010(5)	0.80	4.00(6)
	Fe-P	5.31(3)	2.32(8)	0.0085(6)		
Co@CoFe-P	Fe-O	1.34(4)	1.93(8)	0.0011(6)	0.80	3.85(4)
	Fe-P	4.85(7)	2.32(7)	0.0095(4)		

Table S7. Fitting parameters of *operando* Co *K*-edge EXAFS spectra for Co-P towards HER under 1.0 M KOH conditions. (**CN**: coordination numbers; **R**: interatomic distances; σ^2: Debye-Waller factors; S_0^2: amplitude reduction factor)

Samples	Path	CN	R (Å)	σ^2	S_0^2	ΔE
Co-P in electrolyte	Co-O	0.55(1)	2.02(9)	0.0066(2)	0.825	2.38(3)
	Co-P	5.46(3)	2.29(1)	0.0092(0)		
50 mV	Co-O	0.50(6)	2.03(1)	0.0068(6)	0.825	2.03(4)
	Co-P	5.48(1)	2.29(1)	0.0091(3)		
0 mV	Co-O	0.51(4)	2.03(1)	0.0066(3)	0.825	2.02(8)
	Co-P	5.51(3)	2.29(1)	0.0092(3)		
-20 mV	Co-O	0.43(9)	2.03(2)	0.0067(2)	0.825	2.20(8)
	Co-P	5.50(2)	2.29(1)	0.0091(1)		
-40 mV	Co-O	0.42(6)	2.03(3)	0.0066(0)	0.825	2.29(4)
	Co-P	5.51(6)	2.29(1)	0.0091(2)		
-60 mV	Co-O	0.41(0)	2.03(4)	0.0067(1)	0.825	2.51(8)
	Co-P	5.49(6)	2.29(2)	0.0089(6)		
-80 mV	Co-O	0.41(9)	2.03(5)	0.0067(4)	0.825	2.65(3)
	Co-P	5.46(7)	2.29(2)	0.0089(2)		
-100 mV	Co-O	0.40(9)	2.03(7)	0.0065(1)	0.825	3.19(4)
	Co-P	5.47 (5)	2.29(6)	0.0089(5)		
-120 mV	Co-O	0.34(9)	2.04(1)	0.0066(3)	0.825	3.54(3)
	Co-P	5.45(2)	2.29(8)	0.0091(5)		
-130 mV	Co-O	0.24(6)	2.04(5)	0.0067(5)	0.825	3.91(6)
	Co-P	5.41(5)	2.30(1)	0.0092(0)		
Removed potential	Co-O	0.58(1)	2.03(1)	0.0066(3)	0.825	0.96(6)
	Co-P	5.04(9)	2.29(1)	0.0091(5)		
	Co-Co	0.78(3)	3.17(6)	0.0024(9)		

Table S8. Fitting parameters of *operando* Co *K*-edge EXAFS spectra for Co@CoFe-P towards HER under 1.0 M KOH conditions. (**CN**: coordination numbers; **R**: interatomic distances; σ^2: Debye-Waller factors; S_0^2: amplitude reduction factor)

Samples	Path	CN	R (Å)	σ^2	S_0^2	ΔE
Co@CoFe-P in electrolyte	Co-O	0.70(3)	2.01(0)	0.0045(4)	0.825	-0.21(9)
	Co-P	4.69(8)	2.29(2)	0.0092(9)		
	Co-Co/Fe	0.89(6)	3.12(6)	0.0047(5)		
50 mV	Co-O	0.71(4)	2.01(4)	0.0051(7)	0.825	-0.36(6)
	Co-P	4.72(2)	2.28(9)	0.0093(0)		
	Co-Co/Fe	0.89(8)	3.13(0)	0.0045(0)		
0 mV	Co-O	0.70(7)	2.01(5)	0.0050(2)	0.825	0.02(1)
	Co-P	4.70(8)	2.29(2)	0.0093(5)		
	Co-Co/Fe	0.90(2)	3.12(9)	0.0045(8)		
-10 mV	Co-O	0.71(6)	2.01(4)	0.0051(3)	0.825	0.06(3)
	Co-P	4.73(1)	2.29(3)	0.0094(1)		
	Co-Co/Fe	0.90(1)	3.13(2)	0.0045(8)		
-20 mV	Co-O	0.67(5)	2.01(8)	0.0052(0)	0.825	0.11(2)
	Co-P	4.70(4)	2.29(2)	0.0093(3)		
	Co-Co/Fe	0.86(3)	3.13(1)	0.0044(6)		
-30 mV	Co-O	0.68(9)	2.02(2)	0.0050(7)	0.825	0.36(1)
	Co-P	4.70(9)	2.29(3)	0.0094(3)		
	Co-O-Co/Fe	0.84(6)	3.13(5)	0.0043(9)		
- 40 mV	Co-O	0.65(8)	2.02(8)	0.0051(5)	0.825	0.65(5)
	Co-P	4.63(4)	2.29(3)	0.0093(1)		
	Co-Co/Fe	0.76(2)	3.13(9)	0.0041(2)		
-50 mV	Co-O	0.60(2)	2.03(7)	0.0053(5)	0.825	0.90(7)
	Co-P	4.63(9)	2.29(2)	0.0092(9)		
	Co-Co/Fe	0.68(1)	3.13(9)	0.0036(2)		
-60 mV	Co-O	0.62(1)	2.04(0)	0.0048(6)	0.825	1.20(6)
	Co-P	4.59(7)	2.29(3)	0.0092(5)		
	Co-Co/Fe	0.62(1)	3.13(9)	0.0033(9)		
-65 mV	Co-O	0.61(7)	2.04(0)	0.0045(5)	0.825	1.49(6)
	Co-P	4.62(4)	2.29(4)	0.0094(6)		
	Co-Co/Fe	0.55(2)	3.14(4)	0.0032(0)		
-70 mV	Co-O	0.59(1)	2.04(2)	0.0048(5)	0.825	2.02(4)
	Co-P	4.61(3)	2.29(6)	0.0094(6)		
	Co-Co/Fe	0.52(1)	3.14(9)	0.0032(5)		
Removed potential	Co-O	0.68(7)	2.01(1)	0.0051(4)	0.825	0.84(1)
	Co-P	4.60(0)	2.29(3)	0.0093(0)		
	Co-Co/Fe	0.68(2)	3.12(7)	0.0043(6)		

Table S9. Fitting parameters of *operando* Co *K*-edge EXAFS spectra for Co-P towards OER under 1.0 M KOH conditions. (**CN**: coordination numbers; **R**: interatomic distances; **σ^2**: Debye-Waller factors; **S_0^2**: amplitude reduction factor).

Samples	Path	CN	R (Å)	σ^2	S_0^2	ΔE
Co-P in electrolyte	Co-O	0.58(1)	2.03(1)	0.0066(6)	0.825	2.41(7)
	Co-P	5.45(1)	2.29(1)	0.0090(8)		
0.800 V	Co-O	0.58(6)	2.03(3)	0.0077(6)	0.825	0.91(8)
	Co-P	5.11(7)	2.29(1)	0.0093(6)		
	Co-Co $_{Co(OH)2}$	0.80(9)	3.18(3)	0.0029(0)		
1.000 V	Co-O	0.71(6)	1.92(6)	0.0075(5)	0.825	0.68(5)
	Co-P	4.77(5)	2.28(8)	0.0094(3)		
	Co-Co $_{Co(OH)2}$	0.89(9)	3.18(1)	0.0032(0)		
1.100 V	Co-O	1.25(8)	1.90(9)	0.0061(9)	0.825	-0.21(1)
	Co-P	4.31(2)	2.29(6)	0.0091(0)		
	Co-Co $_{CoOOH}$	0.49(5)	2.79(6)	0.0037(6)		
	Co-Co $_{Co(OH)2}$	0.82(2)	3.18(3)	0.0035(1)		
1.200 V	Co-O	2.29(8)	1.90(6)	0.0038(3)	0.825	1.82(6)
	Co-P	2.79(7)	2.32(1)	0.0084(2)		
	Co-Co $_{CoOOH}$	1.91(2)	2.81(9)	0.0040(1)		
1.300 V	Co-O	3.90(2)	1.90(2)	0.0035(6)	0.825	-0.83(9)
	Co-P	0.86(5)	2.32(6)	0.0045(8)		
	Co-Co $_{CoOOH}$	3.28(3)	2.82(7)	0.0040(1)		
1.400 V	Co-O	4.78(3)	1.89(8)	0.0038(0)	0.825	-0.39(9)
	Co-P	0.26(3)	2.34(7)	0.0048(8)		
	Co-Co $_{CoOOH}$	3.97(9)	2.83(3)	0.0038(8)		
1.425 V	Co-O	5.09(4)	1.89(3)	0.0036(8)	0.825	-0.49(3)
	Co-Co $_{CoOOH}$	4.25(2)	2.83(2)	0.0038(5)		
1.450 V	Co-O	5.05(7)	1.89(3)	0.0036(9)	0.825	-0.16(4)
	Co-Co $_{CoOOH}$	4.29(5)	2.83(4)	0.0038(6)		
1.475 V	Co-O	5.20(8)	1.89(2)	0.0036(0)	0.825	-0.96(8)
	Co-Co $_{CoOOH}$	4.39(9)	2.82(8)	0.0038(6)		
Removed potential	Co-O	5.39(7)	1.89(2)	0.0035(8)	0.825	-0.52(8)
	Co-Co $_{CoOOH}$	4.54(7)	2.83(2)	0.0038(6)		

Table S10. Fitting parameters of *operando* Co *K*-edge EXAFS spectra for Co@CoFe-P towards OER under 1.0 M KOH conditions. (**CN**: coordination numbers; **R**: interatomic distances; σ^2: Debye-Waller factors; S_0^2: amplitude reduction factor)

Samples	Path	CN	R (Å)	σ^2	S_0^2	ΔE
Co@CoFe-P in electrolyte	Co-O	0.66(5)	2.01(4)	0.0062(7)	0.825	0.63(9)
	Co-P	4.68(8)	2.29(2)	0.0094(8)		
	Co-Co/Fe	0.80(2)	3.12(9)	0.0047(2)		
0.800 V	Co-O	0.80(1)	2.00(7)	0.0068(0)	0.825	1.06(2)
	Co-P	4.49(7)	2.29(3)	0.0096(1)		
	Co-Co/Fe $_{Co(OH)2}$	0.79(1)	3.12(8)	0.0050(5)		
1.000 V	Co-O	1.19(9)	1.92(3)	0.0044(9)	0.825	0.92(0)
	Co-P	4.08(8)	2.29(4)	0.0093(4)		
	Co-Co/Fe $_{CoOOH}$	0.19(2)	2.81(1)	0.0030(2)		
	Co-Co/Fe $_{Co(OH)2}$	0.45(9)	3.12(3)	0.0042(5)		
1.100 V	Co-O	1.32(6)	1.92(4)	0.0036(5)	0.825	3.03(0)
	Co-P	3.80(0)	2.30(8)	0.0091(3)		
	Co-Co/Fe $_{CoOOH}$	0.35(5)	2.80(3)	0.0038(7)		
	Co-Co/Fe $_{Co(OH)2}$	0.27(1)	3.17(1)	0.0038(4)		
1.200 V	Co-O	2.32(5)	1.92(1)	0.0038(3)	0.825	1.80(1)
	Co-P	2.73(8)	2.32(2)	0.0085(8)		
	Co-Co/Fe $_{CoOOH}$	1.30(3)	2.82(5)	0.0039(4)		
1.300 V	Co-O	4.13(0)	1.90(5)	0.0040(0)	0.825	-1.27(6)
	Co-P	1.03(6)	2.31(7)	0.0050(9)		
	Co-Co/Fe $_{CoOOH}$	2.80(9)	2.83(1)	0.0039(3)		
1.325 V	Co-O	5.09(2)	1.90(4)	0.0036(1)	0.825	-0.53(9)
	Co-Co/Fe $_{CoOOH}$	4.13(9)	2.83(9)	0.0038(2)		
1.350 V	Co-O	5.55(2)	1.89(7)	0.0035(0)	0.825	-1.24(9)
	Co-Co/Fe $_{CoOOH}$	4.55(5)	2.83(7)	0.0036(4)		
1.375 V	Co-O	5.65(6)	1.89(4)	0.0034(9)	0.825	-1.34(3)
	Co-Co/Fe $_{CoOOH}$	4.62(8)	2.83(6)	0.0036(5)		
1.400 V	Co-O	5.71(3)	1.89(3)	0.0035(2)	0.825	-1.44(4)
	Co-Co/Fe $_{CoOOH}$	4.68(6)	2.83(5)	0.0036(5)		
1.425 V	Co-O	5.79(2)	1.89(1)	0.0036(3)	0.825	-1.84(0)
	Co-Co/Fe $_{CoOOH}$	4.73(6)	2.83(5)	0.0036(6)		
1.450 V	Co-O	5.83(2)	1.88(9)	0.0036(7)	0.825	-1.12(1)
	Co-Co/Fe $_{CoOOH}$	4.78(1)	2.83(3)	0.0036(7)		
Removed potential	Co-O	6.00(5)	1.88(5)	0.0018(4)	0.825	-3.72(8)
	Co-Co/Fe $_{CoOOH}$	5.37(2)	2.83(3)	0.0038(0)		

Table S11. Comparison of HER performance of the as-prepared electrocatalysts with recent studies.

Electrode material	Overpotential (mV) at 10 mA/cm^2	Tafel slope (mV/dec)	Stability (h)	Electrolyte	Substrate	Ref.
h-$Co_{0.34}Fe_{0.33}$ $Ni_{0.33}$-LDH	71	83	25	1.0 M KOH	Ni foam	[13]
Co-E_x-MoS_2	89	53	20	1.0 M KOH	GC-RDE	[14]
O-CoP	98	59.9	15	1.0 M KOH	GC-RDE	[15]
F-CoP-V_p-2	100 106	81.2 62.9	- 20	1.0 M KOH 1.0 M PBS	Carbon cloth	[16]
WC-W_2C/PNCDs	101	90	24	1.0 M KOH	Carbon paper	[17]
CoFeP	106	65.8	-	1.0 M KOH	Carbon cloth	[18]
MoC-Mo_2C/PNCDs	121	60	24	1.0 M KOH	Carbon paper	[17]
NiP_2-650 (c/m)	134 160 126	67 60.2 100	8	1.0 M KOH 0.5 M H_2SO_4 1.0 M PBS	Carbon cloth	[19]
CoP NFs	136 122	56.2 54.8	30	1.0 M KOH 0.5 M H_2SO_4	GC-RDE	[20]
CoP@FeCoP/NC YSMPs	141	56.3	20	1.0 M KOH	Carbon paper	[21]
CoPn	144	68	25	1.0 M KOH	Ni foam	[22]
$NiS_{0.5}Se_{0.5}$ nanorods	150	136	300	1.0 M KOH	Ni foam	[23]
CoNiP/NF	155 60 120	115 39 103	22	1.0 M KOH 0.5 M H_2SO_4 1.0 M KPi	Ni foam	[24]
NiSe-A	157	76	24	1.0 M KOH	Carbon paper	[25]
O-Co_2P	160	61	12	1.0 M KOH	GC-RDE	[26]
$Co_{0.85}Se$ NSs@Co	162 121	82 54	20 20	1.0 M KOH 0.5 M H_2SO_4	GC-RDE	[27]
CoP@PNC-DOS	173 160	63.9 62.1	30 30	1.0 M KOH 0.5 M H_2SO_4	GC-RDE	[28]
$Co_{0.9}Ni_{0.1}Se$ with vacancies	186	58	15	0.5 M H_2SO_4	GC-RDE	[29]
$Co_{0.9}Ni_{0.1}Se$	226	62	11	0.5 M H_2SO_4	GC-RDE	[29]
Ni-Co-P	270	60.6	-	1.0 M KOH	GC-RDE	[30]
Co-P	**214** **217** **329**	**116.59** **114.64** **157.37**	**-**	**1.0 M KOH** **0.5 M H_2SO_4** **1.0 M PBS**	**GC-RDE**	**This work**
Fe-P	**172** **140** **196**	**82.58** **77.94** **122.28**	**-**	**1.0 M KOH** **0.5 M H_2SO_4** **1.0 M PBS**	**GC-RDE**	**This work**
CoFe-P	**141** **116** **183**	**81.31** **70.43** **95.54**	**-**	**1.0 M KOH** **0.5 M H_2SO_4** **1.0 M PBS**	**GC-RDE**	**This work**
Co@CoFe-P	**104** **83** **150**	**78.97** **66.27** **90.04**	**12**	**1.0 M KOH** **0.5 M H_2SO_4** **1.0 M PBS**	**GC-RDE**	**This work**

Table S12. Comparison of OER performance of the as-prepared catalysts with recent studies on alkaline OER electrocatalysts (1.0 M KOH).

Electrode material	Overpotential (mV) at 10 mA/cm^2	Tafel slope (mV/dec)	Stability (h)	Substrate	Ref.
$Co_5Fe_3Cr_2$-LDH	232	31	168	GC-RDE	[31]
o-$CoTe_2$|P@HPC /CNTs	241	46	240	GC-RDE	[32]
CoOOH-NS	253	87	100	Carbon paper	[33]
Fe-$_{0.15}Co_9S_8$	255	49	12	GC-RDE	[34]
NiOOH-NS	258	61	100	Carbon paper	[35]
NiO/Co_3O_4	262	58	10	Ni foam	[36]
Fe-Co-P nanoboxes	269	31	100	Carbon paper	[37]
$La_{0.9}Ce_{0.1}NiO_3$	270	45	48	Carbon paper	[38]
$Fe_{0.4}Co_{0.6}Se_2$ nanoframes	270	36	24	GC-RDE	[39]
MoS_2/NiS_2-3	278	91.7	24	Carbon cloth	[40]
NiFe-LDH nanoprisms	280	49.4	6	GC-RDE	[41]
$CoSe_2$ UNMvac	284	46.3	20	GC-RDE	[42]
γ-FeOOH/NF-6M	286	51	48	Ni foam	[43]
$NSe_2/CoSe_2$-N	286	53	-	Carbon cloth	[44]
Co–Fe–S@PB NBs	286	37.84	33	GC-RDE	[5]
NiFeV-LDH	287	53.7	32	GC-RDE	[45]
D-CoPHoMSs	294	67	10	GC-RDE	[46]
NiCoPO/NC	300	94	10	GC-RDE	[47]
Exfoliated monolayer NiFe-LDH	300	42	12	Ni foam	[48]
$CoFeO_x$ nanosheets	308	36.8	3	GC-RDE	[49]
h-$CoTe_2$@HPC/CNTs	308	62	24	GC-RDE	[32]
O-CoP	310	83.5	15	GC-RDE	[15]
$Co_3S_4@MoS_2$	310	59	10	GC-RDE	[50]
CoP@PNC-DOS	316	42.9	-	GC-RDE	[28]
o-$CoTe_2$|P′@HPC/CNTs	326	71	24	GC-RDE	[32]
o-$CoTe_2$@HPC/CNTs	361	93	24	GC-RDE	[32]
$Li_2Co_2O_4$-20	361	46	-	Carbon paper	[51]
$Co_{0.5}Fe_{0.5}$S@N-Carbon	410	159	5	GC-RDE	[52]
RuO_2	**349**	**70.11**	**-**	**GC-RDE**	**This work**
IrO_2	**443**	**83.11**	**-**	**GC-RDE**	**This work**
Co-P	**327**	**45.23**	**-**	**GC-RDE**	**This work**
Fe-P	**470**	**63.31**	**-**	**GC-RDE**	**This work**
CoFe-P	**296**	**34.45**	**-**	**GC-RDE**	**This work**
Co@CoFe-O	**342**	**54.23**	**-**	**GC-RDE**	**This work**
Co@CoFe-P	**266**	**26.94**	**12**	**GC-RDE**	**This work**

Table S13. Comparison of overall water splitting performance of as-prepared bifunctional electrocatalysts with recent representative works.

Electrode material	Cell voltage (V) at 10 mA/cm^2	Stability (h)	Electrolyte	Substrate	Ref.
Mo-Ni_3S_2/Ni_xP_y/NF	1.46	72	1.0 M KOH	Ni foam	[53]
Ru-MnFeP/NF	1.47	50	1.0 M KOH	Ni foam	[54]
Fe-CoP/NF	1.49	50	1.0 M KOH	Ni foam	[55]
Co-Mo-P/Co NWs	1.50	35	1.0 M KOH	Ni foam	[56]
Cr-FeNi-P/NCN	1.50	20	1.0 M KOH	Ni foam	[57]
Ni_2P@$FePO_x$	1.51	100	1.0 M KOH	Ni foam	[58]
NiP/NiFeP/C	1.53	20	1.0 M KOH	Ni foam	[59]
CoP/NF	1.54	28	1.0 M KOH	Ni foam	[60]
CoFePO@NF	1.56	100	1.0 M KOH	Ni foam	[61]
Mo-CoP	1.56	20	1.0 M KOH	Carbon cloth	[62]
V-CoP@a-CeO_2	1.56	35	1.0 M KOH	Ni foam	[63]
Ni_2P-Fe_2P	1.56	48	1.0 M KOH	Ni foam	[64]
$Co_{0.6}Fe_{0.4}P$-1.125	1.57	120	1.0 M KOH	Ni foam	[65]
Ni/NiCoP	1.57	19	1.0 M KOH	Ni foam	[66]
a-$CoMoP_x$/CF	1.58	100	1.0 M KOH	Carbon paper	[67]
Meso-$Co_{1.8}Fe_{0.2}P$	1.58	25	1.0 M KOH	Ni foam	[68]
Fe-CoP HTPAs	1.59	50	1.0 M KOH	Ni foam	[69]
FeCoP UNSAs	1.60	20	1.0 M KOH	Ni foam	[70]
Fe-CoP/Ti	1.60	40	1.0 M KOH	Ti foil	[71]
Co-P@PC-750	1.60	60	1.0 M KOH	Carbon paper	[72]
O-CoP	1.60	18	1.0 M KOH	Ni foam	[15]
CoP-MNA	1.62	32	1.0 M KOH	Ni foam	[73]
Ni-Co-P	1.62	20	1.0 M KOH	Ni foam	[74]
NiS-$Ni_2P_2S_6$/NF	1.64	36	1.0 M KOH	Ni foam	[75]
CoP/NCNHP	1.64	36	1.0 M KOH	Ni foam	[76]
Co_2P/CoNPC	1.64	8	1.0 M KOH	Ni foam	[77]
Ce-CoP	1.65	15	1.0 M KOH	Ni foam	[78]
NiS/Ni_2P	1.67	10	1.0 M KOH	Carbon cloth	[79]
CoP/PNC	1.68	24	1.0 M KOH	Carbon paper	[80]
Ni-CoP/HPFs	1.68	25	1.0 M KOH	Ni foam	[81]
FeCo/Co_2P@NPCF	1.68	12	1.0 M KOH	Carbon paper	[82]
Co_2P/Co foil	1.71	12	1.0 M KOH	Co foil	[83]
CoP@PCN	1.74	30	1.0 M KOH	Glassy carbon	[28]
RuO_2||Pt/C	**1.56**	**-**	**1.0 M KOH**	**Carbon paper**	**This work**
Co@CoFe-P	**1.49**	**220**	**1.0 M KOH**	**Carbon paper**	**This work**

References

[1] H. Hu, B.Y. Guan, X. W. D. Lou, *Chem* **2016**. *1*, 102.
[2] X. Wang, Z. Na, D. Yin, C. Wang, Y. Wu, G. Huang, L. Wang, *ACS Nano* **2018**, *12*, 12238.
[3] M. Hu, A. A. Belik, M. Imura, Y. Yamauchi, *J. Am. Chem. Soc.* **2013,** *135*, 384.
[4] Z. F. Huang, J. Song, K. Li, M. Tahir, Y. T. Wang, L. Pan, L. Wang, X. Zhang, J. J. Zou, *J. Am. Chem. Soc.* **2016**, *138*, 1359.
[5] Y. G. Zhao, C. K. Mavrokefalos, P. Zhang, R. Erni, J. G. Li, C. A. Triana, G. R. Patzke, *Chem. Mater.* **2020**, *32*, 1371.
[6] O. Bunau, Y. Joly, *J. Phys.: Condens. Matter* **2009**, *21*, 345501.
[7] Y. G. Zhao, W. C. Wan, Y. Chen, R. Erni, C. A. Triana, J. G. Li, C. K. Mavrokefalos, Y. Zhou, G. R. Patzke, *Adv. Energy Mater.* **2020**, *10*, 2002228.
[8] J. VandeVondele, J. Hutter, *J. Chem. Phys.* **2007**, *127*, 114105.
[9] J. Hutter, M. Iannuzzi, F. Schiffmann, J. VandeVondele, *Comput. Mol. Sci.* **2014**, *4*, 15.
[10] W. C. Wan, C. A. Triana, J. G. Lan, J. G. Li, C. S. Allen, Y. G. Zhao, M. Iannuzzi, G. R. Patzke, *ACS Nano* **2020**, *14*, 13279.
[11] J. K. Nørskov, J. Rossmeisl, A. Logadottir, L. Lindqvist, J. R. Kitchin, T. Bligaard, H. Jonsson, *J. Phys. Chem. B* **2004**, *108*, 17886.
[12] Y. Luo, X. Li, X. Cai, X. Zou, F. Kang, H. M. Cheng, B. Liu, *ACS Nano* **2018**, *12*, 4565.
[13] H. Sun, L. Chen, Y. Lian, W. Yang, L. Lin, Y. Chen, J. Xu, D. Wang, X. Yang, M. H. Rümmerli, J. Guo, J. Zhong, Z. Deng, Y. Jiao, Y. Peng, S. Qiao, *Adv. Mater.* **2020**, *32*, 2006784.
[14] Y. Luo, X. Li, X. Cai, X. Zou, F. Kang, H. M. Cheng, B. Liu, *ACS Nano*, **2018**, *12*, 4565.
[15] G. Zhou, M. Li, Y. Li, H. Dong, D. Sun, X. Liu, L. Xu, Z. Tian, Y. Tang, *Adv. Funct. Mater.* **2020**, *30*, 1905252.
[16] K. Xu, Y. Sun, X. Li, Z. Zhao, Y. Zhang, C. Li, H. J. Fan, *ACS Mater. Lett.* **2020**, *2*, 736.
[17] X. F. Lu, L. Yu, J. T. Zhang, X. W. Lou, *Adv. Mater.* **2019**, *31*, 1900699.
[18] S. F. Hung, Y. Zhu, G. Q. Tzeng, H. C. Chen, C. S. Hsu, Y. F. Liao, H. Ishii, N. Hiraoka, H. M. Chen, *ACS Energy Lett.* **2019**, *4*, 2813.
[19] Q. Fu, X. Wang, J. Han, J. Zhong, T. Zhang, T. Yao, C. Xu, T. Gao, S. Xi, C. Liang, L. Xu, P. Xu, B. Song, *Angew. Chem. Int. Ed.* **2021**, *60*, 259; *Angew. Chem*. **2021**, *133*, 263.
[20] L. Ji, J. Wang, X. Teng, T. J. Meyer, Z. Chen, *ACS Catal.* **2019**, *10*, 412.
[21] J. Shi, F. Qiu, W. Yuan, M. Guo, Z. H. Lu, *Chem. Eng. J.* **2021**, *403*, 126312.
[22] A. Indra, P. W. Menezes, I. Zaharieva, H. Dau, M. Driess, *J. Mater. Chem. A* **2020**, *8*, 2637.
[23] Y. Wang, X. Li, M. Zhang, Y. Zhou, D. Rao, C. Zhong, J. Zhang, X. Han, W. Hu, Y. Zhang, K. Zaghib, Y. Wang, Y. Deng, *Adv. Mater.* **2020**, *32*, 2000231.
[24] A. Han, H. Chen, H. Zhang, Z. Sun, P. Du, *J. Mater. Chem. A* **2016**, *4*, 10195.
[25] L. Zhai, T. W. Benedict Lo, Z. L. Xu, J. Potter, J. Mo, X. Guo, C. C. Tang, S. C. Edman Tsang, S. P. Lau, *ACS Energy Lett.* **2020**, *5*, 2483.
[26] K. Xu, H. Ding, M. X. Zhang, M. Chen, Z. K. Hao, L. D. Zhang, C. Z. Wu, Y. Xie, *Adv. Mater.* **2017**, *29*, 1606980.
[27] R. Qin, J. Hou, C. Xu, H. Yang, Q. Zhou, Z. Chen, H. Liu, *Nano Res*. **2020**, *13*, 2950.
[28] Y. Li, Y. Liu, Q. Qian, G. Wang, G. Zhang, *Energy Storage Mater*. **2020**, *28*, 27.
[29] W. Zhong, Z. Wang, N. Gao, L. Huang, Z. Lin, Y. Liu, F. Meng, J. Deng, S. Jin, Q. Zhang, L. Gu, *Angew. Chem. Int. Ed.* **2020**, *59*, 22743; *Angew. Chem*. **2020**, *132*, 22931.
[30] Y. Feng, X. Y. Yu, U. Paik, *Chem. Commun*. **2016**, *52*, 1633.
[31] J. Chen, H. Li, S. Chen, J. Fei, C. Liu, Z. Yu, K. Shin, Z. Liu, L. Song, G. Henkelman, L. Wei, Y. Chen, *Adv. Energy Mater.* **2021**, *11*, 2003412.
[32] Z. Chen, M. Chen, X. Yan, H. Jia, B. Fei, Y. Ha, H. Qing, H. Yang, M. Liu, R. Wu, *ACS Nano* **2020**,*14*, 6968.

[33] J. Zhou, Y. Wang, X. Su, S. Gu, R. Liu, Y. Huang, S. Yan, J. Li, S. Zhang, *Energy Environ. Sci*. **2019**, *12*, 739.
[34] Z. Wang, Z. Lin, J. Deng, S. Shen, F. Meng, J. Zhang, Q. Zhang, W. Zhong, L. Gu, *Adv. Energy Mater.* **2021**, *11*, 2003023.
[35] X. Su, Y. Wang, J. Zhou, S. Gu, J. Li, S. Zhang, *J. Am. Chem. Soc.* **2018**, *140*, 11286.
[36] J. Zhang, J. Qian, J. Ran, P. Xi, L. Yang, D. Gao, *ACS Catal.* **2020**, *10*, 12376.
[37] H. Zhang, W. Zhou, J. Dong, X. F. Lu, X. W. D. Lou, *Energy Environ. Sci.***2019***, 12,* 3348.
[38] Y. Sun, R. Li, X. Chen, J. Wu, Y. Xie, X. Wang, K. Ma, L. Wang, Z. Zhang, Q. Liao, Z. Kang, Y. Zhang, *Adv. Energy Mater.* **2021**, *11*, 2003755.
[39] J. Zhang, Y. Yan, B. Mei, R. Qi, T. He, Z. Wang, W. Fang, S. Zaman, Y. Su, S. Ding, B. Y. Xia, *Energy Environ. Sci.* **2021**, *14*, 365.
[40] J. Lin, P. Wang, H. Wang, C. Li, X. Si, J. Qi, J. Cao, Z. Zhong, W. Fei, J. Feng, *Adv. Sci.* **2019**, *6*, 1900246.
[41] Le Yu, J. F. Yang, B. Y. Guan, Y. Lu, X. W. Lou, *Angew. Chem., Int. Ed.* **2018**, *57*, 172; *Angew. Chem.* **2018**, *130*, 178.
[42] Y. Zhang, C. Zhang, Y. Guo, D. Liu, Y. Yu, B. Zhang, *J. Mater. Chem. A* **2019**, *7*, 2536.
[43] K. Wang, H. Du, S. He, L. Liu, K. Yang, J. Sun, Y. Liu, Z. Du, L. Xie, W. Ai, W. Huang, *Adv. Mater.* **2021**, *33*, 2005587.
[44] X. Zheng, X. Han, Y. Cao, Y. Zhang, D. Nordlund, J. Wang, S. Chou, H. Liu, L. Li, C. Zhong, Y. Deng, W. Hu, *Adv. Mater.* **2020**, *32*, 2000607.
[45] L. Zhou, C. Zhang, Y. Zhang, Z. Li, M. Shao, *Adv. Funct. Mater.* **2021**, *31*, 2009743.
[46] P. Hou, D. Li, N. Yang, J. Wan, C. Zhang, X. Zhang, H. Jiang, Q. Zhang, L. Gu, D. Wang, *Angew. Chem. Int. Ed.* **2021***, 60,* 6926*; Angew. Chem.* **2021***, 133,* 7002.
[47] C. Wang, W. Chen, D. Yuan, S. Qian, D. Cai, J. Jiang, S. Zhang, *Nano Energy* **2020**, *69*, 104453.
[48] F. Song, X. Hu, *Nat. Commun.* **2014**, *5*, 4477.
[49] L. Zhuang, L. Ge, Y. Yang, M. Li, Y. Jia, X. Yao, Z. Zhu, *Adv. Mater.* **2017**, *29*, 1606793.
[50] Y. Guo, J. Tang, H. Qian, Z. Wang, Y. Yamauchi, *Chem. Mater.* **2017**, *29*, 5566.
[51] S. Zhang, S. Gu, Y. Wang, C. Liang, Y. Yu, L. Han, S. Zheng, N. Zhang, X. Liu, J. Zhou, J. Li, *ACS Catal.* **2019**. *9*, 7389.
[52] M. Shen, C. Ruan, Y. Chen, C. Jiang, K. Ai, L. Lu, *ACS Appl. Mater. Interfaces* **2015**, *7*, 1207.
[53] X. Luo, P. Ji, P. Wang, R. Cheng, D. Chen, C. Lin, J. Zhang, J. He, Z. Shi, N. Li, S. Xiao, S. Mu, *Adv. Energy Mater.* **2020**, *10*, 1903891.
[54] D. Chen, Z. Pu, R. Lu, P. Ji, P. Wang, J. Zhu, C. Lin, H.-W. Li, X. Zhou, Z. Hu, F. Xia, J. Wu, S. Mu, *Adv. Energy Mater.* **2020**, *10*, 2000814.
[55] L.-M. Cao, Y.-W. Hu, S.-F. Tang, A. Iijin, J.-W. Wang, Z.-M. Zhang, T.-B. Lu, *Adv. Sci.* **2018**, *5*, 1800949.
[56] V. H. Hoa, D. T. Tran, D. C. Nguyen, D. H. Kim, N. H. Kim, J. H. Lee, *Adv. Funct. Mater.* **2020**, *30*, 2002533.
[57] Y. Q. Wu, X. Tao, Y. Qing, H. Xu, F. Yang, S. Luo, C. H. Tian, M. Liu, X. H. Lu, *Adv. Mater.* **2019**, *31*, 1900178.
[58] F.-S. Zhang, J.-W. Wang, J. Luo, R.-R. Liu, Z.-M. Zhang, C.-T. He, T.-B. Lu, *Chem. Sci.* **2018**, *9*, 1375.
[59] B. Weng, X. Wang, C. R. Grice, F. Xu, Y. Yan, *J. Mater. Chem. A* **2019**, *7*, 7168.
[60] J. Liu, Y. Gao, X. Tang, K. Zhan, B. Zhao, B. Y. Xia, Y. Yan, *J. Mater. Chem. A* **2020**, *8*, 19254.
[61] J. Duan, S. Chen, A. Vasileff, S. Z. Qiao, *ACS Nano.* **2016**, *10*, 8738.
[62] C. Guan, W. Xiao, H. Wu, X. Liu, W. Zang, H. Zhang, J. Ding, Y. P. Feng, S. J. Pennycook, J. Wang, *Nano Energy* **2018**, *48*, 73.

[63] L. Yang, R. Liu, L. F. Jiao, *Adv. Funct. Mater.* **2020***, 30,* 1909618.
[64] L. B. Wu, L. Yu, F. H. Zhang, B. McElhenny, D. Luo, A. Karim, S. Chen, Z. F. Ren, *Adv. Funct. Mater.* **2020**, 2006484.
[65] Y. Lian, H. Sun, X. Wang, P. Qi, Q. Mu, Y. Chen, J. Ye, X. Zhao, Z. Deng, Y. Peng*, Chem. Sci.* **2019***,10,* 464.
[66] Y. Lin, Y. Pan, S. Liu, K. Sun, Y. Cheng, M. Liu, Z. Wang, X. Li, J. Zhang, *Appl. Catal. B: Environ.* **2019**, *259*, 118039.
[67] H. Huang, A. Cho, S. Kim, H. Jun, A. Lee, J. W. Han, J. Lee, *Adv. Funct. Mater.* **2020**, *30*, 2003889.
[68] S. Meng, S. Sun, Y. Qi, D. Jiang, W. Wei, M. Chen, *Inorg. Chem. Front.* **2020**, *7*, 3002.
[69] E. Hu, J. Ning, D. Zhao, C. Xu, Y. Lin, Y. Zhong, Z. Zhang, Y. Wang, Y. Hu, *Small* **2018**, *14*, 1704233.
[70] L. Zhou, M. Shao, J. Li, S. Jiang, M. Wei, X. Duan, *Nano Energy* **2017**, *41*, 583.
[71] C. Tang, R. Zhang, W. Lu, L. He, X. Jiang, A. M. Asiri, X. Sun, *Adv. Mater.* **2017**, 2*9*, 1602441.
[72] J. Wu, D. Wang, S. Wan, H. Liu, C. Wang, X. Wang, *Small* **2020**, *16*, 1900550.
[73] Y.-P. Zhu, Y.-P. Liu, T.-Z. Ren, Z.-Y. Yuan, *Adv. Funct. Mater.* **2015**, *25*, 7337.
[74] E. Hu, Y. Feng, J. Nai, D. Zhao, Y. Hu, X. W. Lou, *Energy Environ. Sci.* **2018**, *11*, 872.
[75] X. Zhang, S. Zhang, J. Li, E. Wang, *J. Mater. Chem. A* **2017**, *5*, 22131.
[76] Y. Pan, K. Sun, S. Liu, X. Cao, K. Wu, W. C. Cheong, Z. Chen, Y. Wang, Y. Li, Y. Liu, D. Wang, Q. Peng, C. Chen, Y. Li. *J. Am. Chem. Soc.* **2018**, *140*, 2610.
[77] H. Liu, J. Guan, S. Yang, Y. Yu, R. Shao, Z. Zhang, M. Dou, F. Wang, Q. Xu, *Adv. Mater.* **2020**, *32*, 2003649.
[78] J. J. Li, S. B. Zou, X. D. Liu, Y. Lu, D. H. Dong, *ACS Sustainable Chem. Eng*. **2020**, *8*, 10009.
[79] X. Xiao, D. Huang, Y. Fu, M. Wen, X. Jiang, X. Lv, M. Li, L. Gao, S. Liu, M. Wang, C. Zhao, Y. Shen, *ACS Appl. Mater. Interfaces* **2018**, *10*, 4689.
[80] Z. Peng, Y. Yu, D. Jiang, Y. Wu, B. Y. Xia, Z. Dong*, Carbon* **2019***, 144,* 464.
[81] Y. Pan, K. A. Sun, Y. Lin, X. Cao, Y.S. Cheng, S. J. Liu, L. Y. Zeng, W.-C. Cheong, D. Zhao, K. L. Wu, Z. Liu, Y. Q. Liu, D. S. Wang, Q. Peng, C. Chen, Y. D. Li, *Nano Energy* **2019***, 56*, 411.
[82] Q. Shi, Q. Liu, Y. Ma, Z. Fang, Z. Liang, G. Shao, B. Tang, W. Yang, L. Qin, X. S. Fang, *Adv. Energy Mater.* **2020**, *10*, 1903854.
[83] C.-Z. Yuan, S.-L. Zhong, Y.-F. Jiang, Z. K. Yang, Z.-W. Zhao, S.-J. Zhao, N. Jiang, A.-W. Xu, *J. Mater.Chem. A* **2017**, *5*, 10561.
[84] N. Kornienko, J. Resasco, N. Becknell, C.-M. Jiang, Y.-S. Liu, K. Nie, X. Sun, J. Guo, S. R. Leone, P. Yang, *J. Am. Chem. Soc.* **2015**, *137*, 7448.
[85] C. Zhang, Y. Shi, Y. Yu, Y. Du, B. Zhang, *ACS Catal.* **2018**, *8*, 8077.
[86] D. Cao, D. Liu, S. Chen, O. A. Moses, X. Chen, W. Xu, C. Wu, L. Zheng, S. Chu, H. Jiang, C. Wang, B. Ge, X. Wu, J. Zhang, Li Song, *Energy Environ. Sci.* **2021**, *14*, 906.
[87] L. Bai, C.-S. Hsu, D. T. L. Alexander, H. M. Chen, X. Hu, *J. Am. Chem. Soc.* **2019**, *141*, 14190.
[88] X. Su, Y. Wang, J. Zhou, S. Gu, J. Li, S. Zhang, *J. Am. Chem. Soc.* **2018**, *140*, 11286.
[89] H. Jin, X. Liu, S. Chen, A. Vasileff, L. Li, Y. Jiao, Li Song, Y. Zheng, S.-Z. Qiao, *ACS Energy Lett.* **2019**, *4*, 805.
[90] F. M. F. de Groot, S. Pizzini, A. Fontaine, K. Hämäläinen, C. C. Kao, J. B. Hastings, *Phys. Rev. B* **1995**, *51*, 1045.
[91] A. P. Grosvenor, R. G. Cavell, A. Mar, *J. Solid State Chem.* **2007**, *180*, 2702.
[92] A. P. Grosvenor, R. G. Cavell, A. Mar, *J. Solid State Chem.* **2008**, *181*, 2549.

[93] F. Yu, H. Zhou, Y. Huang, J. Sun, F. Qin, J. Bao, W. A. Goddard, S. Chen, Z. Ren, *Nat. Commun.* **2018**, *9*, 2551.
[94] F. Hu, S. Zhu, S. Chen, Y. Li, L. Ma, T. Wu, Y. Zhang, C. Wang, C. Liu, X. Yang, Li Song, X. Yang, Y. Xiong, *Adv. Mater.* **2017**, *29*, 1606570.
[95] Y. Zhou, S. Sun, S. Xi, Y. Duan, T. Sritharan, Y. Du, Z. J. Xu, *Adv. Mater.* **2018**, *30*, 1705407.
[96] Y. Zhou, S. Sun, J. Song, S. Xi, B. Chen, Y. Du, A. C. Fisher, F. Cheng, X. Wang, H. Zhang, Z. J. Xu, *Adv. Mater.* **2018**, *30*, 1802912.
[97] J. Nai, X. W. Lou, *Adv. Mater.* **2019**, *31*, 1706825.
[98] F. Xie, L. Zhang, C. Ye, M. Jaroniec, S.-Z. Qiao, *Adv. Mater.* **2019**, *31*, 1800492.
[99] Y. Fang, D. Luan, X. W. Lou, *Adv. Mater.* **2020**, *32*, 2002976.
[100] D.-S. Bin, Y. Li, Y.-G. Sun, S.-Y. Duan, Y. Lu, J. Ma, A.-M. Cao, Y.-S. Hu, L.-J. Wan, *Adv. Energy Mater.* **2018**, *8*, 1800855.
[101] Y. Fang, D. Luan, SY. Chen, S. Gao, X. W. Lou, *Angew. Chem. Int. Ed.* **2020**, *59*, 7178; *Angew. Chem.* **2020,** *132*, 7245.
[102] G. K. Schweitzer, L. L. Pesterfield, The Aqueous Chemistry of the Elements, *Oxford University Press*, **2010**.
[103] A. Bergmann, T. E. Jones, E. Martinez Moreno, D. Teschner, P. Chernev, M. Gliech, T. Reier, H. Dau, P. Strasser, *Nat. Catal*. **2018**, *1*, 711.
[104] B. Pattengale, Y. Huang, X. Yan, S. Yang, S. Younan, W. Hu, Z. Li, S. Lee, X. Pan, J. Gu, J. Huang, *Nat. Commun.* **2020**, *11*, 4114.
[105] S. Song, J. Zhou, X. Su, Y. Wang, J. Li, L. Zhang, G. Xiao, C. Guan, R. Liu, S. Chen, H.-J. Lin, S. Zhang, J.-Q. Wang, *Energy Environ. Sci.* **2018**, *11*, 2945.
[106] M. Risch, F. Ringleb, M. Kohlhoff, P. Bogdanoff, P. Chernev, I. Zaharieva, H. Dau, *Energy Environ. Sci.* **2015**, *8*, 661.
[107] J. G. McAlpin, Y. Surendranath, M. Dinca, T. A. Stich, S. A. Stoian, W. H. Casey, D. G. Nocera, R. D. Britt, *J. Am. Chem. Soc.* **2010**, *132*, 6882.